STUDY OF THE TRUE PERFORMANCE LIMITS OF THE ASTROMETRIC MULTIPLEXING AREA SCANNER (AMAS)

(NAS5-20065)

Final Report

Covering the Period
April 1974-March 1975

Laurence W. Fredrick, Principal Investigator

and

Harold A. McAlister

Leander McCormick Observatory
P.O. Box 3818 University Station
Charlottesville, Virginia 22903

LEANDER McCORMICK OBSERVATORY
UNIVERSITY OF VIRGINIA • CHARLOTTESVILLE

STUDY OF THE TRUE PERFORMANCE LIMITS OF THE ASTROMETRIC MULTIPLEXING AREA SCANNER (AMAS)

(NAS5-20065)

Final Report

Covering the Period
April 1974-March 1975

Laurence W. Fredrick, Principal Investigator

and

Harold A. McAlister

Leander McCormick Observatory
P.O. Box 3818 University Station
Charlottesville, Virginia 22903

TABLE OF CONTENTS

ABSTRACT

The Astrometric Multiplexing Area Scanner (AMAS) is an instrument designed to perform photoelectric long-focus astrometry of small fields, replacing both the photographic plate and the measuring engine. Modulation of a telescope focal plane with a rotating Ronchi ruling produces a frequency modulated signal from which relative positions and magnitudes can be extracted.

Observations of double and multiple star systems have indicated a lower limit to resolution of $\sim$ 4 arcseconds. However, these observations were made under unfavorable conditions of seeing and telescope performance. The results presented here were made to check the above result and to provide additional data on the overall precision and accuracy of the AMAS. The basic observations were made in the laboratory under precisely controlled conditions using near Gaussian artificial double star images with separation adjustable in 10.3 ± 1.2 μ steps in the ruling plane. The existing reduction technique is modified to more properly consider the signal D.C. term and to calculate the image radius.

The data is used to evaluate instrumental precision, accuracy and resolution characteristics with respect to a variety of instrumental and cosmical parameters that include distance from ruling center, signal/noise, record length and binary star separation, position angle and magnitude difference. Binary star and stellar field signals were generated by

adding individually observed signals whose solutions may be compared with the combined solutions of the summed signals. Fields of up to 10 stars were generated in this manner.

The results indicate 1.5 μ precision and accuracy for single stars under specific conditions. This value decreases for increased number of field stars, particularly for fainter stars. For star images of diameter $\sim$ 120 μ, accurate binary resolution occurs at separations $\gtrsim$ 120 μ for $\delta m < 1$. This lower limit increases to $\sim$ 170 μ for $1 \lesssim \delta m < 3$. One may conclude that the prototype AMAS is capable of performing at least as well as the photographic plate - measuring engine combination for long-focus astrometry, providing the field stars are of very similar magnitude or are observed individually. Highly constant ruling rotation rate and accurate centering are shown to be essential to accurate performance. Variations on the present AMAS scheme, the applicability of the AMAS to an LST and areas for continued study are briefly discussed.

Introduction

The development of the Astrometric Multiplexing Area Scanner (AMAS) at the Leander McCormick Observatory is an attempt to modernize the observational approach to the traditional astrometric problem of determining precise, relative stellar positions. The modernization effort takes several forms: (a) substituting for the photographic plate a higher-quantum-efficient detector; (b) altering the archival aspect from preserving delicate irreplaceable emulsions to filing away completely reproducible numbers; and, (c) replacing direct geometric measures with mathematical data reduction generated by computer analysis, which has the additional advantage that it can be done on-line at the telescope. Each of these items contribute to the overall desirability of an AMAS-type instrument. The AMAS is also a suitable instrument for performing astrometry from space; for example, from the Large Space Telescope (LST) where the photographic plate is ruled out for many reasons.

Before any instrument is adopted for a scientific program, a thorough analysis of its capabilities and inherent systematic errors is a prerequisite to a final judgement on its use. The purpose here is to determine the true performance limits of the AMAS with as much certainty as possible. Such work is essential, as work by Smith (1973) with the AMAS on a ground-based telescope placed an observational lower

limit on the resolution of binary stars at 4 arc-seconds. This is a constrained result, as pointing accuracy and effects of atmospheric turbulence degrade performance so the data do not truly reflect the intrinsic capability of the AMAS. There are also no observations to show the relative accuracy which the AMAS yields for the positions and magnitudes of a field of stars.

The present evaluation of the AMAS is via a detailed series of observations in a laboratory situation using an optical system to model the various observational problems to which the AMAS might be applied. This report presents the results of these laboratory observations, additional relevant discussions of particular areas and a general discussion of the AMAS technique. The results indicate a performance level equal to that of the photographic plate-measuring engine combination. As these results were obtained with the relatively imprecise proto-type version of the AMAS, an improved next generation instrument will certainly enhance the attractiveness of the AMAS.

I. AMAS Signal Analysis and Reduction

A. Operation and Principles

The AMAS principle is to modulate the focal plane of a telescope with a rotating mask producing an output signal that is a unique function of the positions and intensities of the point sources within the field. The signal is simply the convolution of the mask transmission function with the intensity distributions of the sources. Thus, one is left with a deconvolution problem to obtain the astrometric information.

A strong-point for the AMAS is its ability to look simultaneously in multiple directions. The AMAS "scans" in the sense of passing a transmission array through the focal plane while sampling the combined transmitted light at discrete time intervals. It does not scan in the usual sense, i.e. point-to-point sampling of the field intensity. Thus, the AMAS adds, or "multiplexes", the individual signals from all point sources in the field of view.

The AMAS is in several ways analogous to the x-ray rotation modulation collimator (RMC) (Gursky and Schwartz 1974). The present AMAS scheme is to use a Ronchi ruling, composed of alternate transparent and opaque lines which are parallel and of equal widths, as the modulation mask. The RMC employs two planes of parallel wires to achieve fine resolution and overcomes the positional ambiguity of the simple modulation collimator by rotation about the axis

perpendicular to the wire planes. The response of the RMC to a source is analyzed in terms of frequency, phase and amplitude to determine the location and strength of the source in the field. The AMAS response may be treated in the exact same manner. Both instruments look in multiple directions at once and superpose signals from all the sources in the field. Both instruments can integrate by repeated rotation to improve the signal/noise.

B. Equipment Description

A detailed mechanical description of the prototype AMAS is given in the works of Rosenberg (1972) and Smith (1973). A schematic diagram of the AMAS is shown in Figure I.1. which emphasizes the overall simplicity of the instrument.

Two major differences exist between the present configuration and that used by Smith (1973): (1) the original motor is replaced with a more powerful synchronous motor yielding a higher degree of rotational constancy; and, (2) the photomultiplier operation is converted from D.C. to a pulse counting scheme, designed to operate at typical AMAS illumination levels. These two improvements more accurately produce the signal expected from an ideal AMAS system. In addition, the AMAS was cleaned thoroughly and lubricated to produce the highest level of rotational constancy obtainable from the prototype. Because the motor is situated within a few inches of the photomultiplier tube housing, a reflective layer of aluminum foil was placed between the two to help

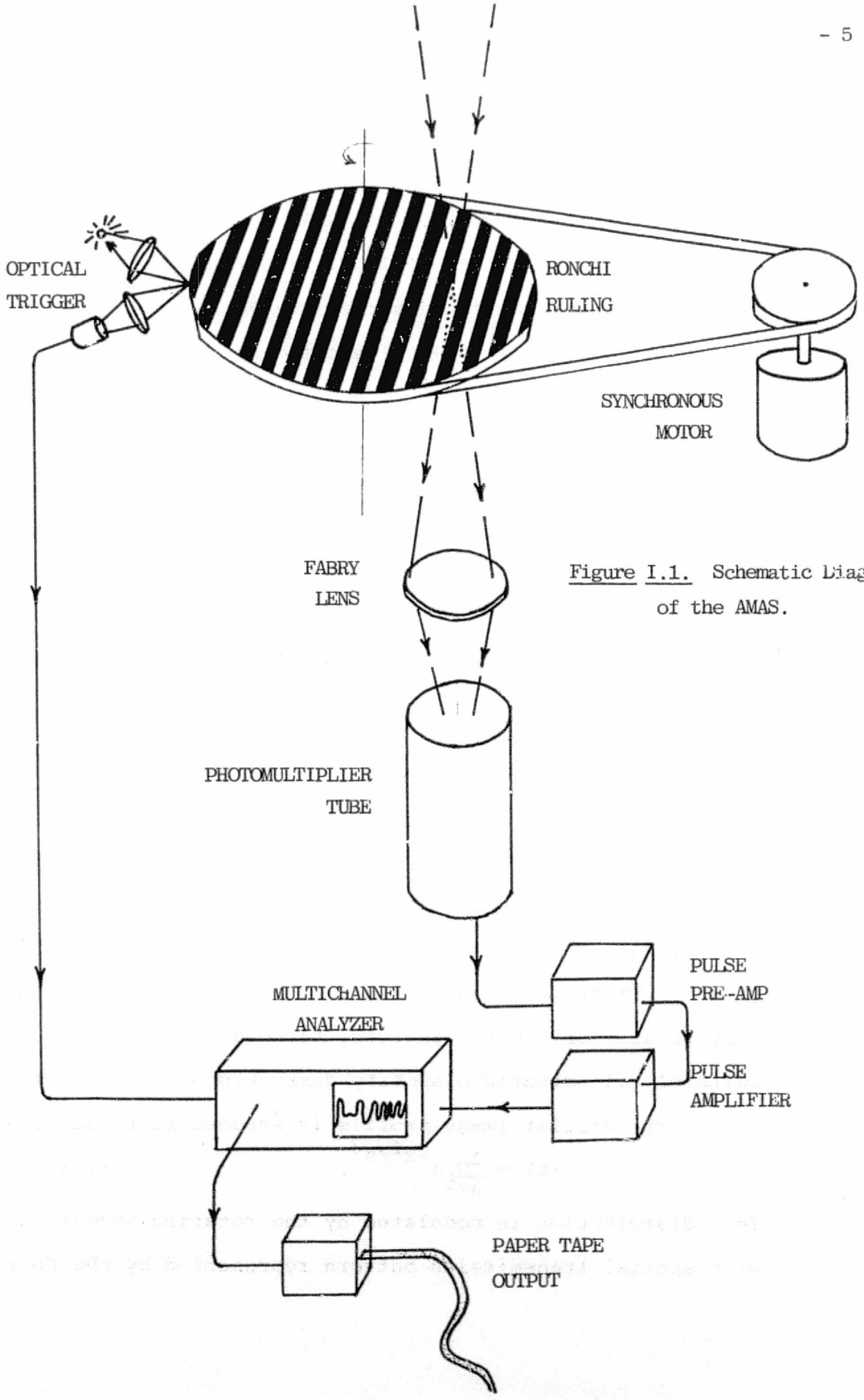

Figure I.1. Schematic Diagram of the AMAS.

insulate the tube from the rather warm motor. The tube is uncooled due to design limitations of the prototype.

The field of view of the AMAS is limited by the 22 mm aperture of the Fabry lens. The Fabry lens-PMT assembly may be translated across the Ronchi ruling to select the portion of the telescope focal plane to be observed. In this laboratory study the artificial stars observed were centered in the field of view of the PMT to avoid vignetting by the Fabry lens. Photometric accuracy should be assured in practice by placing an aperture stop in front of the Fabry lens. A strictly defined field is also a present requirement since the number of stars contributing to the output signal must be known as explained in the next section.

C. Mathematical Description

The mathematical form of the modulated signal from the AMAS is dicussed in detail by Rosenberg (1972). Here, for the sake of completeness, an abbreviated description of this signal is presented. This description parallels that given by Fredrick, et al (1975). The discussion pertains only to stellar "point" sources, although an extension to uniformly illuminated planetary disks probably is feasible.

The stellar image profile is assumed to be Gaussian,

$$\Psi(x) = \frac{I_o}{\sigma\pi^{\frac{1}{2}}} e^{-x^2/\sigma^2} . \qquad (1\text{-}1)$$

This distribution is modulated by the rotating Ronchi ruling, with spatial transmission pattern represented by the Fourier

series

$$T(x) = \sum_{n=1}^{\infty} a_n \mathrm{Cos}\frac{n\pi x}{L} \quad , \qquad (1\text{-}2)$$

where L is the line spacing (mm/line) of the Ronchi ruling, and

$$a_n = \frac{2}{n\pi}\mathrm{Sin}\frac{n\pi}{2}$$

so that all even ordered terms vanish. The geometry of the Ronchi ruling is shown in Figure I.2.

As the observed intensity is the convolution of the image profile with the transmission pattern, the instantaneous intensity at a point x is given by

$$I(x) = \int_{-\infty}^{\infty} T(x')\Psi(x-x')dx'$$

$$= \tfrac{1}{2}I_o\{1 + \frac{4}{\pi}\sum_{n=1}^{\infty}\frac{(-1)^{n+1}}{m} e^{-(m\sigma\pi/2L)^2} \mathrm{Cos}\frac{m\pi x}{L}\}, \qquad (1\text{-}3)$$

where $m \equiv 2n - 1$.

If the ruling is rotated about a point centered between two dark lines,

$$x(t) = R\mathrm{Cos}(\omega t + \theta) \ ,$$

where (R,θ) are the polar coordinates of the Gaussian source. Thus, the observed intensity becomes the time varying function

$$I(t) = \tfrac{1}{2}I_o\{1 + \frac{4}{\pi}\sum_{n=1}^{\infty}\frac{(-1)^{n+1}}{m} e^{-(m\sigma\pi/2L)^2} \cdot$$

$$\mathrm{Cos}(\frac{m\pi R}{L}\mathrm{Cos}(\omega t+\theta))\} \ . \qquad (1\text{-}4)$$

The spacing parameter L may be selected so that σ/L is large enough to permit truncation of the series at the first term, while maintaining a reasonably high degree of modulation. In this work σ/L is selected to be of the order of 0.5. A quantitative evaluation of this ratio is given below.

As in practice the data is stored in the memory of a

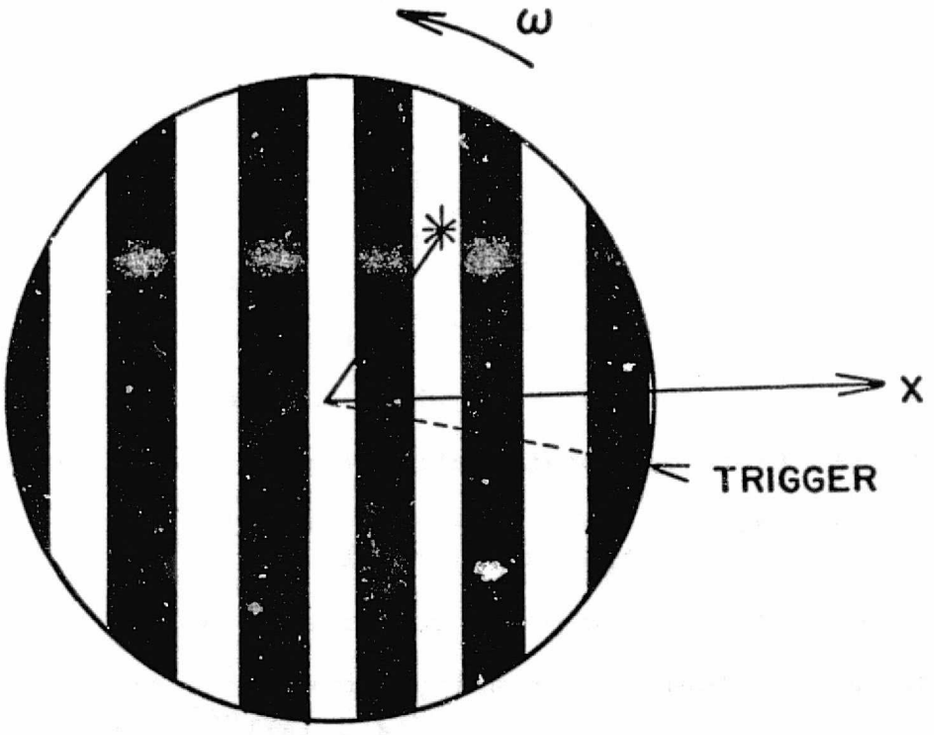

Figure I.2. The Geometry of the Ronchi Ruling.

multichannel analyzer, it is convenient to express the signal in a discrete form for J channels and K sources. For convenience a D.C. term is subtracted in a manner to be discussed in the next section and the remaining damping factor $4/\pi e^{-(\sigma\pi/2L)^2}$ and $\frac{1}{2}I_{ok}$ are absorbed by a constant A_k. The intensity in the j^{th} channel is then given by

$$I_j = \sum_{k=1}^{K} A_k \cos\left(\frac{\pi R_k}{L}\cos(\omega t_j + \theta_k)\right)$$

$$= \sum_{k=1}^{K} A_k \cos\frac{\pi}{L}(x_k u_j - y_k v_j) \qquad (1\text{-}5)$$

where $u_j \equiv \cos\omega t_j$
$v_j \equiv \sin\omega t_j$
$t_j \equiv$ mean channel time

If values for x_k, y_k and A_k are assumed initially, the last equation may be written in terms of these estimates plus the small corrections Δx_k, Δy_k and ΔA_k. Expanding Eq. (1-5) and keeping terms only to the first order in the corrections gives

$$I_j \simeq \sum_{k=1}^{K} \{A_k \cos\frac{\pi}{L}(x_k u_j - y_k v_j) -$$

$$A_k \frac{\pi}{L}(\Delta x_k u_j - \Delta y_k v_j)\sin\frac{\pi}{L}(x_k u_j - y_k v_j) +$$

$$(\Delta A_k)\cos\frac{\pi}{L}(x_k u_j - y_k v_j)\} \equiv I_{jo} \qquad (1\text{-}6)$$

The corrections to position and intensity are determined by defining an error parameter

$$S \equiv \sum_{j=1}^{J} (I_j - I_{jo})^2$$

and applying the method of least-squares in the usual manner. This yields 3K linear equations in the 3K unknowns Δx_k, Δy_k and ΔA_k. These equations are solved iteratively until the

corrections in position and intensity are less than or equal to 0.1 micron and one count. The procedure converges usually on five iterations, if the initial estimates of position are accurate to about 100 microns. The final solution is otherwise found to be completely independent of the initial estimates. This rate of convergence is, of course, dependent upon the number of field stars, their relative spatial distribution and their absolute and relative signal strengths.

The 180° ambiguity with respect to the center of rotation is eliminated in practice by observing with the center of rotation outside the field of view. The distance of the field center from the rotation axis appears to be unimportant as long as an adequate number of channels is available to record the highest frequency. One might intuitively expect greater accuracy and precision from images receiving a higher degree of modulation, i.e. further from the rotation center. From the point of view of power spectral analysis this might be a proper conclusion. However, since the positions and intensities are determined from a least-squares fit of an observed to a theoretical curve, the empirical definition of the intensity curve is the overriding factor. With this in mind, the observations made were confined to the neighborhood near the rotation center to minimize smearing which tends to occur when a small number of channels is used to record the high frequency component. This smearing is, of course, due to the non-constant ruling rotation rate. The specific effects

of observing at large R are considered later in more detail. An example of an observed signal along with the best fit to the observation is shown in Figure I.3 where counting rate is plotted as a function of ruling position angle for 180° of rotation (or, as a function of channel number).

D. Evaluation of the D.C. Term

In writing the discrete form of the intensity function, Eq. (1-5), a D.C. component is subtracted from the signal. Rosenberg (1972) and Smith (1973) do this simply by subtracting out the mean value of the signal. This is not the best way to remove this term.

If the intensity in the j^{th} channel arising from the k^{th} source is written as

$$I_{jk} = \tfrac{1}{2} I_{ok}(1 + A_k' \mathrm{Cos}\Omega_{jk}) \qquad (1\text{-}7)$$

where

$$A_k' \equiv \frac{4}{\pi} e^{-(\sigma\pi/2L)^2} \qquad (1\text{-}8)$$

and

$$\Omega_{jk} \equiv \frac{\pi}{L}(x_k u_j - y_k v_j) = \frac{\pi}{L} R_k \mathrm{Cos}(\theta_j + \theta_k) \ .$$

Then

$$\overline{I}_k \equiv \frac{1}{N} \sum_{j=1}^{N} I_{jk} = \frac{1}{N} \sum_{j=1}^{N} \tfrac{1}{2} I_{ok}(1 + A_k' \mathrm{Cos}\Omega_{jk})$$

$$= \tfrac{1}{2} I_{ok}(1 + A_k' \overline{\mathrm{Cos}\Omega_{jk}}) \ . \qquad (1\text{-}9)$$

Thus, the actual D.C. term is then

$$\tfrac{1}{2} I_{ok} = \frac{\overline{I}_k}{1 + A_k' \overline{\mathrm{Cos}\Omega_{jk}}} \ , \qquad (1\text{-}10)$$

instead of the simple mean of the intensity. The D.C. term is not simply the mean intensity as the extended duration of the low frequency intensity value weights the average so that

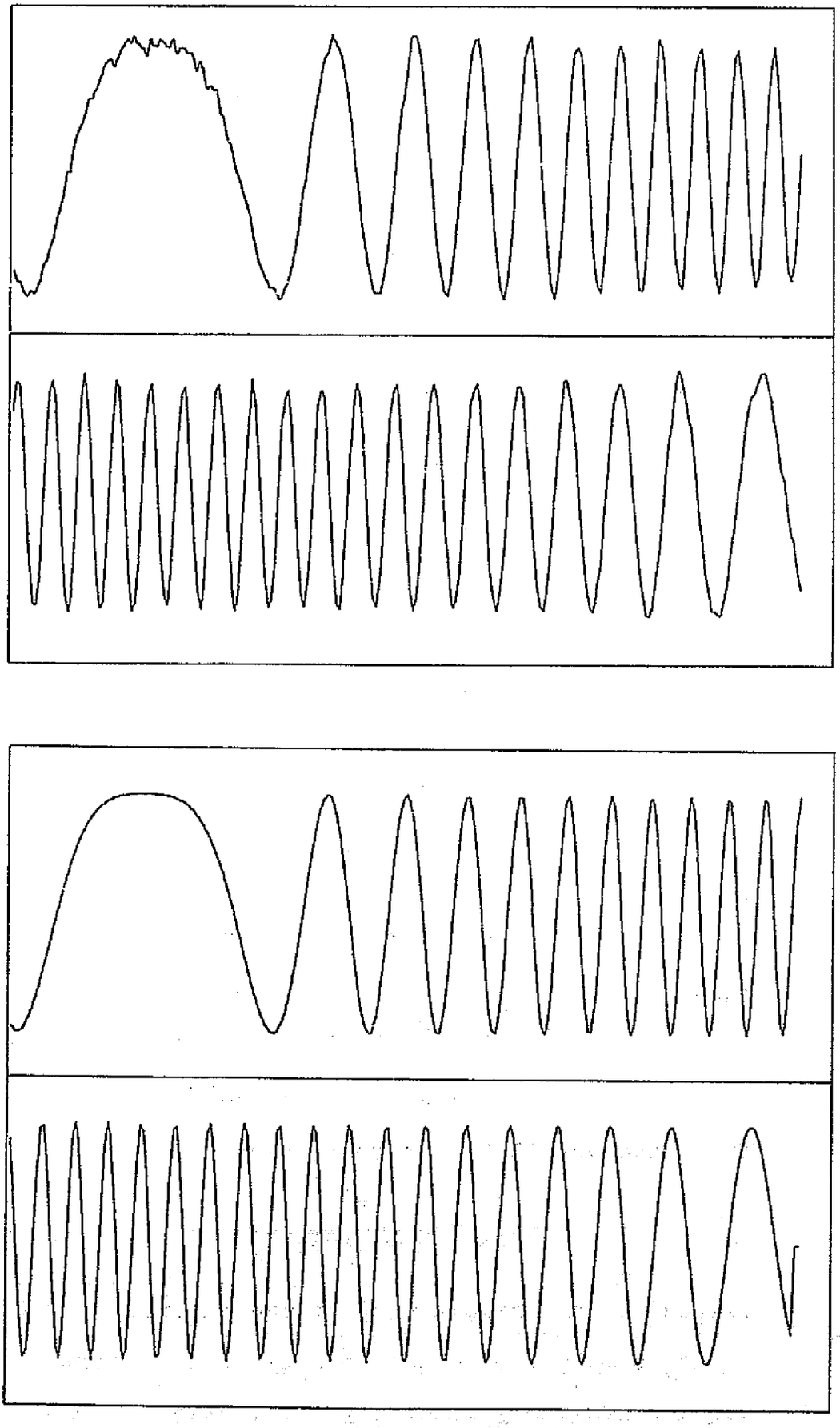

Figure I.3. (a) Typical AMAS Signal for N_{chan}=480 and (b) The Least-Squares Fit to (a) Yielding Values of R/L = 29.9623, θ = 16°.1417 and m = 10.7.

it is above or below the mean D.C. value.

To evaluate the D.C. term for K sources, the following iteracive procedure is applied to the observations. First, the scraight mean is subtracted from each channel-value of the intensity to form

$$I_j^{(1)} \equiv I_j - \bar{I}$$
$$= \sum_{k=1}^{K} (\tfrac{1}{2} I_{ok} + A_k \mathrm{Cos}\Omega_{jk}) - \bar{I} \qquad (1\text{-}11)$$

where

$$\bar{I} \equiv \sum_{k=1}^{K} \bar{I}_k = \sum_{k=1}^{K} (\tfrac{1}{2} I_{ok} + A_k \overline{\mathrm{Cos}\Omega_{jk}}) \qquad (1\text{-}12)$$

and

$$A_k \equiv \tfrac{1}{2} I_{ok} \frac{4}{\pi} e^{-(\sigma\pi/2L)^2} = \tfrac{1}{2} I_{ok} A_k' \ .$$

The values of $I_j^{(1)}$ are used in the iterative procedure of Section I.C to provide values for $x_k^{(1)}$, $y_k^{(1)}$ and $A_k^{(1)}$ for the K sources. Equations (1-11) and (1-12) show that one may add

$$\Delta I_j \equiv \sum_{k=1}^{K} A_k^{(1)} \overline{\mathrm{Cos}\Omega_{jk}^{(1)}}$$

to every value of the intensity to make the D.C. term correction and again iterate to a solution yielding the 3K values $x_k^{(2)}$, $y_k^{(2)}$ and $A_k^{(2)}$. The correction procedure may be repeated, each time followed by a new least-squares solution of the coordinates and intensity, although it has been found that subsequent iterations are unnecessary.

Rosenberg (1973) suggests making the D.C. correction by considering the integral-form definition of the mean:

$$\bar{I}_k = \frac{1}{2\pi} \int_0^{2\pi} I_k(\theta) d\theta$$
$$= \tfrac{1}{2} I_{ok} \{1 + \frac{A_k'}{2\pi} \int_0^{2\pi} \mathrm{Cos}(\frac{\pi R_k}{L} \mathrm{Cos}\theta) d\theta \}$$

where

$$\theta \equiv \theta_j + \theta_k$$

and finally

$$\bar{I}_k = \tfrac{1}{2} I_{ok}\{1 + A_k' J_o(\pi R_k/L)\}$$

which demonstrates that the correction can be expressed in terms of the zeroth order Bessel function J_o. These two methods are essentially identical.

If one ignores making the D.C. correction a systematic error is imposed upon the final results. The absolute error is found to be on the order of one or two microns in each coordinate and thus should be avoided. The Bessel function nature of the correction may produce a relative displacement error of several microns between stars if not applied.

E. The Image Parameter σ_k/L

As the solution yields a value for A_k where

$$A_k = \tfrac{1}{2} I_{ok} \frac{4}{\pi} e^{-(\sigma_k \pi/2L)^2} ,$$

one may easily find $\sigma_k \pi/2L$ during the process of correcting for the D.C. term by evaluating

$$\sigma_k/L = \frac{2}{\pi} \left| \{ \ln \left(\frac{2 I_{ok}}{\pi A_k} \right) \} \right|^{\frac{1}{2}} . \qquad (1\text{-}13)$$

However, a problem arises in evaluating I_{ok}. If Eq. (1-12) is used, $\bar{I}$ must be resolved into its K components $\bar{I}_k$,

$$\bar{I}_k \equiv \tfrac{1}{2} I_{ok} + A_k \overline{\mathrm{Cos}\Omega_{jk}} .$$

If one makes the approximation that

$$\bar{I}_k \approx A_k \bar{I} / \sum_{k=1}^{K} A_k ,$$

an approximate value for I_{ok} is given by

$$I_{ok} \simeq 2A_k\left(\frac{\bar{I}}{\sum_k A_k} - \overline{\cos\Omega_{jk}}\right)$$

which is substituted into Eq. (1-13) to give

$$\sigma_k/L \simeq \frac{2}{\pi}\left|\ln\left\{\frac{4}{\pi}\left(\frac{\bar{I}}{\sum_k A_k} - \overline{\cos\Omega_{jk}}\right)\right\}\right|^{\frac{1}{2}} .$$

Thus, an estimate for the image parameter σ_k/L can be made in addition to values for position and intensity.

F. Data Reduction Procedures

The reduction scheme used is similar to that of Smith (1973), although modified to handle more efficiently the laboratory data. The steps implementing the scheme are:

(1) Convert paper tape output into cards and data listing.

(2) Plot number of counts per channel as a function of channel number.

(3) Produce initial estimates of positions and intensities. Previously, a Fourier analysis of the data was performed to produce a contour plot of the focal plane. Here a much simpler method was used. As the low frequency component's location is indicative of position angle and the number of lines in 180° of rotation yields the radial coordinate, (x,y) can easily be calculated by measuring these two values. The low frequency center is found by folding the data about the estimated center and subtracting one half of the data from the other to form a mean residual. The center is then stepped 10 channels on either side of the estimate and the true center value, to the nearest

half channel, can be estimated from the minimum residual. This procedure works for single sources only. When double or multiple sources are used, preliminary calibration runs on each source by itself were routinely made and provided the required initial estimates as well as precise comparison values.

(4) Calculate precise values of positions and intensities. The program used is essentially that of Rosenberg as described by Smith (1973). The I/O is significantly changed and designed for 180° of rotation only. The program also corrects for the D.C. term as described above, calculates $\sigma_{K/L}$, the standard deviation of the residuals and the internal standard errors calculated from the inverse of the matrix containing the co-efficients of the normal equations.

(5) Statistically analyze the results of (4) in the manner appropriate to the particular test problem.

II. The Double Star Source and Imaging Optics

A. Parameters for a Double Star Source

For best performance in resolving binary components, the AMAS must work near the diffraction limit of the optical system to which it is attached. Defining diffraction limited resolution in terms of the Rayleigh criterion means an optical system can resolve two point sources separated such that the central maximum of the diffraction pattern of one source coincides in position with the first minimum of the other source (see Fig. II.1.) If a circular aperture of size a images a point source at wavelength λ, the minimum angle of resolution is

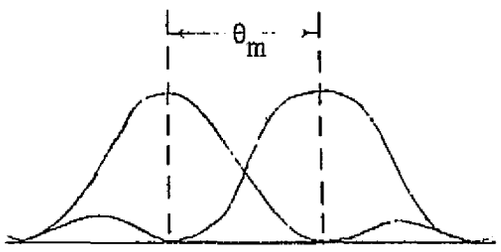

Figure II.1. The Rayleigh Criterion

$$\theta_m = 1.22\frac{\lambda}{a} .$$

Earthbound telescopes are limited by atmospheric "seeing", vitiating attainment of diffraction limited resolution.

As relatively small aperture optics are used in this investigation, it would be generally nonrepresentative to work at the diffraction limit of the test optics. Instead, a situation has been chosen that essentially models the focal plane of a medium-size telescope commonly used for more traditional astrometric work. The example chosen is the new 40-inch astrometric reflector at Fan Mountain with

a focal length of 13.75 meters implying a plate scale of $15\overset{''}{.}0\ \text{mm}^{-1}$ and a minimum angle of resolution of $0\overset{''}{.}14$ at $\lambda = 5600$ Angstroms. The scale and diffraction limit yield a diffraction limited linear separation in the focal plane of

$$d = \frac{0\overset{''}{.}14}{15\overset{''}{.}0}\ \text{mm} = 0.0093\ \text{mm}$$

$$\simeq 10\ \text{microns}\ .$$

To simulate the ideal resolution limit obtainable with a 40-inch telescope, an artificial double star imaged on the Ronchi ruling must have component separations of the order of 10 microns. To demonstrate that the AMAS is competitive with other methods demands that this separation be determined to within a single micron. Furthermore, the artificial double star must span the gamut of expected magnitude differences and position angles. Because of ruling availability, the artificial star images were required to have diameters of over 100 microns to allow σ/L to be approximately 0.5. The value d = 10 microns is kept as a guideline for accurate displacement of the double star components.

B. The "Double Star" Source

The scheme chosen to produce two collimated beams of variable inclination is shown in Figure II.2. Two collimated sources are oriented roughly at right angles and direct beams to the plane-parallel beam splitter whose orientation ultimately determines the focal plane separation d. The beam splitter is rigidly coupled to a geared-down stepping motor

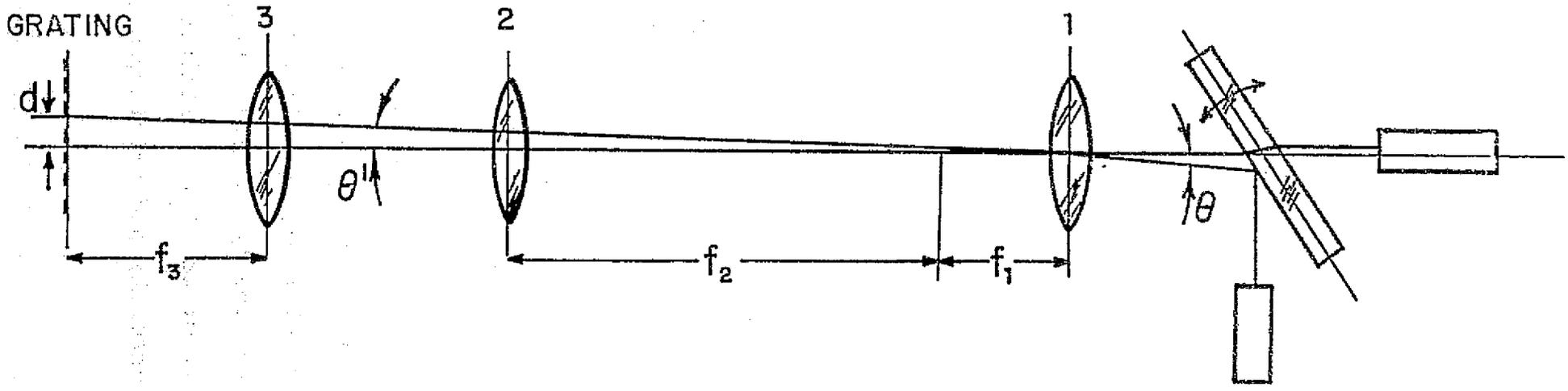

Figure II.2. Schematic Diagram of the Laboratory Double Star Apparatus.

with axis of rotation pointing out of the page. As the beams are collimated, any secondary reflections from the surfaces of the beam splitter remain part of the collimated beam so that no ghost images are produced. Each collimated source was constructed by illuminating a positive photographic enlargement of a high quality image on McCormick plate number 101370 in the focal plane of a coated achromat.

A small rotation of the beam splitter by the amount $\Delta\phi$ is seen to swing the reflected beam through an angle of $2\Delta\phi$ while merely displacing the transmitted beam parallel to itself. The Slo-syn stepping motor may be singly stepped through rotations of $1\overset{\circ}{.}8\pm0\overset{\circ}{.}1$ which are then geared-down by by a factor of approximately 100.

The actual size of $\Delta\phi$ was obtained through a calibration using a very narrow laser beam projected nearly perpendicular onto the beam splitter and measuring the displacements over a baseline of 4.41 meters. The relatively crude procedure of marking the location of a spot of light on a mounted piece of graph paper after each step and taking many groups of 5 step measures yielded

$$\Delta\phi = (1.06\pm0.11)\ \text{step}^{-1} .$$

The larger error than might be expected from the accuracy of the stepping motor may be attributed to backlash in the gears as well as perhaps to the relatively crude calibration procedure. The error in $\Delta\phi$ is certainly no larger than that found.

The absolute and relative brightness of each component

is variable by means of adjusting the voltage on the illuminating bulbs in each source with a precisely controlled voltage divider. The beam splitter can be manually rotated about an axis lying in the plane of Fig. II.2 and parallel to the front and back surfaces so that the two sources may be aligned for zero separation. A dove prism can be inserted in the optical path and used to vary the position angle of the "binary star".

C. Imaging Optics

The optics used to model the focal plane of the 40-inch telescope and to form images of the "double star" on the Ronchi ruling are also shown in Fig.II.2. Simple geometrical optics yields the analysis given below. Lenses 1 and 2 have the function of de-magnifying the angle θ to produce a resulting angular separation θ' given by the relation

$$\frac{\theta'}{\theta} = \frac{f_1}{f_2} \quad . \qquad (2\text{-}1)$$

Lens 3, of focal length f_3, serves as an objective to form the image onto the ruling. In its focal plane the scale is given by

$$S = \frac{206265}{f_3} \ (\text{arcsec}\cdot\text{mm}^{-1}). \qquad (2\text{-}2)$$

From Eq.(2-1)

$$S = \frac{\theta'}{d} = \frac{\theta f_1}{d f_2} \ ,$$

so using Eq.(2-2) gives the relation for the image separation distance, d,

$$d = \frac{\theta f_1 f_3 / f_2}{206265} \ \ (\text{mm}) \ , \qquad (2\text{-}3)$$

where θ is in arcseconds and the f's are in mm.

For an f_3 of 193 mm, and letting $r \equiv f_1/f_2$, then Eq.(2-3) becomes

$$d = \frac{\theta r}{1069} \quad (\text{mm}),$$

$$= \frac{r\Delta\phi}{534.4} \quad , \qquad (2\text{-}4)$$

as $\theta = 2\Delta\phi$. If $\Delta\phi$ is expressed in arc-minutes, this equation becomes

$$d = 0.1123r\Delta\phi. \qquad (2\text{-}5)$$

As $\Delta\phi$ is 1!06±0!11 step^{-1}, Eq.(2-5) in terms of integral multiples of $\Delta\phi$ becomes

$$d = (0.119\pm0.012)nr \quad (\text{mm}) \; . \qquad (2\text{-}6)$$

Eq.(2-6) is used to construct the following table that allows selection of a suitable value for r.

Table II.1. - Incremental Focal Plane Distances from Equation (2-6)

r \ n	1	2	5	10	15	
1	.119	.238	.595	1.190	1.786	
.20	.024	.048	.119	.238	.357	
.10	.012	.024	.060	.119	.179	d(mm)
.04	.005	.010	.024	.048	.071	
.01	.001	.002	.006	.012	.018	

Table II.1 shows the ratio of focal lengths for the demagnifying lenses can be between .10 and .04. On this basis optics with the characteristics listed in Table II.2 were selected.

Table II.2. - Parameters for the Optics in the Double Star Source

Lens #	focal length (mm)	aperture (mm)
1	88	42
2	1016	52
3	193	52

Thus, r = 88/1016 ≈ 0.0866 and d as a function of step number n is given by

$$d = 0.0103n \quad (\text{mm}) , \qquad (2\text{-}7)$$

i.e. each step is 10.3 microns.

D. Error Analysis

To determine the error associated with Eq.(2-7), it will be assumed that all the variable in Eq.(2-3) are independent and the error may then be written as

$$(\Delta d)^2 = (\frac{\delta d}{\delta \theta}\Delta\theta)^2 + (\frac{\delta d}{\delta f_1}\Delta f_1)^2 + (\frac{\delta d}{\delta f_2}\Delta f_2)^2 + (\frac{\delta d}{\delta f_3}\Delta f_3)^2 . \qquad (2\text{-}8)$$

Upon evaluation Eq.(2-8) becomes

$$(\Delta d)^2 = (1.00\times10^{-3})^2 + (\Delta f)^2\{(1.17\times10^{-4})^2 + (1.01\times10^{-5})^2 + (5.34\times10^{-5})^2\} ,$$

where it is assumed that

$$\Delta f_1 = \Delta f_2 = \Delta f_3 = \Delta f$$

so

$$(\Delta d)^2 = (1.00\times10^{-3})^2 + (1.60\times10^{-8})(\Delta f)^2 .$$

If the rather liberal error of 4 mm in the focal lengths is assumed, then

$$\Delta d = 1.19\times10^{-3} \text{ mm.}$$

The largest error contribution is from the uncertainty in the mirror stepping angle. However, the final error is certainly acceptable and the controllable image-separation step increment on the ruling of the AMAS is

$$d = 10.3\pm1.2 \text{ microns.} \qquad (2\text{-}9)$$

The optical system described above was completely set up in the Photocathode Laboratory at the McCormick Observatory.

III. Laboratory Testing Procedure

A. General Guidelines

The advantage of evaluating the AMAS in the laboratory is the freedom to control various parameters precisely. As the ill effects of atmospheric seeing and telescope jitter are completely eliminated, a space environment and a high degree of pointing stability are simulated easily.

The list of parameters against which the AMAS has been tested fall rather naturally into two overall categories. The first grouping consists of those instrumental parameters - ruling line spacing and precision, rotation rate, dwell time per channel, distance of field center from ruling rotation center, σ/L, integration time, etc. - over which the observer normally has control. The second grouping consists of cosmical parameters - double and multiple star separations, position angles and magnitude differences, background star density and distribution, etc. - which the observer must normally accept as they are encountered. Each of these parameters may be varied uniformly and independently in the laboratory to produce clearly defined results.

B. Definitions

The terms precision and accuracy are used in the strict sense, that is the degree of freedom from random and systematic errors respectively. In practice precision is determined by

making five observations of a single star image with no variations of parameters between integrations. The root-mean-square deviations in the reduced co-ordinates are then taken as the precision in those co-ordinates. Because of uncertainty in the repeatability of lamp illumination, the precision of magnitude determination is not given here. Accuracy is determined by making five or more observations of a single source while stepping the mirror through one rotation increment between observations. The reduced coordinates are then used to calculate the observed mean stepping increment and the r.m.s. deviation from that value. The observed value for d may then be compared with the calibrated value for d (Section II.D.) to determine the accuracy of the AMAS.

The ability of the AMAS to resolve double stars may be determined in one of two equivalent ways. The first way is to make separate observations of each component with the other component turned off. A third observation with both components illuminated may be reduced and compared with the solutions for the separate components. The alternative method is to add the signals of the single components to numerically produce a double star signal. This latter technique has the advantage of eliminating random errors that occur between observations of the stars separately and together. The number of observing runs is also significantly reduced. For example, the procedure used here to evaluate resolution as a function of some parameter is as follows: (a) visually align the two

components so that their centers coincide, (b) step one component away from the other to give an initial separation of some value known to be unresolvable (this was normally 60 microns for sources with diameters of ∿ 120 microns), (c) turn the stationary component off and make twelve observations of the single source with one step of 10.3 microns between observations (this produces a range of separations between 60 and 180 microns), (d) turn the movable component off and make up to five observations of the stationary source while varying its intensity between observations. These 17 runs may then be combined to make 60 equivalent observations of a double star with uniformly varying separation and magnitude difference. Unless otherwise stated, the separation steps are made in the R direction. If the first method of actually observing the combined stars had been used, a total of 180 observations would have been necessary. This expediency reduces the observing time from 30 to 2.8 hours, over 90% of which time is used for punching paper tape. Also, long observing runs decrease the homogeneity of the series of observations with the prototype due to time-varying characteristics of the AMAS-optical bench system. These problems result primarily from the level of engineering incorporated in the prototype.

Initially, a test series was made both ways, giving no indication that the method adopted is invalid. A further check was made by adding four separate runs of the same star and comparing the results of the combined observation with

the mean results of the individual runs. The difference in position was less than 0.1 micron and less than one count in intensity for a source with R/L = 20.2485, $\theta = 51^{\circ}.1641$, m = 10.2 and $N_{chan} = 384$. These differences are within the tolerance of the solution as explained in Section I.C. Fields of up to ten stars were generated in the same manner.

C. Signal Strength Expressed as Apparent Magnitude

In order to model a real observational situation, it is desirable to have laboratory star images with intensities similar to actual stars. Thus, it would be helpful to have a magnitude system that would provide a reasonable estimate of the equivalent apparent magnitudes of the laboratory stars.

The usual defining relation for magnitude is

$$m = \frac{5}{2}\text{Log}\frac{1}{1_o} \quad , \qquad (3\text{-}1)$$

where 1_o is the apparent luminosity for a star of m = 0. Code (1960) gives a flux value of 3.8×10^{-9} erg·cm^{-2}·sec^{-1}·Å $= 6.45\times10^{3}$ photons·in^{-2}·sec^{-1}·Å for a star of V = 0.00 above the atmosphere. This may be used in the above expression to derive a magnitude system of

$$m = 2.5\text{Log}\frac{(6.45\times10^{3})(\pi A^{2})(T_{int})(\Delta\lambda)(q)}{I_o} \qquad (3\text{-}2)$$

where 2A ≡ Aperature of telescope = 40 inches

T_{int} ≡ Integration time per channel ≡ D·N_{rot}

D ≡ Dwell time per channel (seconds)

N_{rot} ≡ Number of observed ruling rotations

$\Delta\lambda$ ≡ Passband of system ≃ 2500 Å

q ≡ Quantum efficiency of the system ≃ 0.1

I_o ≡ Integrated intensity of the Gaussian image. (Given by the solution in counts/channel)

Equation (3-2) may finally be written as

$$m = 2.5\text{Log}\frac{(2.03\times10^{9})(D)(N_{rot})}{I_o} \qquad (3\text{-}3)$$

D. Laboratory Test Schedule

A Ronchi ruling of 100 lines/inch (implying L = 0.127mm) was used throughout. This coupled with the observed value of $\sigma/L \simeq 0.5$ gives image diameters of 120 microns. This also leads to first and third order damping terms of 0.69 and 165×10^{-3} allowing safe exclusion of the third order term which is only 0.2% of the first. Integration times corresponding to 400 rotations were commonly used along with a dwell time of 80 μsec. The mean period of ruling rotation is 76.75 msec. This combination requires 479.7 channels to record 180^0 of rotation. Only the first 180^0 of rotation is used since the suggestion of Rosenberg (1972) to add the two half rotations together is safe only for highly constant rotation rate.

The list of tests carried out in the laboratory in order to evaluate the AMAS is given in Table III.1. The parameters chosen represent a reasonable sample of possible

observational and cosmical variables expectected during a real observational program.

Table III.1. AMAS Laboratory Test Schedule

NUMBER	DESCRIPTION	NUMBER	DESCRIPTION
1.1	P(R)	3.1	$\mathbb{R}(\rho;\ \delta m=o)$
1.2	P(S/N)	3.2	$\mathbb{R}(\rho;\ \delta m\neq 0)$
1.3	$P(N_{chan})$	3.3	$\mathbb{R}$(P.A.; A(P.A.))
		3.4	$\mathbb{R}$(R)
2.1	A(R)	3.5	$\mathbb{R}$(S/N)
2.2	A(S/N)	3.6	$\mathbb{R}(N_{chan})$
2.3	$A(N_{chan})$	3.7	$\mathbb{R}$(Distribution of background stars)

Abbreviations

P	Precision
A	Accuracy
$\mathbb{R}$	Resolution
R	Distance from center of rotation
S/N	Signal to noise ration
N_{chan}	Number of channels in 180^0
ρ	Double star linear separation (microns)
P.A.	Double star position angle
δm	Double star magnitude difference

IV. Laboratory Test Results

A. Instrumental Precision

1.1 P(R)

The position precision is expected to decrease for objects located at increased distances from the center of rotation for two related reasons. First, for a fixed number of channels the resolution in detecting the high frequency components generated by sources at large R is diminished. Second, the effects of uncertainty in the position angle of the ruling at any instant of time are directly proportional to R. This latter effect obtains always a greater precision in the R coordinate than in the Rθ coordinate even at small values of R. Factors influencing the precision in R reduce primarily to the precision in the line spacing of the Ronchi ruling. Examples of AMAS signals at small and large values of R/L are shown in Fig IV. 1.1.

The trend in precision with increasing R/L is shown in Fig IV.1.2. Data from a total of 55 observations of single stars has been reduced to determine r.m.s. deviations in the R and θ directions as well as the internal error associated with the (x,y) determinations. Out to R/L $\sim$ 70, the mean rms errors are (in microns)

$$\bar{\sigma}_R = 0.8,\ \bar{\sigma}_\theta = 1.5,\ \bar{\sigma}_i = 0.3\ .$$

At values of R/L = 187 and 216, the overall precision is clearly diminishing in a somewhat erratic manner. The last value of R/L

shows an uncertainty in θ of over six times the uncertainty in R. Clearly observations at this large a distance from the center of rotation are of little value unless the rotation rate is highly constant.

It may be concluded that the uncertainty in the θ direction is generally about twice that in R. The uncertainty transmitted to (x,y) values may then be expected to be 1.5 microns in either coordinate.

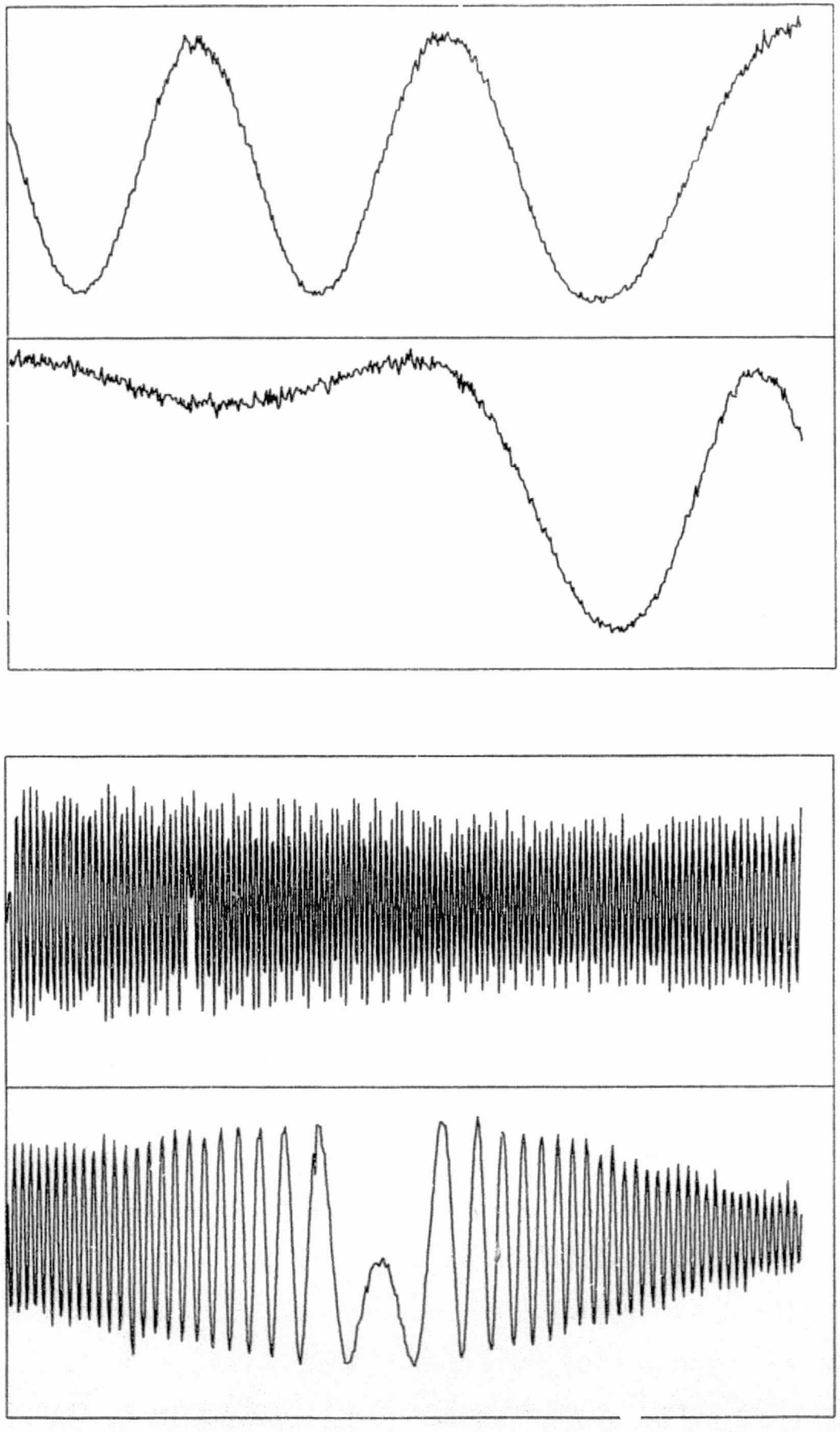

Figure IV.1.1. Examples of AMAS Signals for (a) R/L = 4.3024, $\theta = 67^{0}.6458$, m = 9.7 and N_{chan}= 960; (b) R/L = 187.3700, θ = 47.4400, m = 9.3 and N_{chan}= 960.

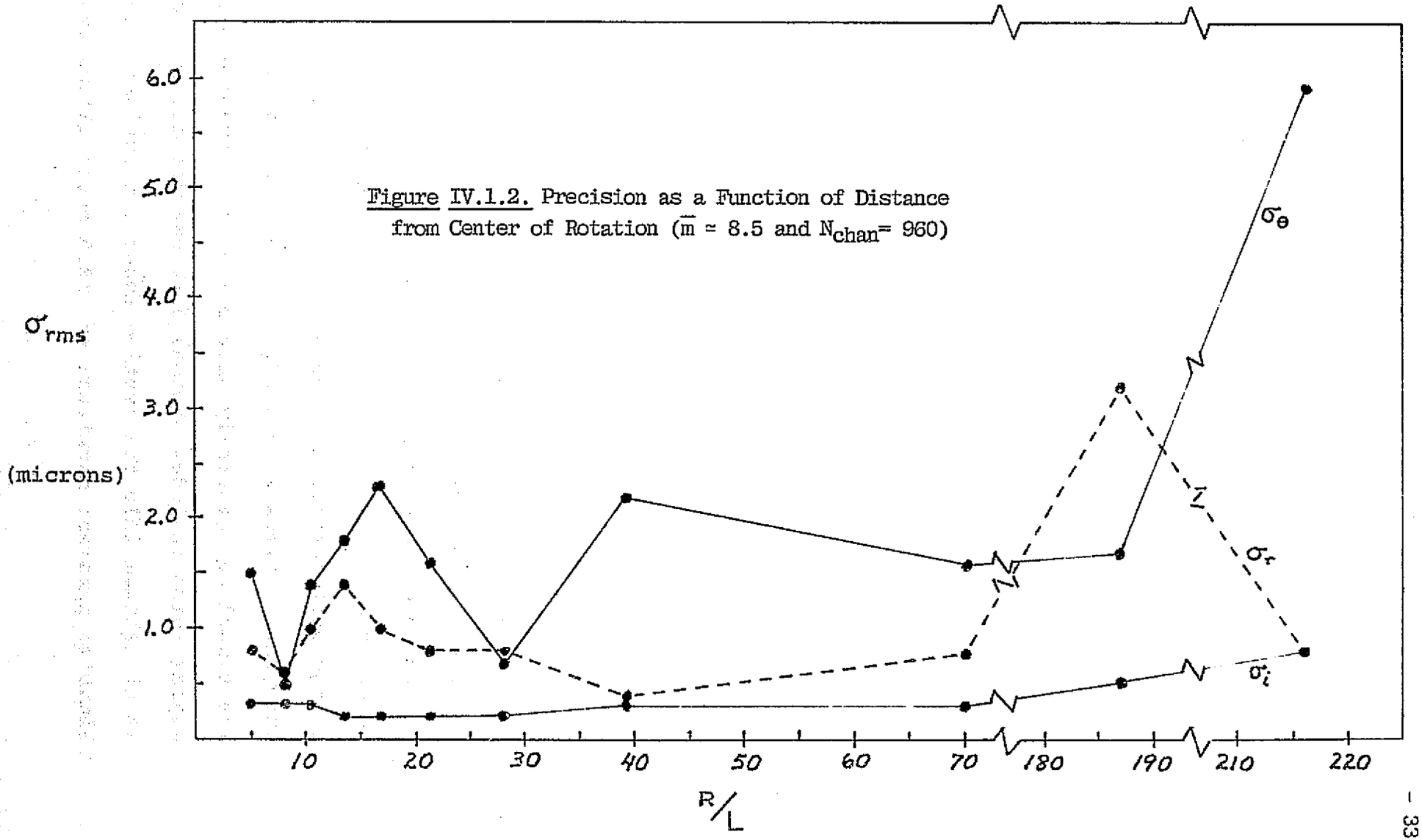

Figure IV.1.2. Precision as a Function of Distance from Center of Rotation ($\bar{m} \simeq 8.5$ and $N_{chan} = 960$)

1.2 P(S/N)

The effects of decreasing signal to noise are shown in Fig IV. 1.3. where the rms deviations in R and θ are shown as a function of magnitude. A value representing a signal to noise ratio has been formed from the ratio $\bar{A}/\bar{\sigma}$ where $\bar{A}$ is the mean amplitude of the signal and $\bar{\sigma}$ is the mean standard deviation of the residuals from the least squares fit to the signal. Table IV.1. gives the observed correspondence between m and S/N for the data.

Table IV.1. Correspondence Between Apparent Magnitude and Signal to Noise Ratio.
(m is calculated from Eq. (3-3))

m	S/N	m	S/N
8.8	10.9	13.9	1.7
11.2	8.0	14.7	1.1
11.9	5.8	15.0	0.9
12.5	3.8	15.3	0.7

Again, as shown in Fig. IV.1.3., the precision in R is generally better than in θ, with both better than 1.5 microns down to nearly apparent magnitude 13. Presumably, acceptable precision could be extended to fainter magnitudes if the photomultiplier tube were cooled and/or if longer integration times were used. At the faint end of the data, the signal was generally only 20% or so above the background signal which includes thermal dark current and any residual light leakage into the testing apparatus optical path. A limiting apparent magnitude of 12.0 still allows the prototype

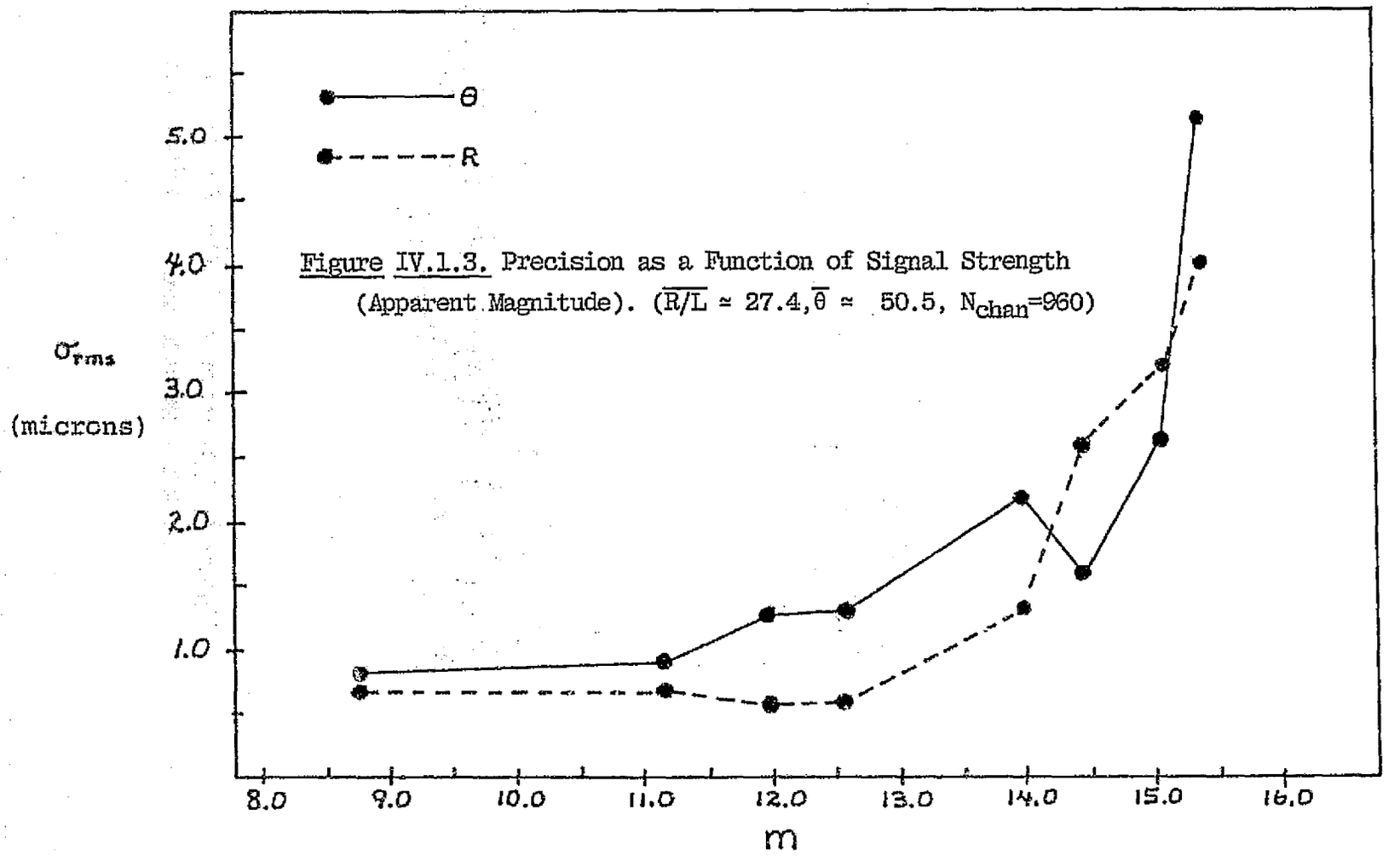

Figure IV.1.3. Precision as a Function of Signal Strength (Apparent Magnitude). ($\overline{R/L} \simeq 27.4, \overline{\theta} \simeq 50.5$, N_{chan}=960)

AMAS to pursue typical parallax studies where reference star magnitudes are around 11.0. An example of a signal from a faint star is shown in Figure IV.1.4.

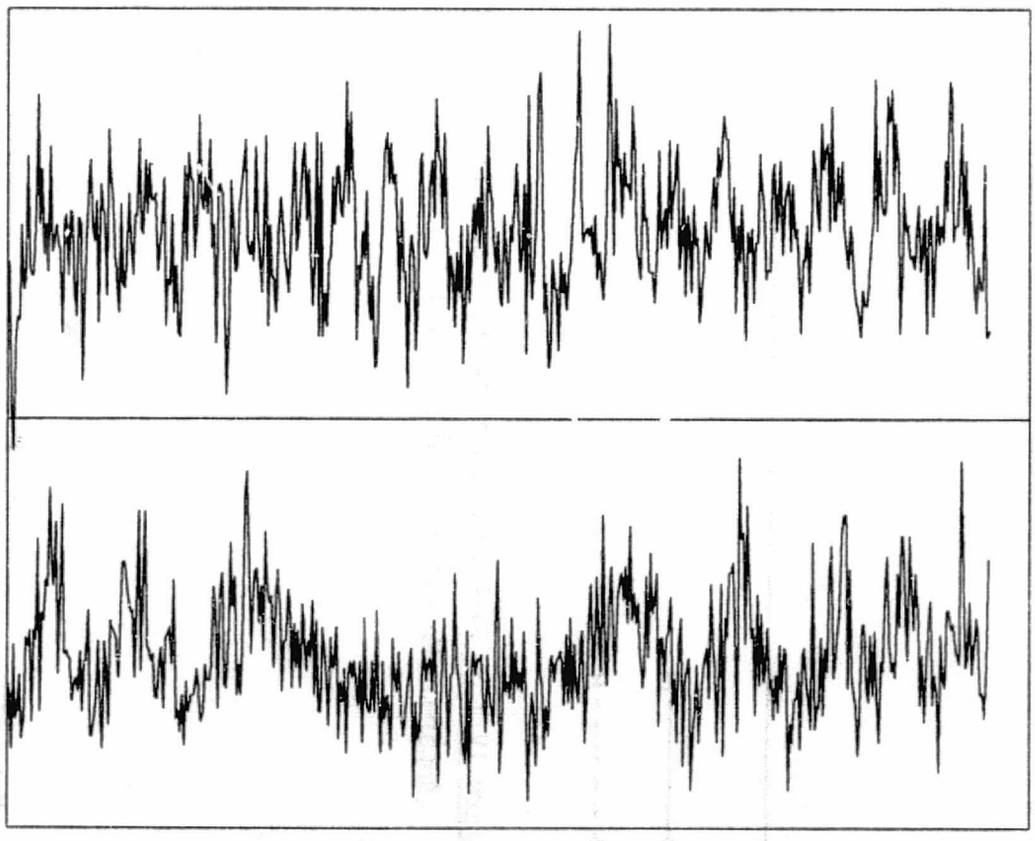

Figure IV.1.4. Example of AMAS Signal for a Star of m = 14.9 at R/L = 27.1916 and $\theta = 50^{\circ}.5214$ with $N_{chan} = 960$.

1.3 $P(N_{chan})$

The number of channels used to record the signal generated by the AMAS is an important factor. The number used here was constrained principally for reasons of economy. The data readout time in the present system is directly proportional to the record length; this severely inhibits obtaining a large number of observations in a single session. However, if too few channels are used, the form of the high frequency component is lost. Thus, it is desirable to find a compromise in the record length. Figure IV.1.5. shows an example of the same star as observed with widely different record lengths. Much of the high frequency information is lost in the signal with fewer channels. However, the two solutions converge within 30 microns so that the absense of high frequency definition does not prohibit convergence to an approximate solution entirely for this particular case.

Results for a range of record lengths are presented in Figure IV.1.6. The largest error is in σ_θ for N_{chan} = 480. This value was obtained from six observations, one of which is decidedly removed from the others and is possibly spurious. If this observation is ignored, σ_R and σ_θ become 0.4 and 1.0 microns. The overall high precision for small record lengths may largely be explained by the increase in dwell time per channel so that both noise and registration inaccuracies from non-constant ω are greatly smoothed out

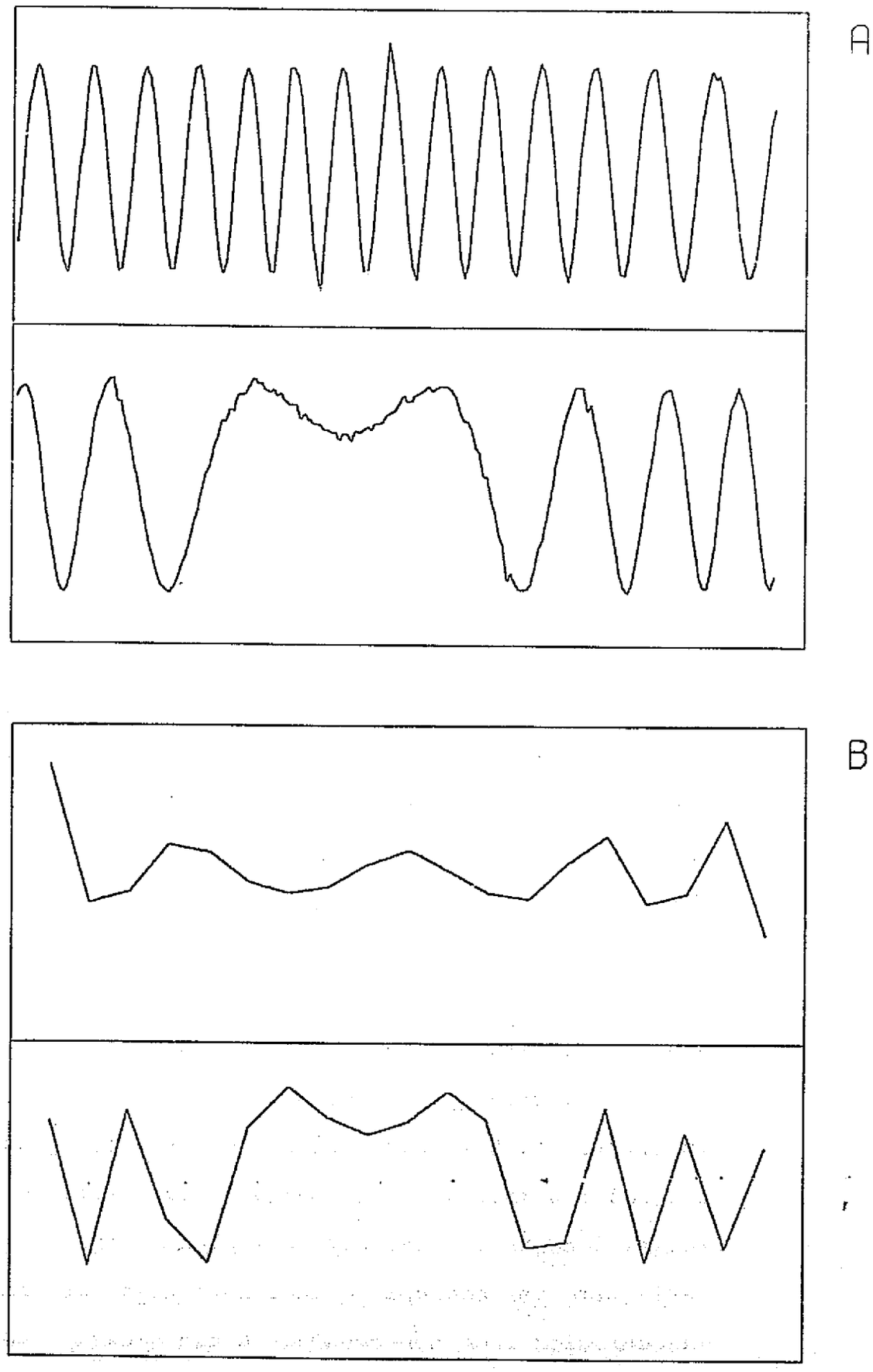

Figure IV.1.5. Example of AMAS Signals for (a) N_{chan}= 384, R/L = 20.3298, $\theta = 51^{0}.0352$ and m = 9.3; (b) N_{chan}= 38, R/L = 20.3156, $\theta = 50^{0}.4003$ and m = 10.7.

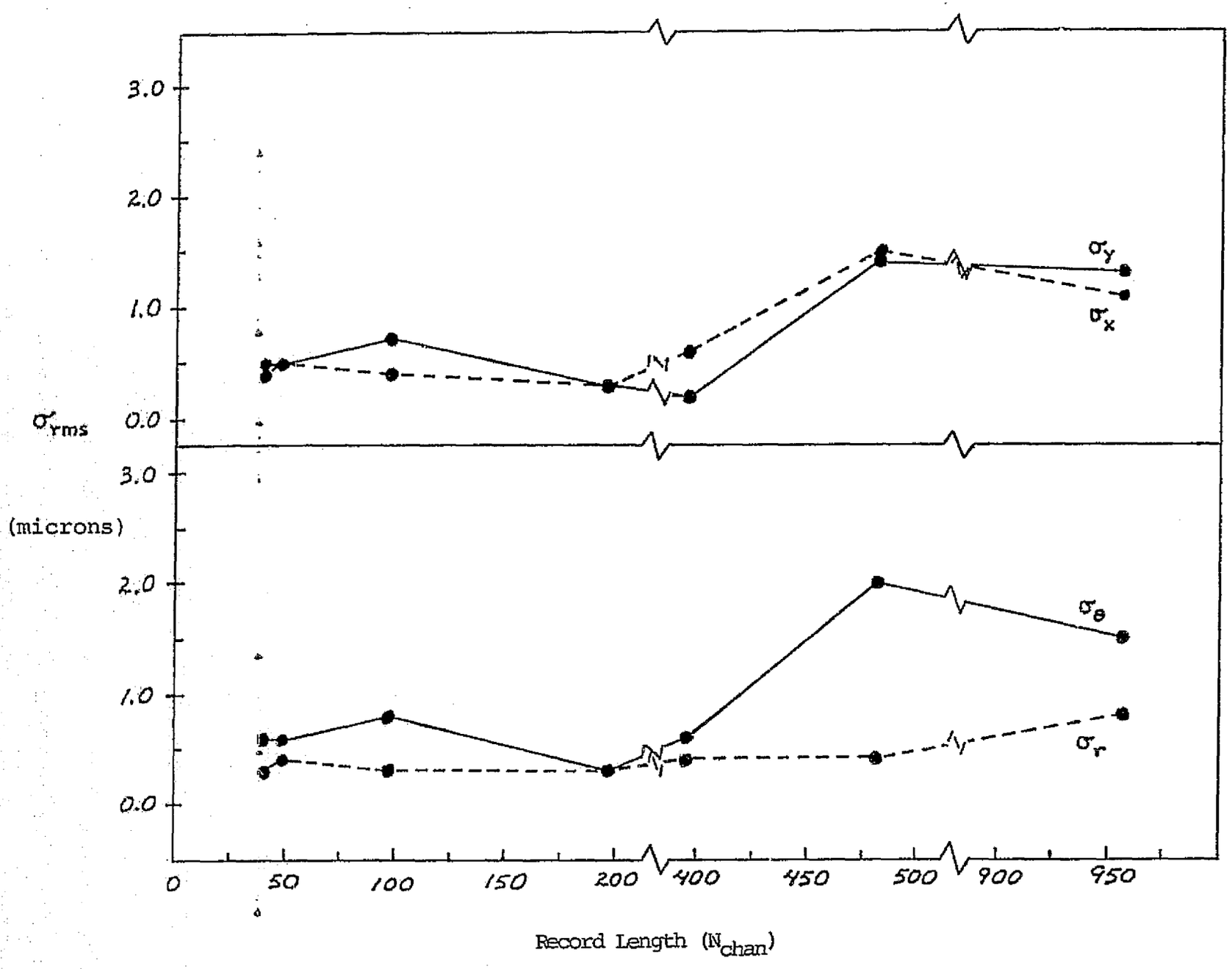

Figure IV.1.6. Precision as a Function of Record Length.
($\overline{R/L} \approx 20.3$, $\overline{\theta} \approx 51.0$ and $\overline{m} \approx 10.6$)

in any one channel. Thus, one would expect a high degree of repetition among observations with fewer channels. Observations carried out subsequent to this series were limited to 480 channels except where the record length was the independent variable.

B. Instrumental Accuracy

2.1 A(R)

Figure IV.2.1. shows the results of a series of observations investigating the accuracy of the AMAS as the distance from the center of rotation is increased. The upper part of the diagram gives the mean value of the step size in a series of five observations. In these tests of accuracy, the orientation of the optics was such that the 10.3 micron step was principally in the R coordinate. Thus, least squares fits of astraight line were performed on each data set to calculate the residuals x_{ri} and y_{ri} of the i^{th} observation that leads to an error in the θ - direction given by

$$\Delta\theta_i = x_{ri}\mathrm{Sin}\{\mathrm{Tan}^{-1}(y_{ri}/x_{ri})\}$$

The mean value of the $\Delta\theta_i$ may then be taken as the accuracy in the θ - direction.

The lower panel of Figure IV.2.1. indicates a step size agreement between observed and calibrated values to generally within a single micron. The r.m.s. deviations are least for values of R/L between 40 and 100. Omitting the values at R/L = 216, the means (in microns) are:

$$\langle\Delta r\rangle = 10.0$$

$$\langle\sigma_{\Delta r}\rangle = 1.3$$

$$\langle\sigma_{\Delta\theta}\rangle = 1.3$$

$$\langle\sigma_i\rangle = 0.4$$

where σ_i is the internal error of solution.

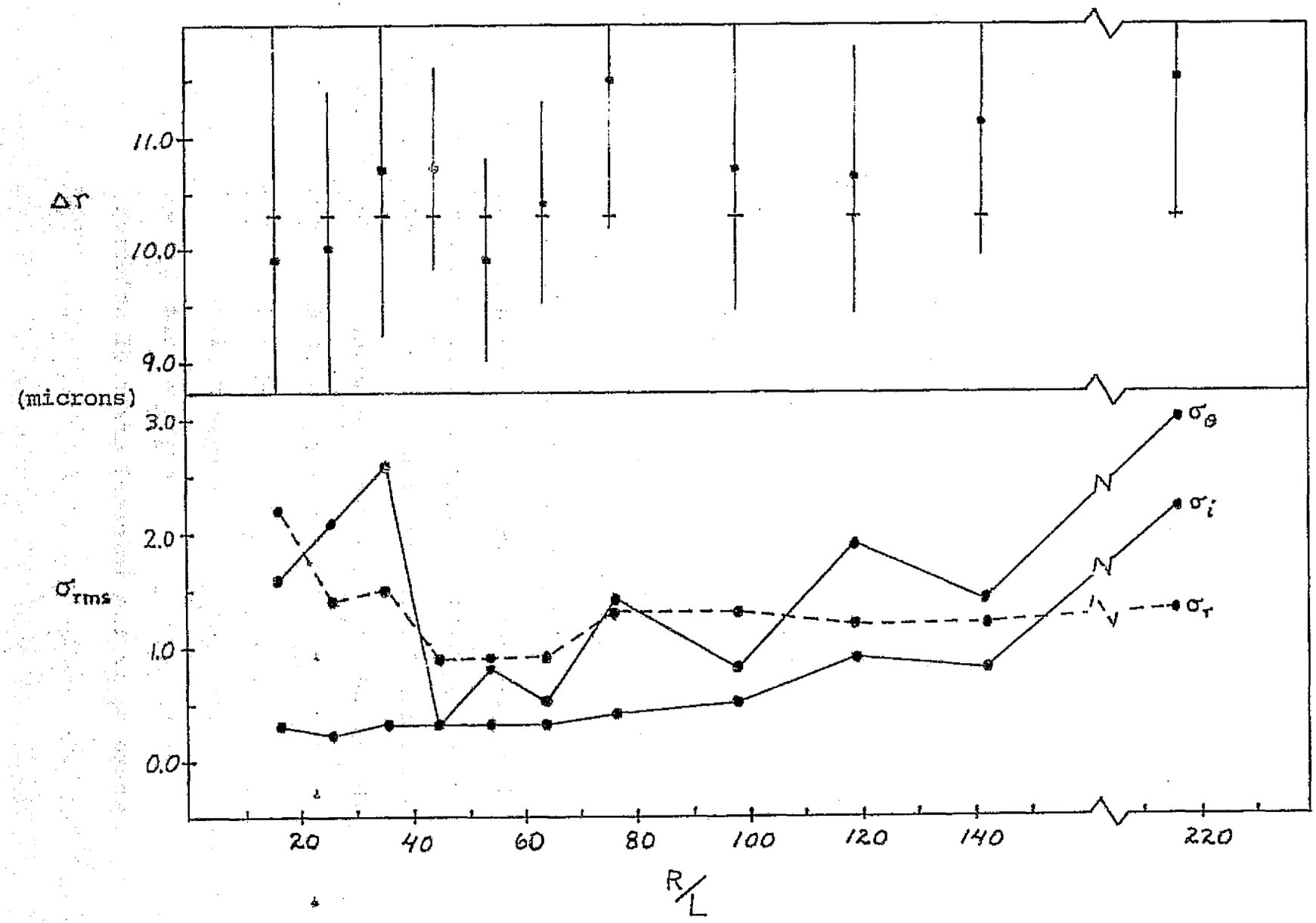

Figure IV.2.1. Accuracy as a Function of Distance from Center of Rotation ($\bar{m} \approx 10.0$).

2.2 A(S/N)

Figure IV.2.2. shows results for AMAS accuracy as a function of apparent magnitude. The upper part indicates the deviation of the observed step size from the calibrated step size by means of arrows. The accompanying r.m.s. deviations are also shown. It is interesting to note that, although it behaves erratically, beyond m≈13.0 σ_r is noticably greater than σ_θ. Additional points are shown at around m≈15.2 for integrations increased from 400 rotations to 800 ($\Delta r_1, \sigma_{r1}, \sigma_{\theta 1}$) and to 4000 ($\Delta r_2, \sigma_{r2}, \sigma_{\theta 2}$) rotations. Thus, increased integration time dramatically extends the limiting magnitude of the AMAS.

2.3 A (N_{chan})

The results for AMAS accuracy as a function of record length as shown in Fig. IV.2.3 Over the range of 38 to 960 channels observations of a star at R/L ~ 22 lead to values of Δr all within the calibration accuracy. The observed r.m.s. deviations are however unacceptable for N_{chan} = 38 and 48. Excluding values at these two points, one finds that (in microns):

$$\langle \Delta r \rangle = 10.4$$

$$\langle \sigma_{\Delta r} \rangle = 0.9$$

$$\langle \sigma_{\Delta \beta} \rangle = 0.8$$

$$\langle \sigma_i \rangle = 0.5$$

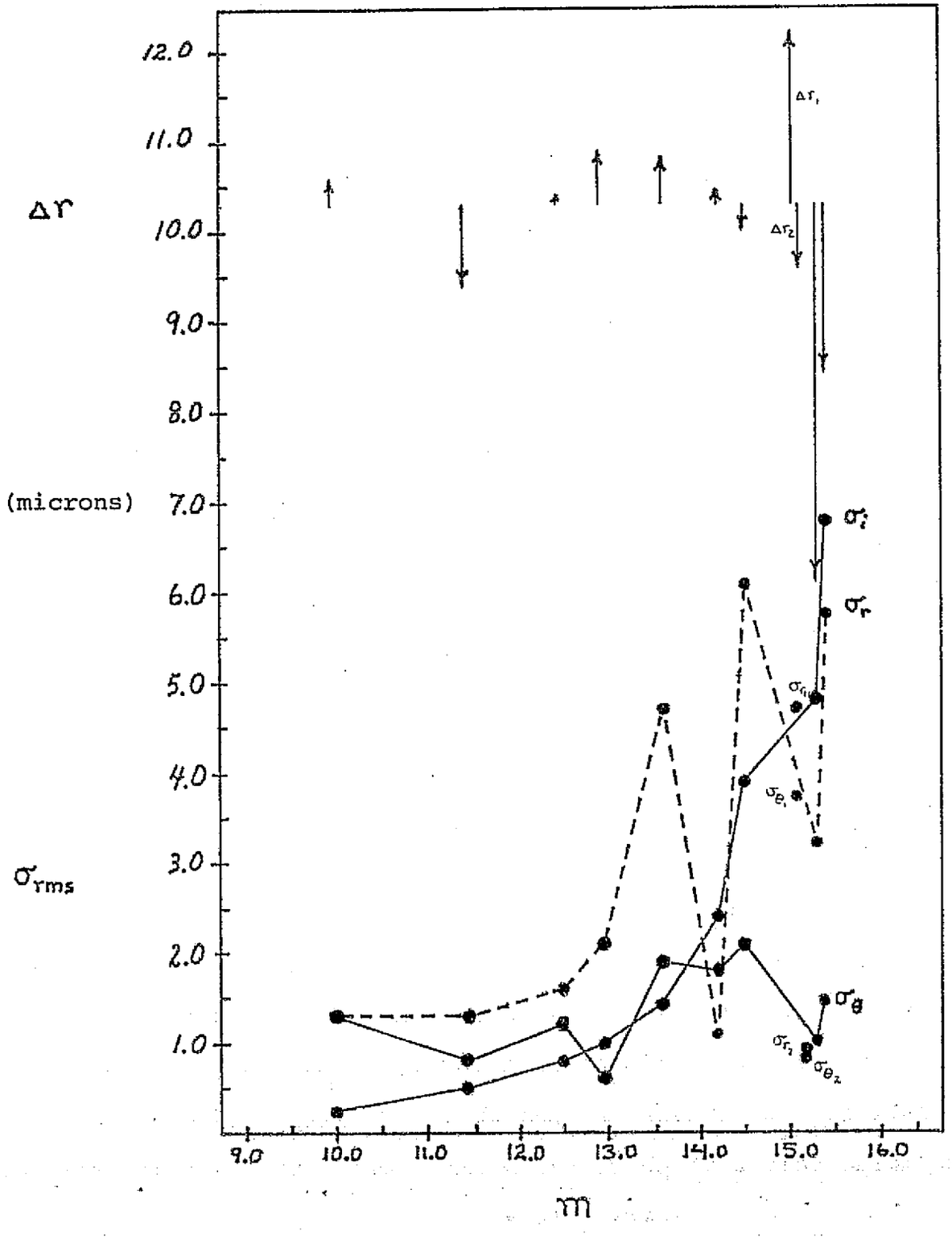

Figure IV.2.2. Accuracy as a Function of Apparent Magnitude
($\overline{R/L} \simeq 22.3$, $\overline{\theta} \simeq 56.3$, N_{chan}=480)

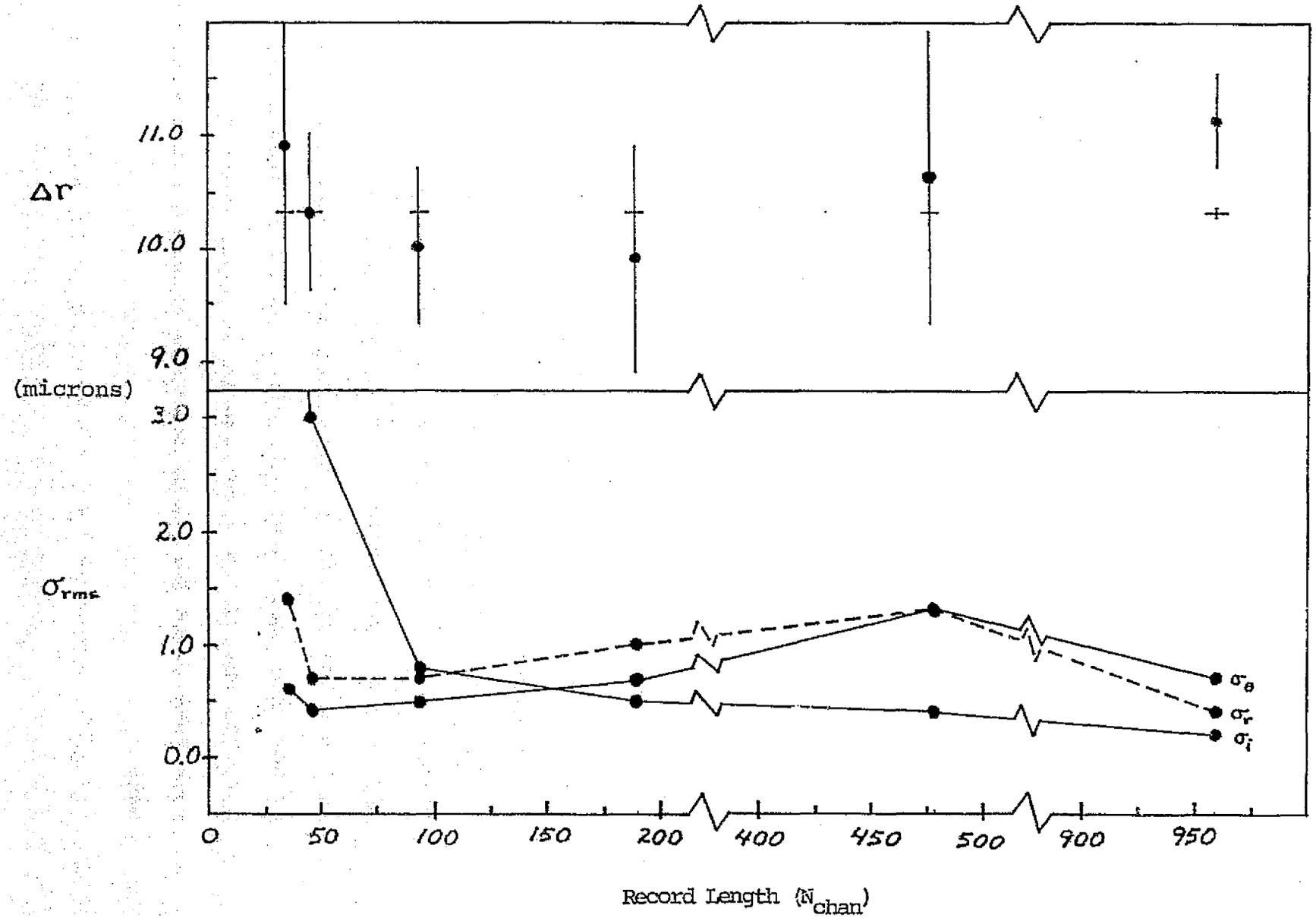

Figure IV.2.3. Accuracy as a Function of Record Length
($\overline{R/L} \approx 22.3$, $\bar{\theta} \approx 56.3$, $\bar{m} \approx 10.0$)

C. Instrumental Resolution

Up to this point the experimental results have all pertained to observations of single stars. These observations establish the degree of confidence to be attached to a single observation of a single star. The next series of test results are for double stars observed as described under Section III.B.

3.1, 3.2 $R(\rho,\delta m)$

The results for this series are shown in Figures IV. 3.1, IV. 3.2 and IV. 3.3, which are essentially self-explanatory. In these figures, errors in separation (ρ), position angle (P.A.$=\mathrm{Tan}^{-1}(\rho_y/\rho_x)$), magnitudes (apparent (m) and differential (δm)) and (R,θ) coordinate directions are plotted as functions of the actual separation ρ_A for various values of δm. Each figure contains additional explanatory information.

For a δm of near zero and image diameter $\sim$120 microns, error in the separation becomes acceptable at $\rho\sim$120 microns although the error in position angle does not diminish to 1° until $\rho\sim$130 microns. For increasing δm, the errors in ρ and P.A. increase systematically but tend to approach an acceptable limit at $\rho\sim$180 microns. For values of $\rho_m \geq 4.0$ the errors in separation become negative. Whether or not they again approach zero is not indicated here. It is possible that $\delta m \simeq 4.0$ represents an upper limit to the dynamic magnitude range for simultaneously observed stars with the AMAS.

Figure IV.3.1. Errors in (ρ,P.A.) as Functions of Separation and δm. ($\overline{R/L} \simeq 31.0$, $\overline{\theta} \simeq 52.^{\circ}6$, $m_{primary} \simeq 10.0$ and $N_{chan} = 480$)

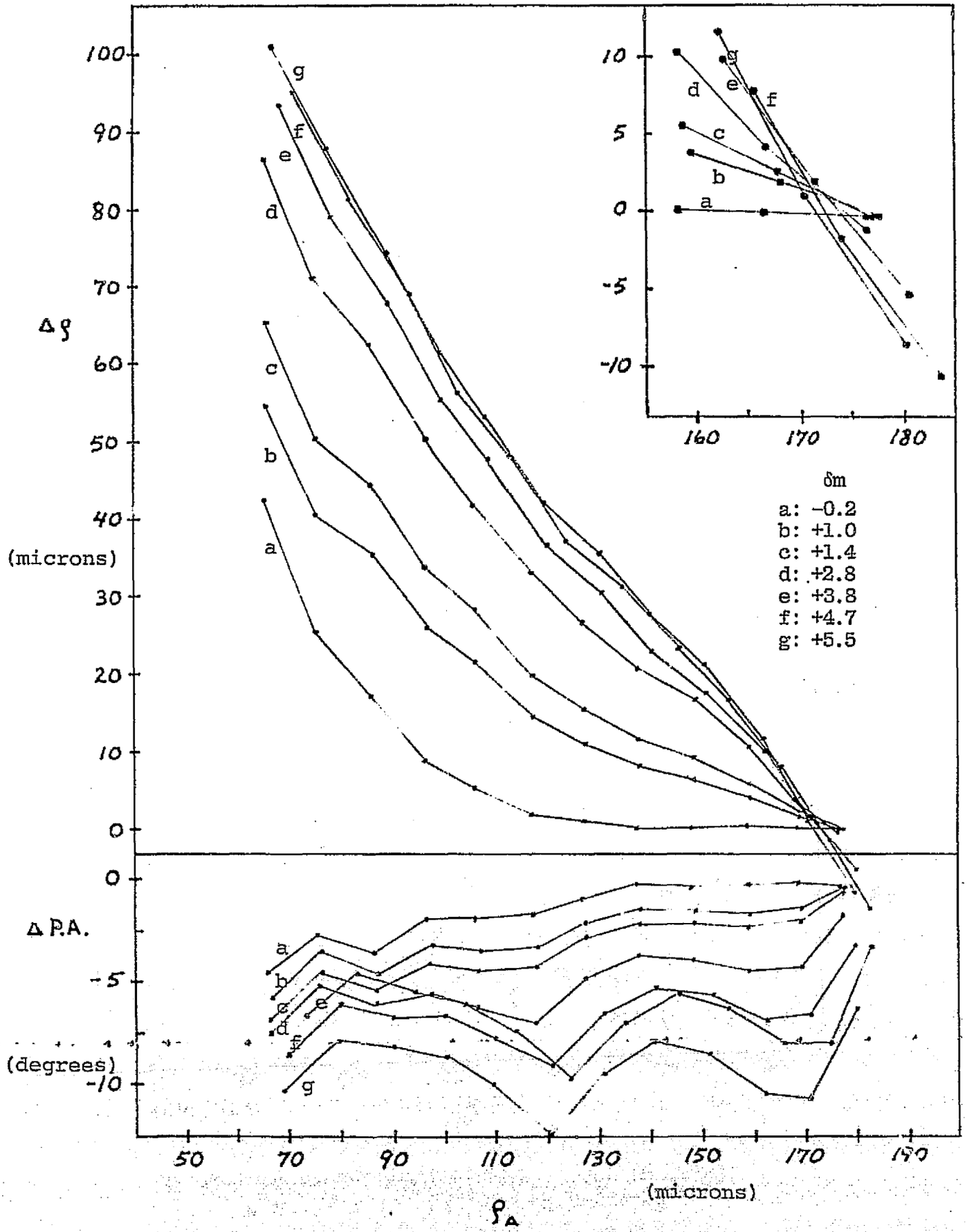

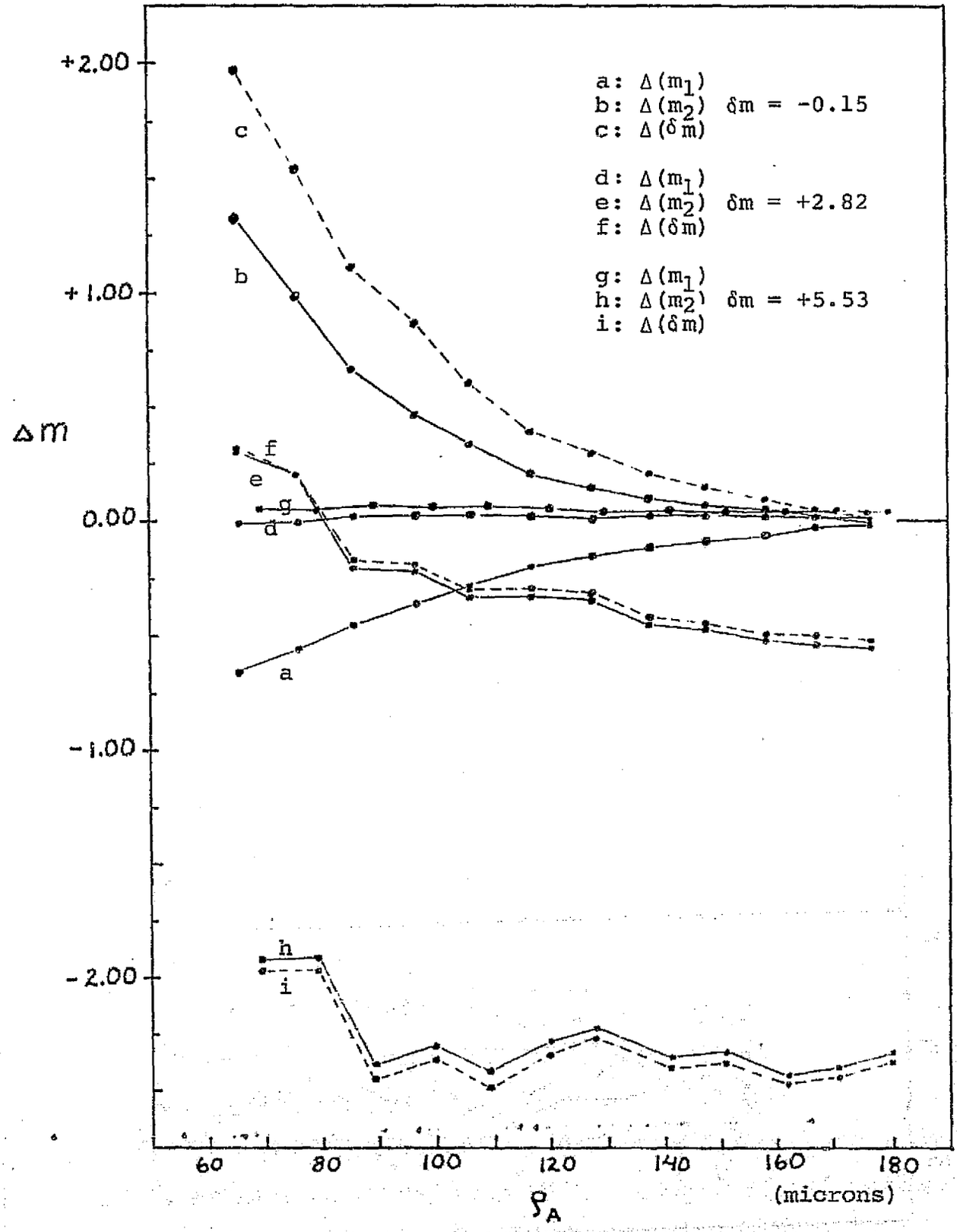

Figure IV.3.2. Errors in Magnitudes as Functions of Separation and δm. ($\overline{R/L} \simeq 31.0$, $\overline{\theta} \simeq 52.6$, $m_{primary} \simeq 10.0$ and $N_{chan} = 480$)

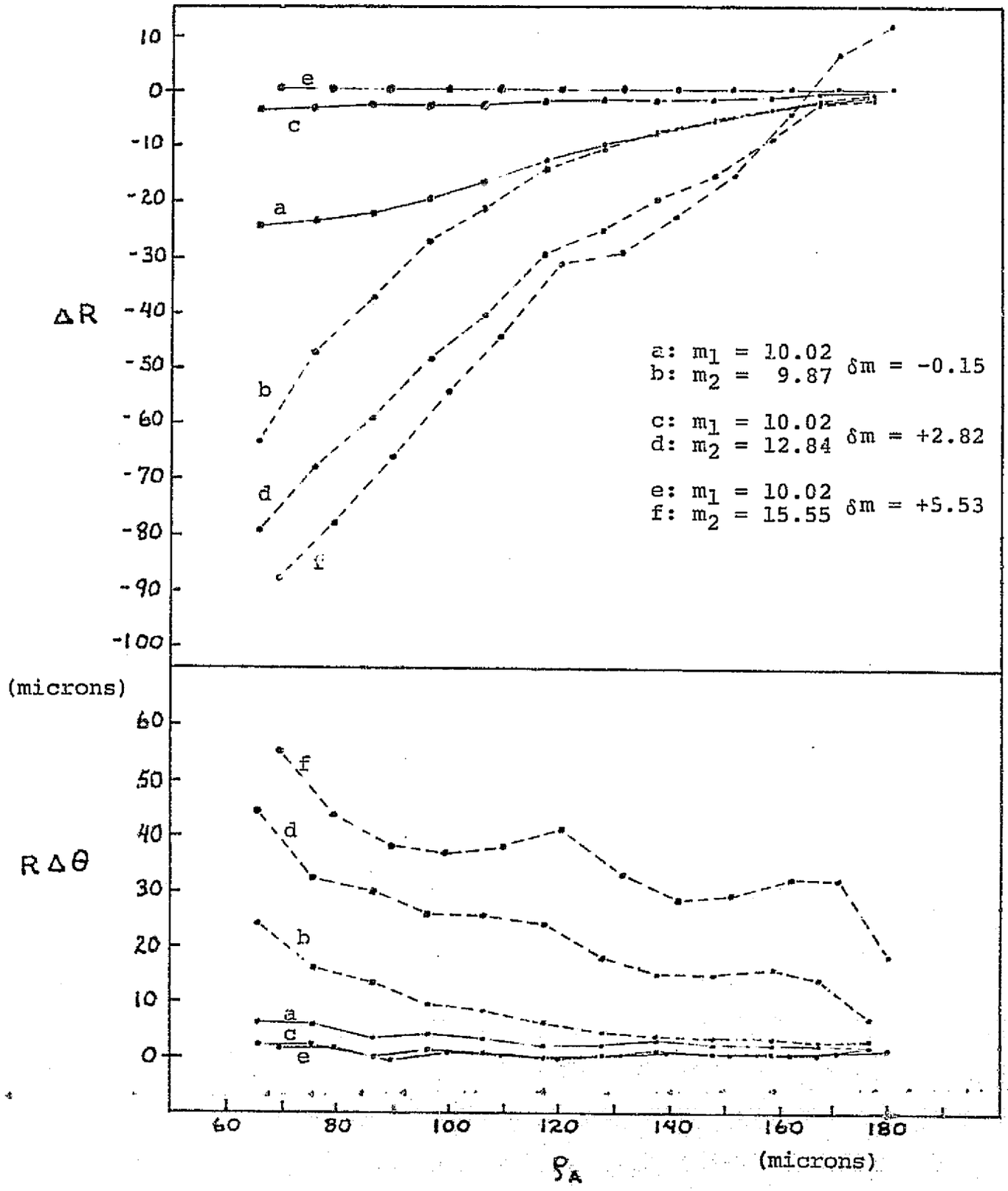

Figure IV.3.3. Errors in (R,θ) Coordinate Directions as Functions of Separation and δm. ($\overline{R/L} \simeq 31.0$, $\overline{\theta} \simeq 52.^{0}6$, $m_{primary} \simeq 10.0$ and $N_{chan} = 480$)

Figures IV. 3.2 and IV. 3.3 give results that are generally to be expected, that is, errors in position and brightness increase for the fainter component and decrease for the brighter component with increasing δm.

3.3 R(P.A., A(P.A.))

An additional test series to establish the general trend in resolution was carried out with the direction of separation rotated 90^0, i.e. the two components oriented perpendicular to the radius vector originating from the center of rotation and bisecting the separation vector. This was done by placing a dove prism in the test apparatus optical path with the proper orientation. The results of this series are shown in Figures IV.3.4., IV.3,5, and IV.3.6.

For a $\delta m \sim 0$, the error in separation becomes less than one micron at $\rho \sim 116$. However, the error in position angle is less than one degree at $\rho \sim 70$, a significant improvement over the previous binary orientation. A second set for $\delta m \sim 1.6$ shows somewhat erratic behavior. Solutions for this combination could not be obtained for $\rho_A < 99$ microns. Figure IV.3.6. indicates that the error in R for the faint component diverges from reasonable agreement at $\rho \sim 110$ microns and only starts to decrease again at $\rho \sim 170$ microns.

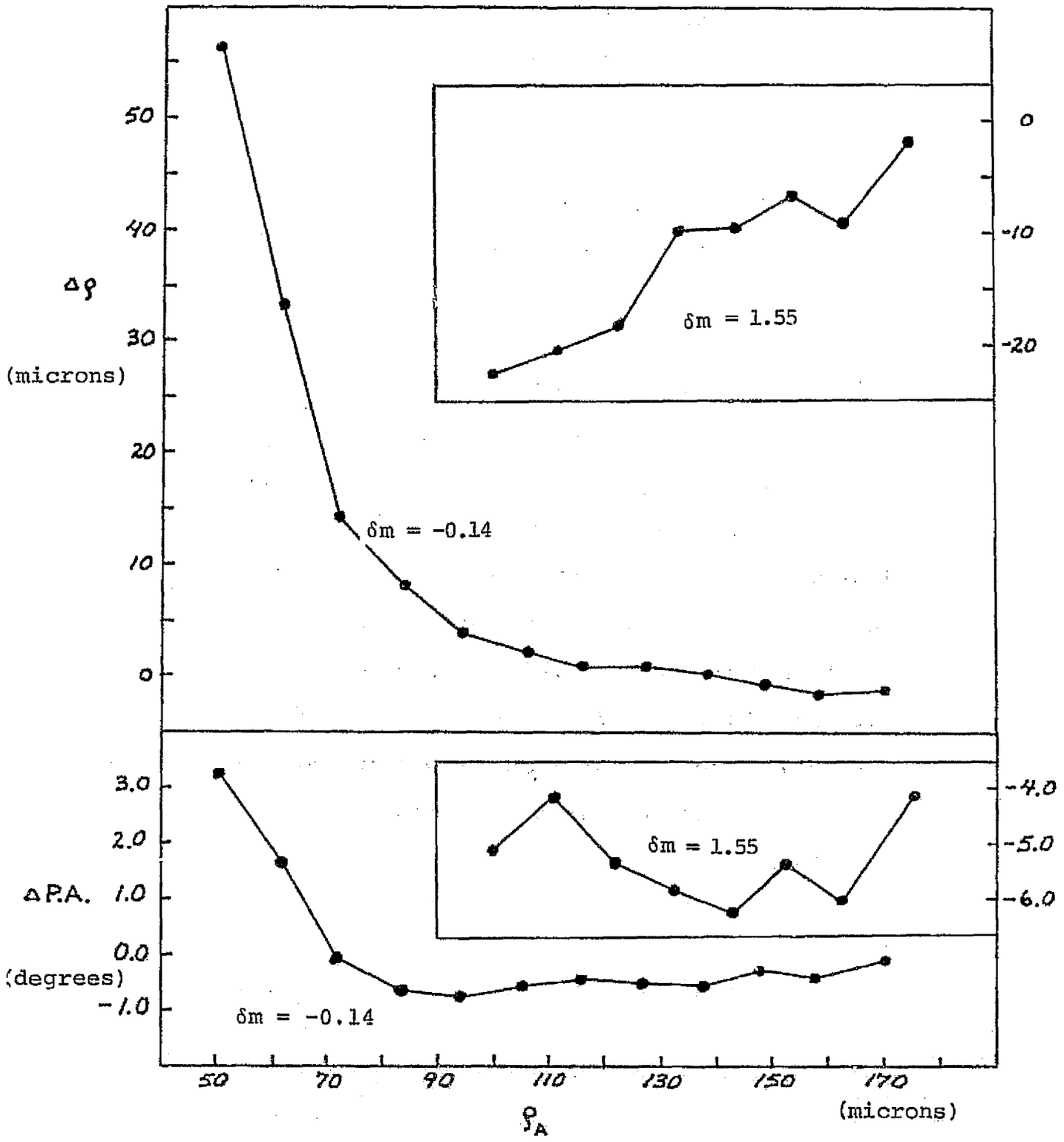

Figure IV.3.4. Errors in (ρ,P.A.) as Functions of Separation and δm for P.A. Rotated by 90^0. ($\overline{R/L} \simeq 26$, $\overline{\theta} \simeq 55\overset{0}{.}7$, $m_{primary}=9.91$)

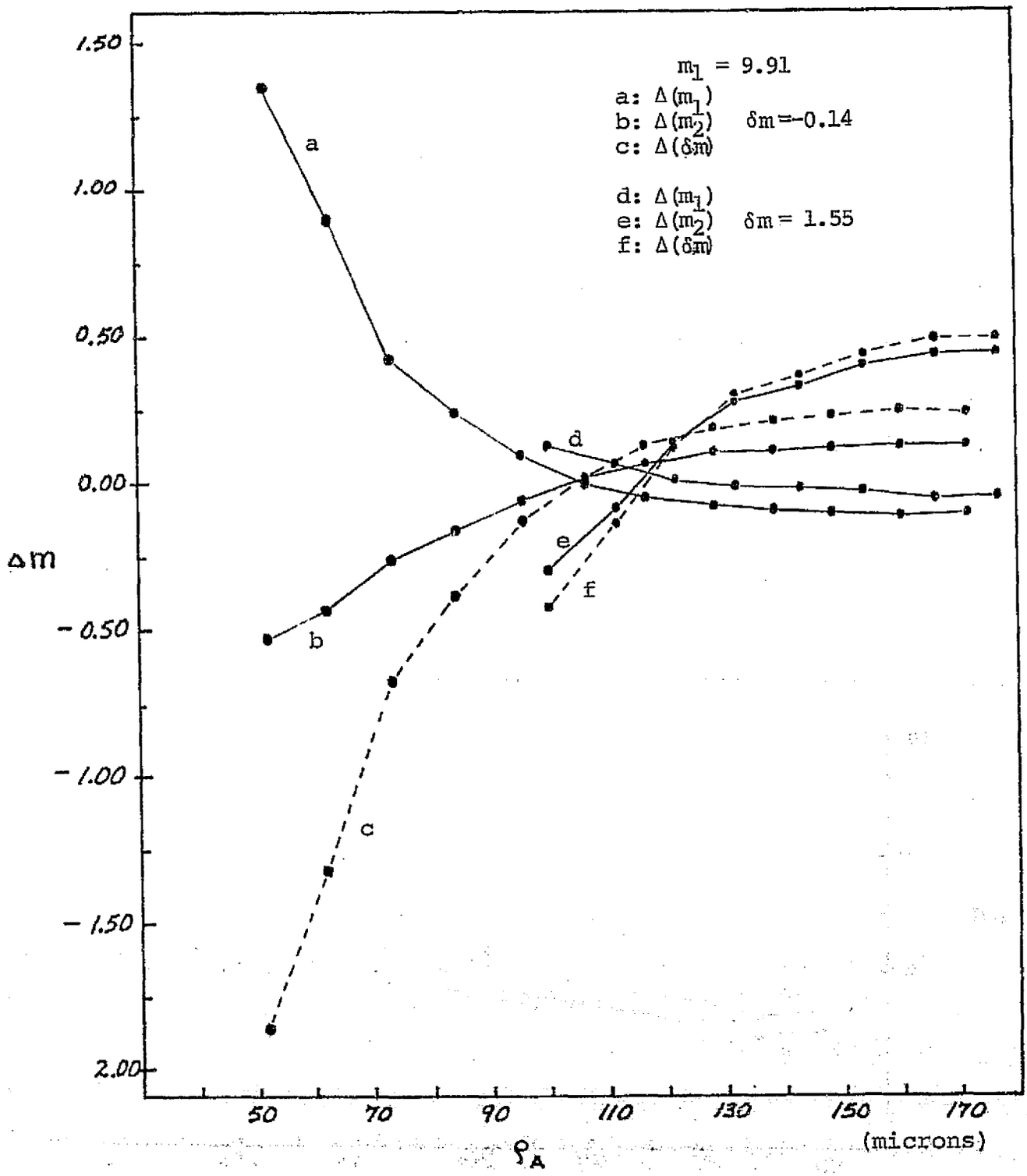

Figure IV.3.5. Errors in Magnitudes as Functions of Separation and δm for P.A. Rotated by 90°.
($\overline{R/L} \simeq 26$, $\overline{\theta} \simeq 55°.7$, $m_{primary}$=9.91)

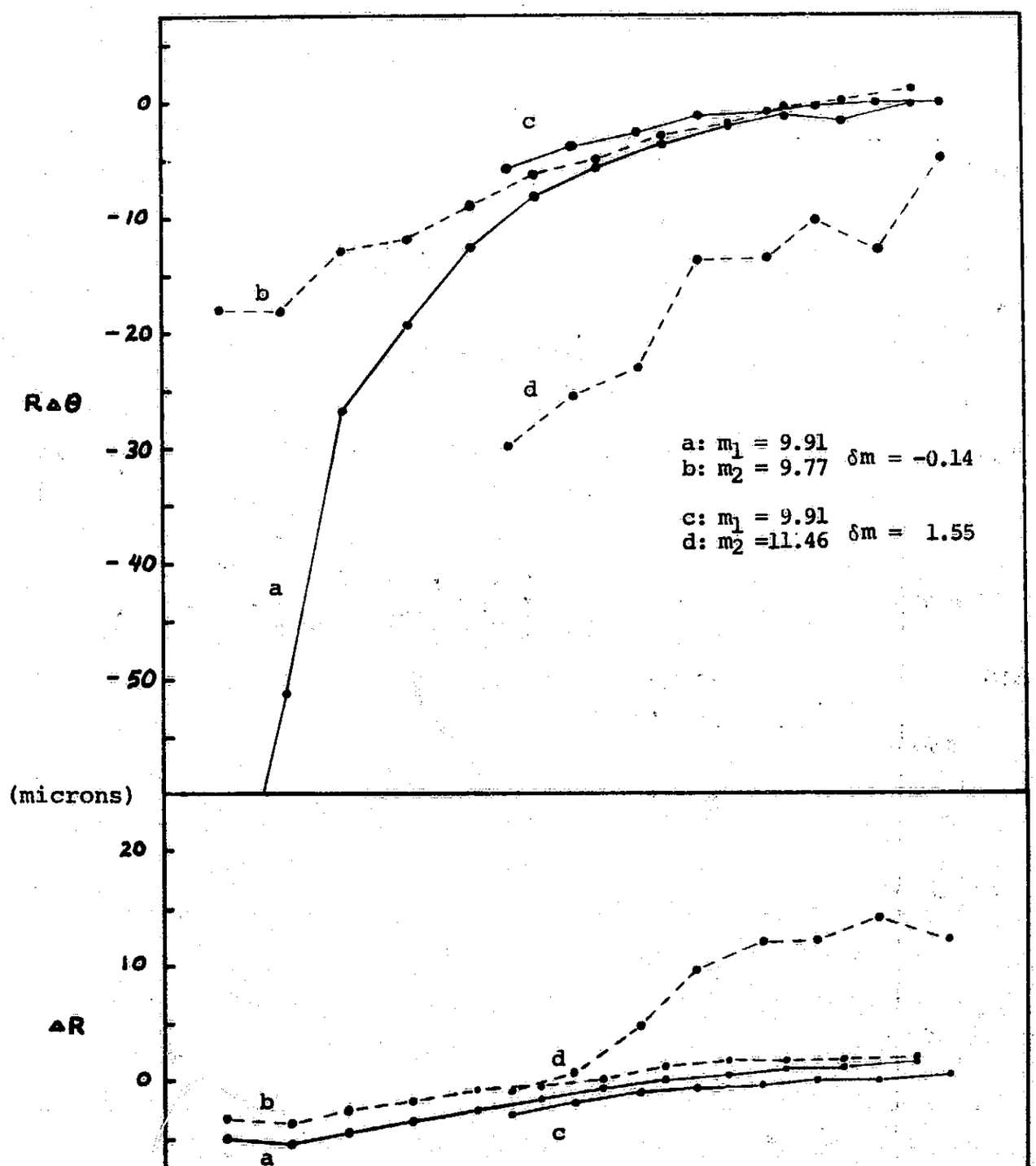

Figure IV.3.6. Errors in (R,θ) Coordinate Directions as Functions of Separation and δm for P.A. Rotated by 90°. ($\overline{R/L} \approx 26$, $\overline{\theta} \approx 55°.7$, $m_{primary}=9.91$)

3.4 R(R)

Figures IV.3.7. through IV.3.10. summarize the results for double stars observed at values for R/L of 131 and 188 with δm values of 0.1 and 1.7 of each value of R/L. The results indicate that these values of R/L are already straining the ability of the AMAS to accurately resolve double stars. The errors in separation for $\delta m \sim 0.1$ drop rapidly to one micron at $\rho \sim 105$ microns but immediately begins to diverge. In this and succeeding tests, the binary components are oriented in the R direction.

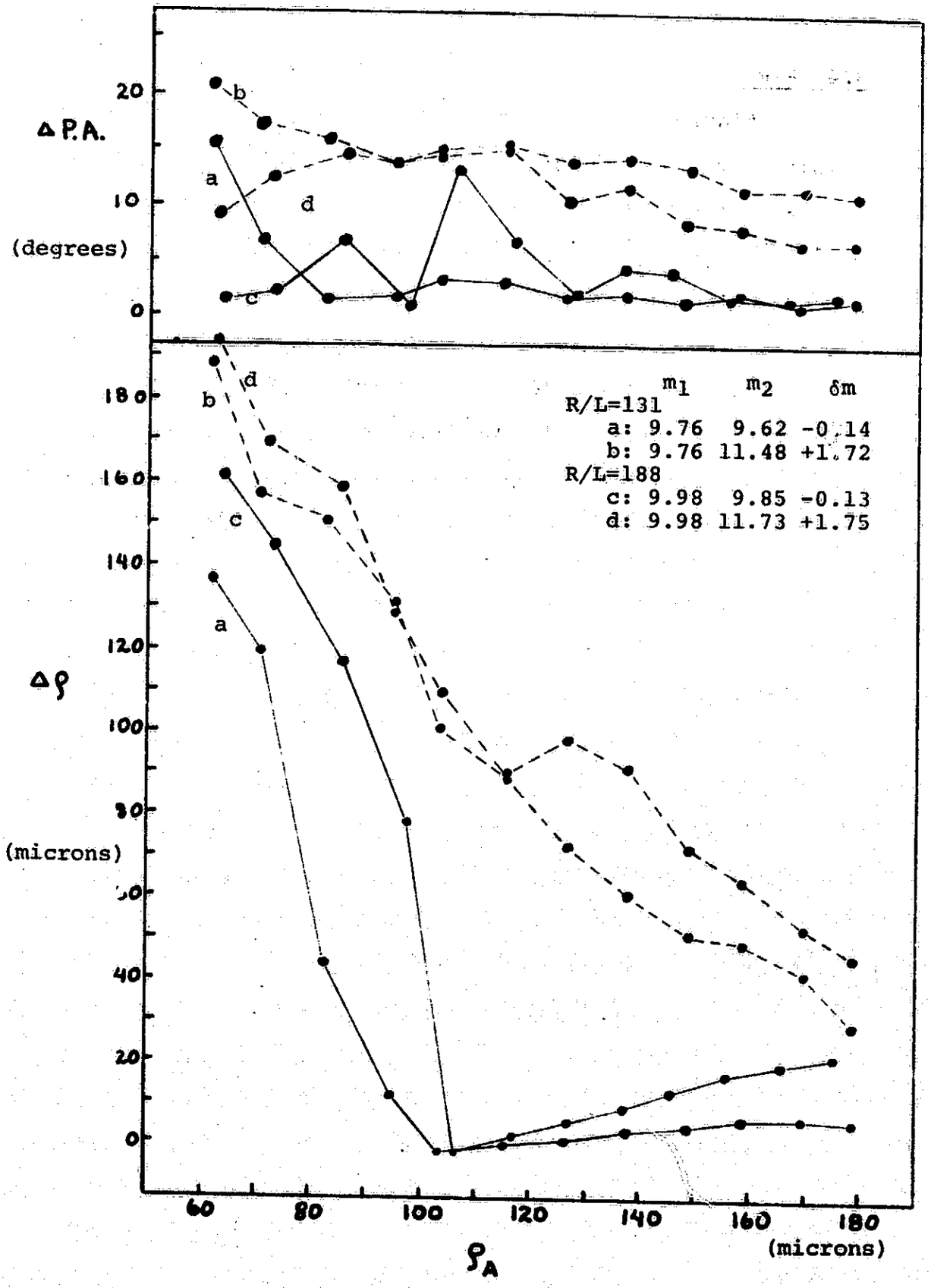

Figure IV.3.7. Errors in (ρ,P.A.) as Functions of Separation, δm and Distance from Center of Rotation.

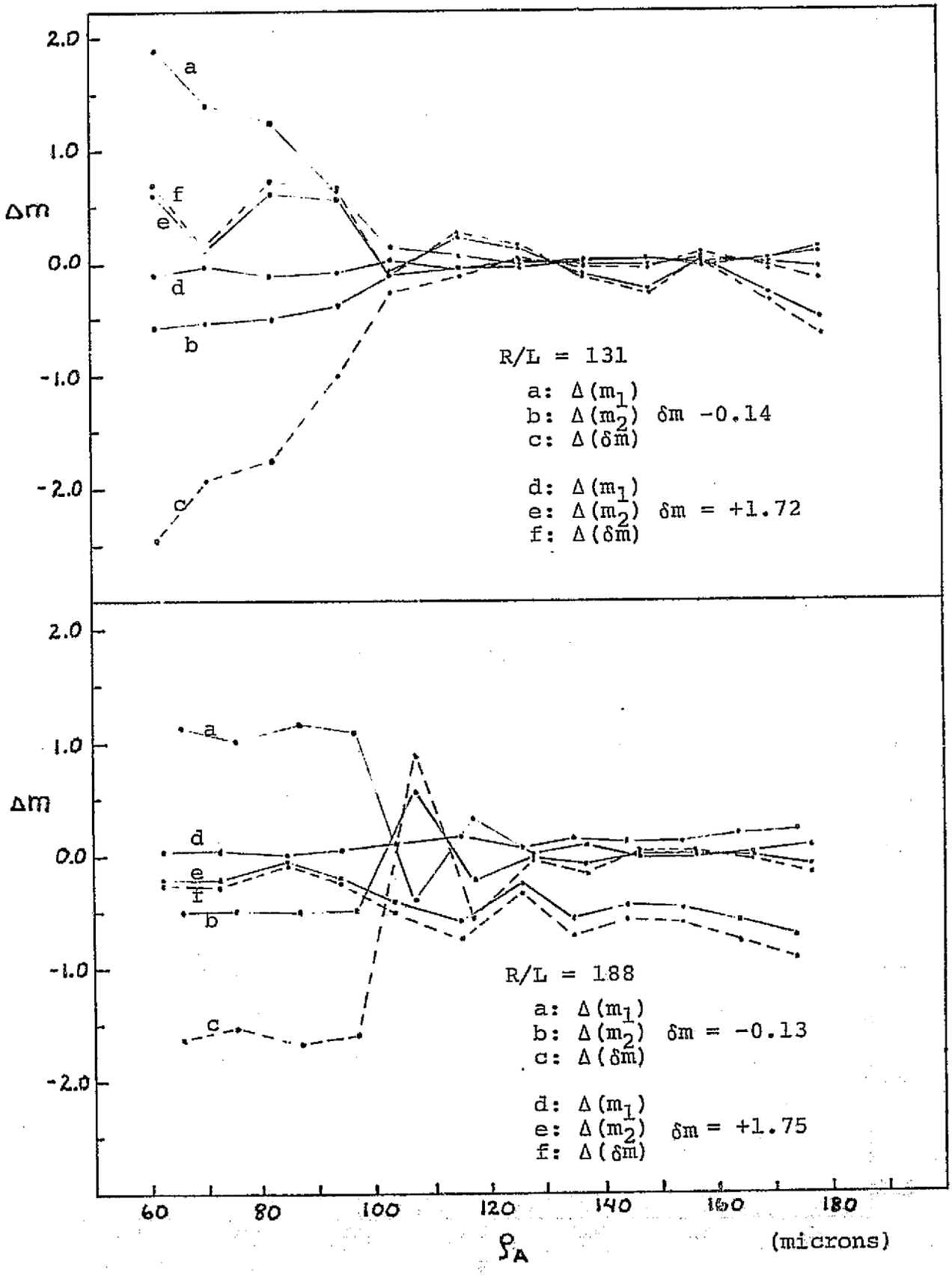

Figure IV.3.8. Errors in Magnitudes as Functions of Separation, δm and Distance from Center of Rotation.

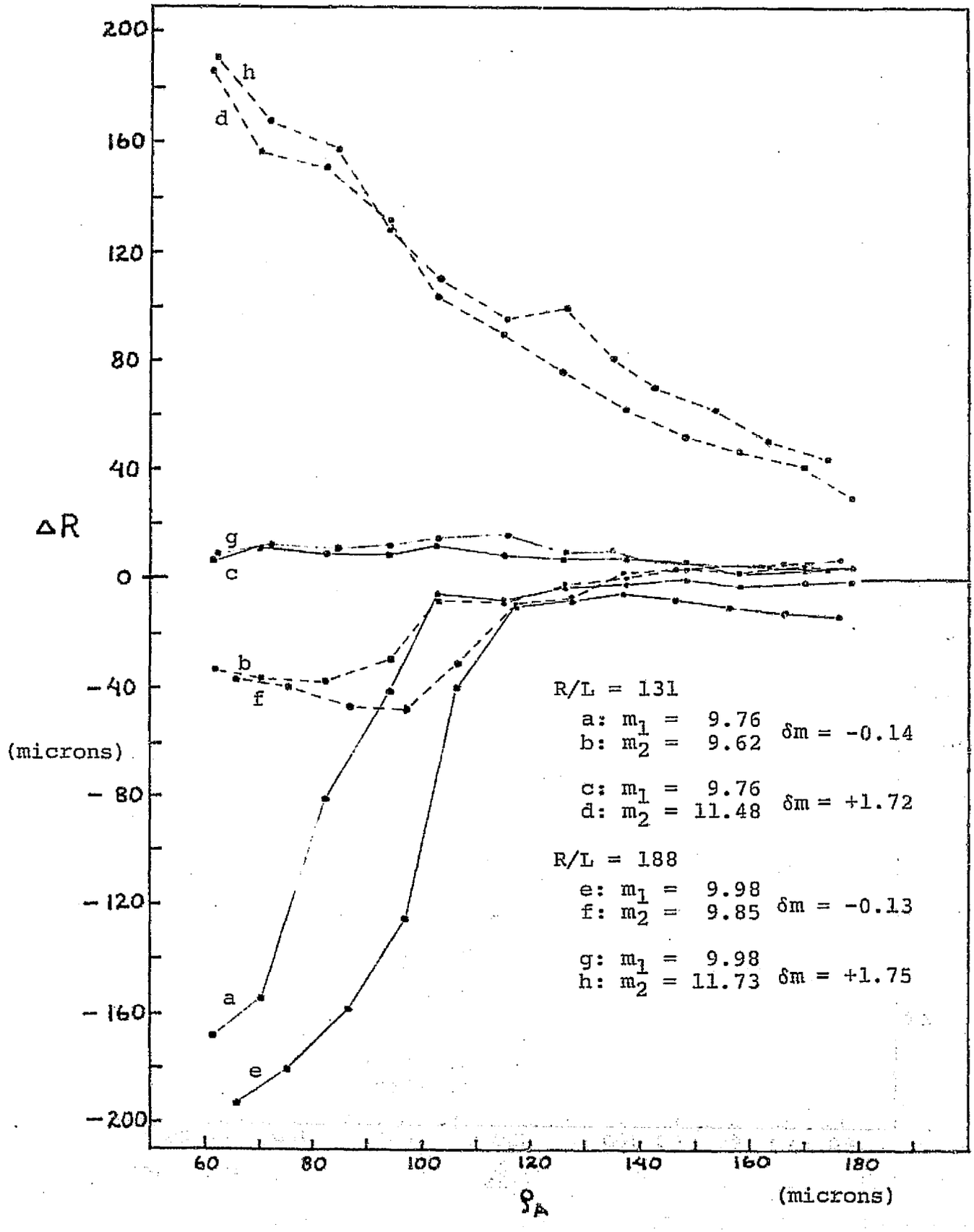

Figure IV.3.9. Errors in R Coordinate Direction as a Function of Separation, δm and Distance from Center of Rotation.

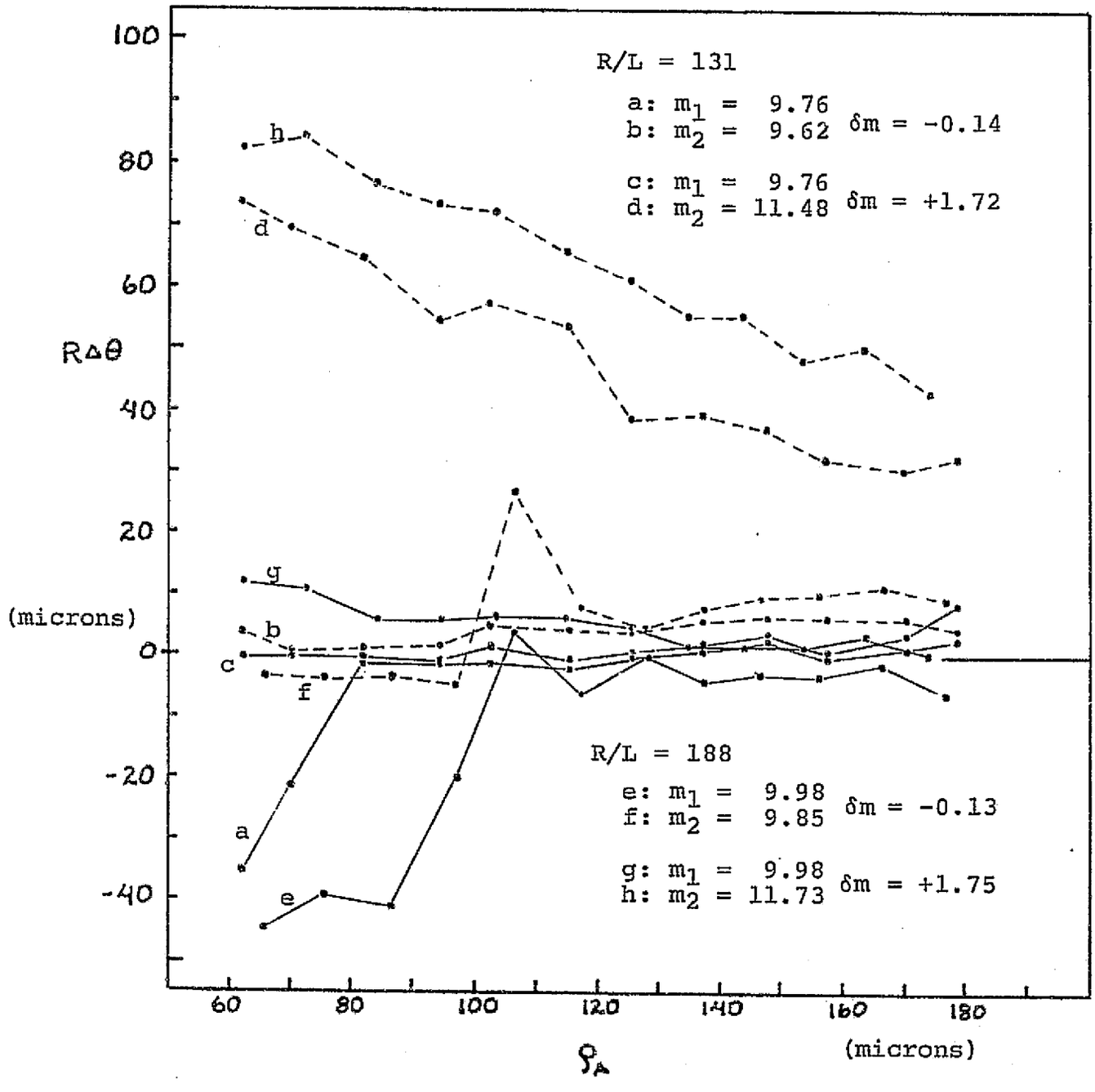

Figure IV.3.10. Errors in θ Coordinate Direction as a Function of Separation, δm and Distance from Center of Rotation.

3.5 $\mathbb{R}(m_1+m_2)$

This series presents the results of observing binaries with primary components of magnitudes 12.0 and 13.1 with secondaries producing δm values of -0.3 and 0.9. ("Primary" refers to the stationary component). These results are shown in Figures IV.3.11 through IV. 3.14. The errors in ρ and P.A. behave similarly to brighter binaries although the position angle determinations appear to be better in general. The errors in the faintest pair with the largest δm overshoot at the largest separation and become negative for both separation and absolute radial position.

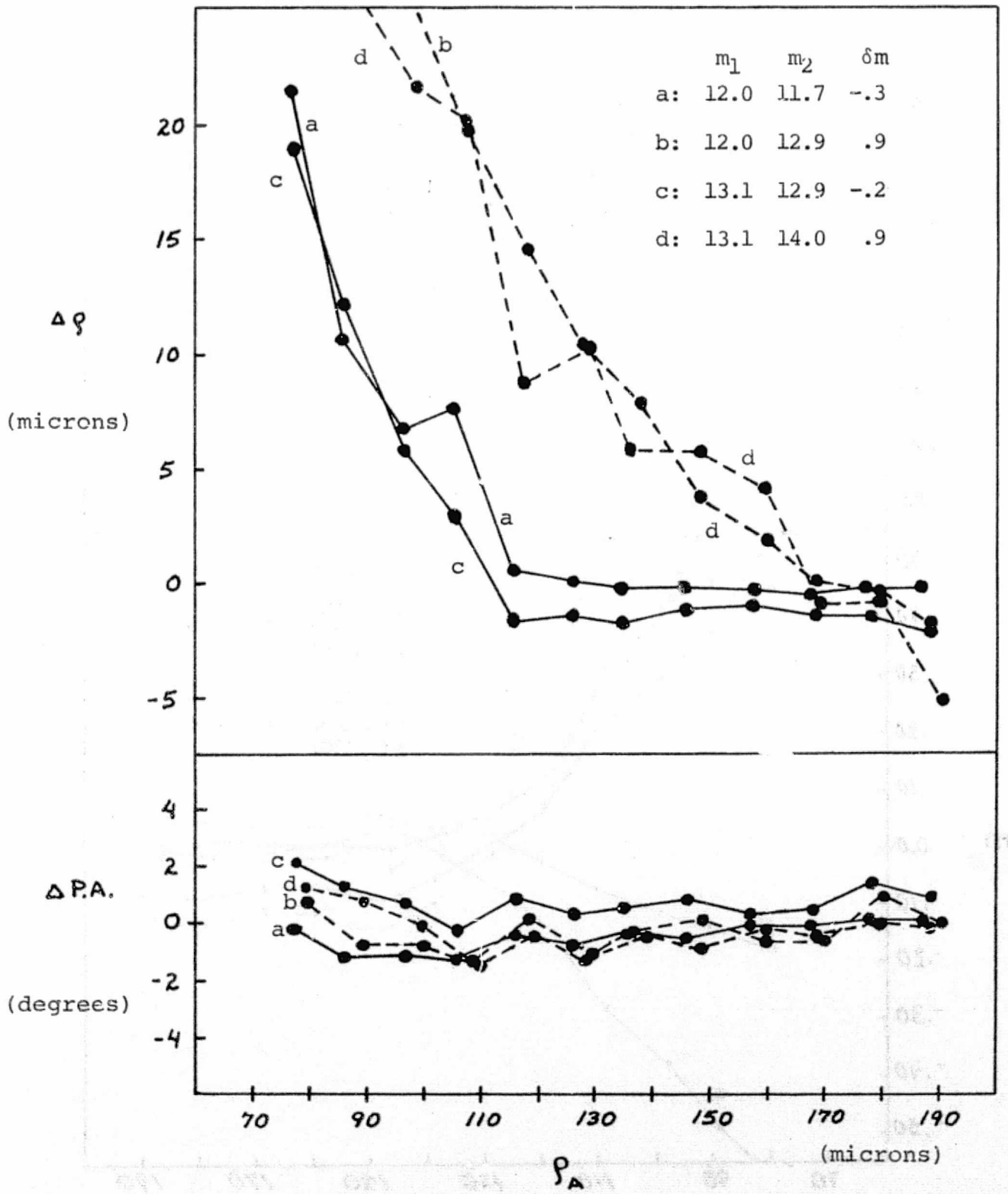

Figure IV.3.11. Errors in (ρ,P.A.) as Functions of Separation, δm and Brightness of Primary. ($\overline{R/L} \simeq 38$, $\overline{\theta} \simeq 51\overset{\circ}{.}6$)

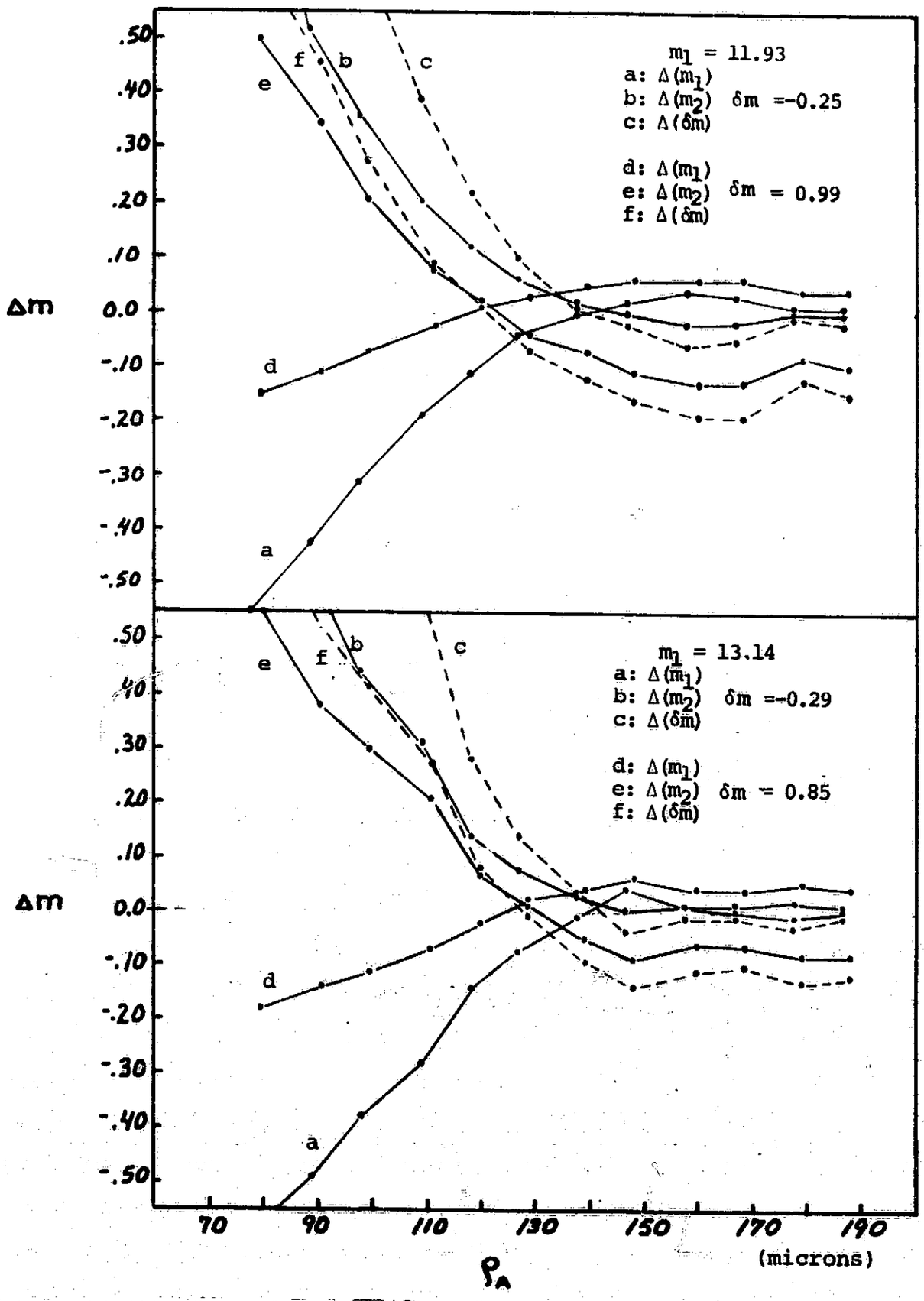

Figure IV.3.12. Errors in Magnitudes as Functions of Separation, δm and Brightness of Primary. ($\overline{R/L} \approx 38$, $\bar{\theta} \approx 51\overset{\circ}{.}6$)

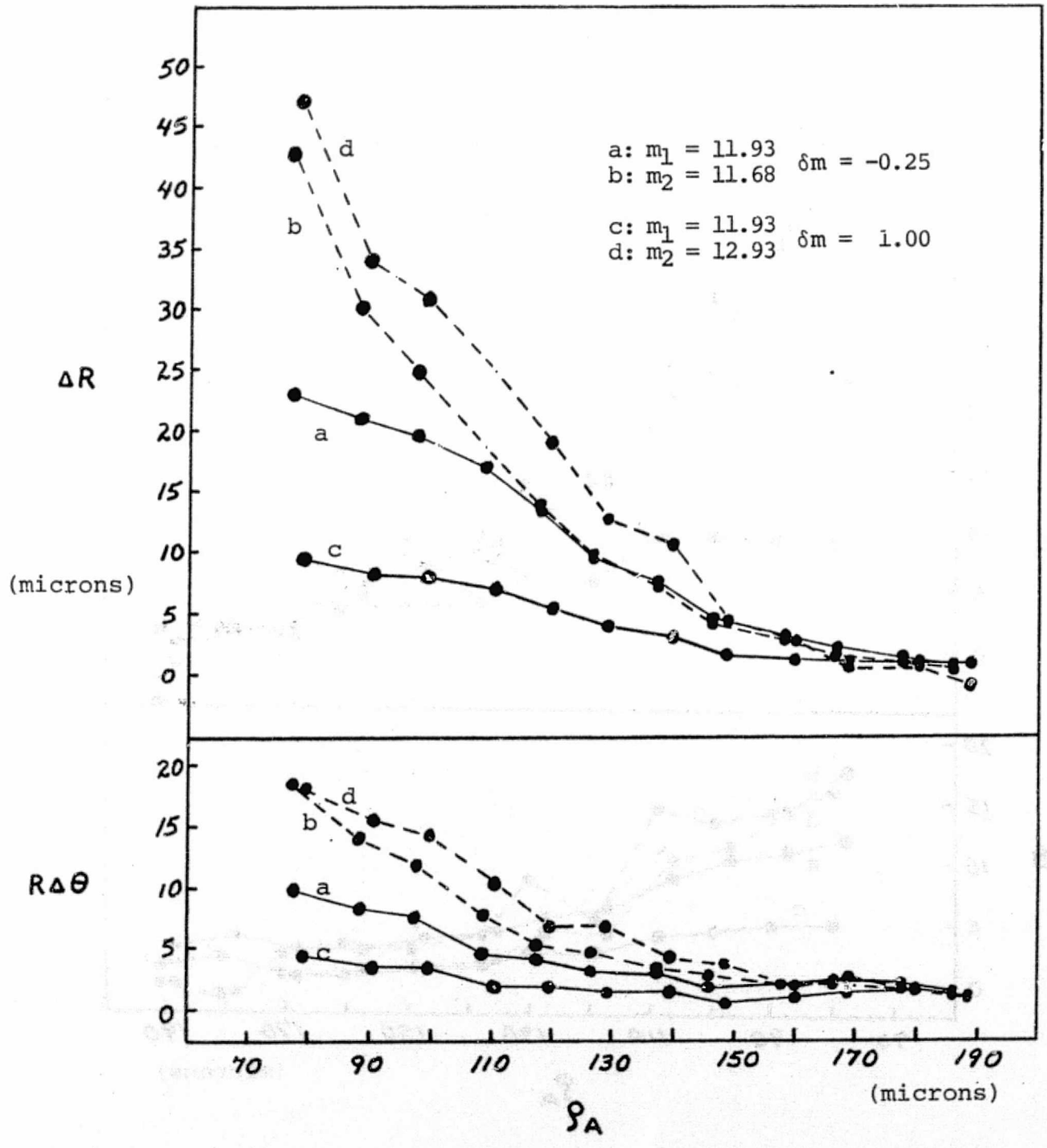

Figure IV.3.13. Errors in (R,θ) Coordinate Directions as Functions of Separation, δm and Brightness of Primary. ($\overline{R/L} \simeq 38$, $\overline{\theta} \simeq 51.^{\circ}6$)

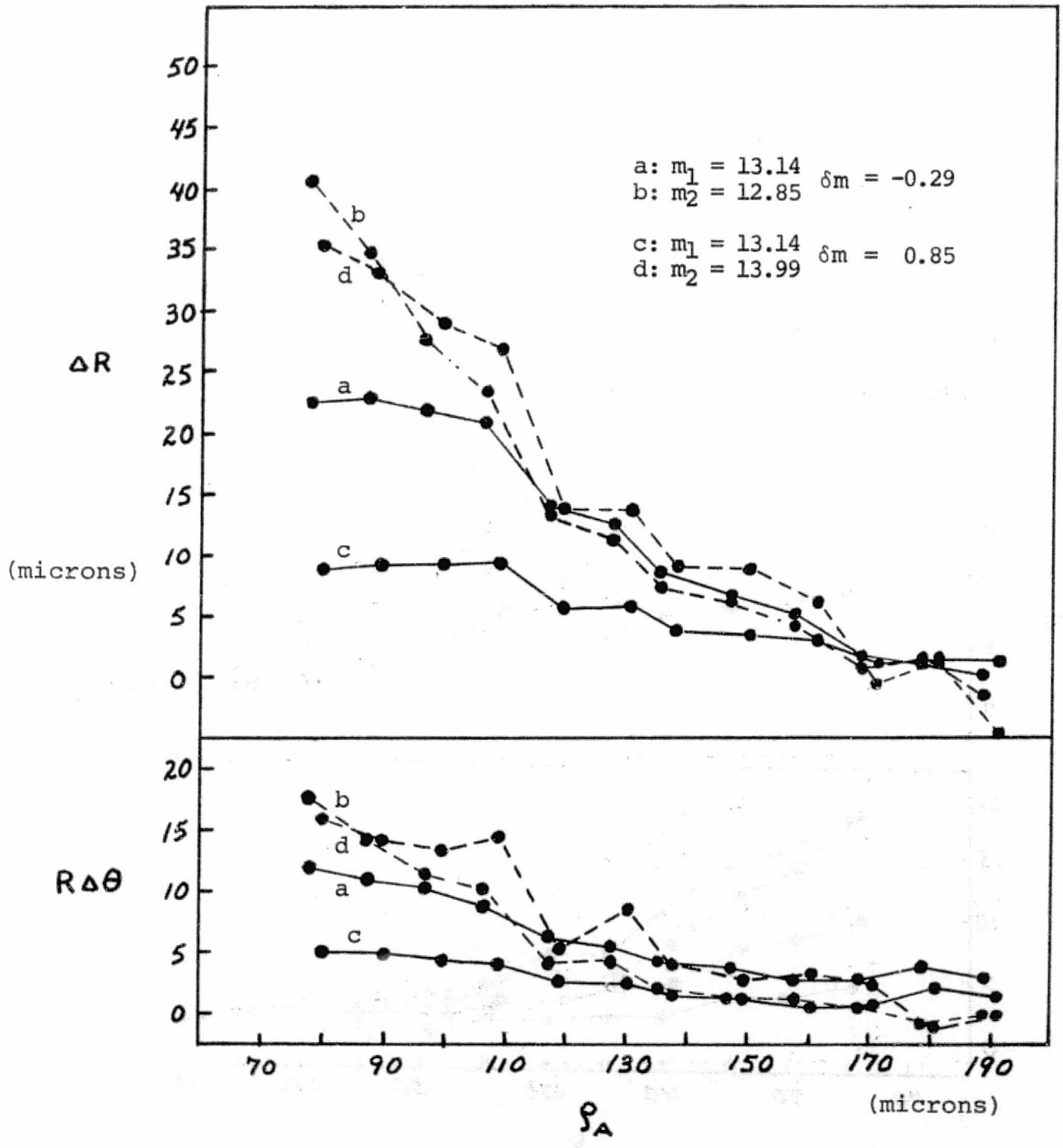

Figure IV.3.14. Errors in (R,θ) Coordinate Directions as Functions of Separation, δm and Brightness of Primary. ($\overline{R/L} \simeq 38$, $\overline{\theta} \simeq 51\overset{\circ}{.}6$)

3.6 $\mathbb{R}(N_{chan})$

Figures IV. 3.15 through IV. 3.18. present results obtained using record lengths other than 480 channels. Three values of N_{chan} were used; 960, 192 and 96 channels. Observations made using 48 channels refused to converge to binary solutions. Each value of N_{chan} has two sets of data corresponding to two values of δm as shown on the diagrams. The results are generally as might be expected. One curious aspect is that the errors in separation for the series N_{chan}= 192, δm=-0.13 slowly diverge positively after having been small negative values absolutely smaller than the errors for N_{chan}=960, δm=-0.21. The errors in magnitudes as shown in Figure IV. 3.16. are plotted as one component versus the other. Generally, the value of ρ_A is increasing as the two errors approach zero.

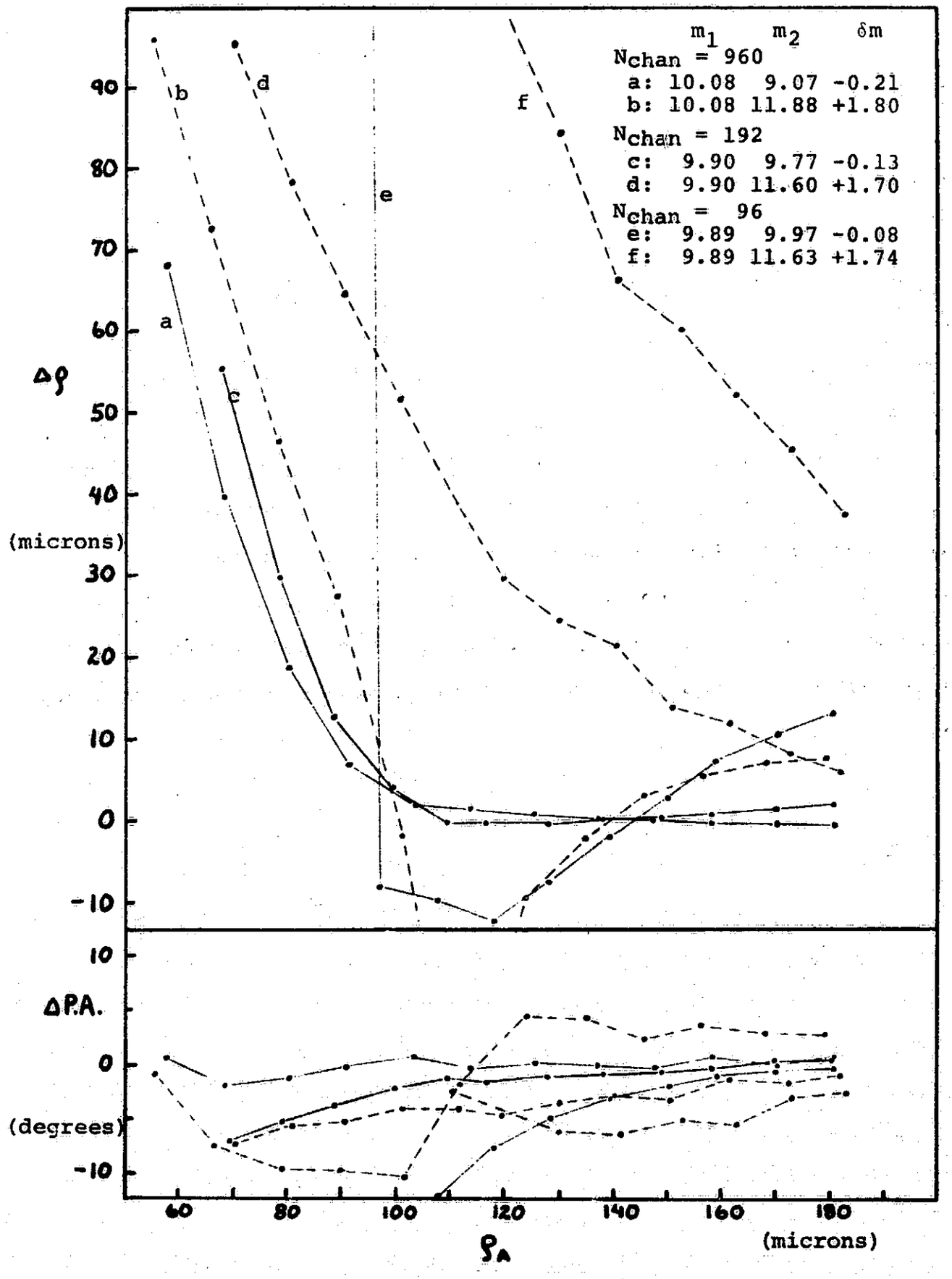

Figure IV.3.15. Errors in (ρ,P.A.) as Functions of Separation, δm and Record Length (N_{chan})
($\overline{R/L} \approx 36$, $\bar{\theta} \approx 51^{0}.8$)

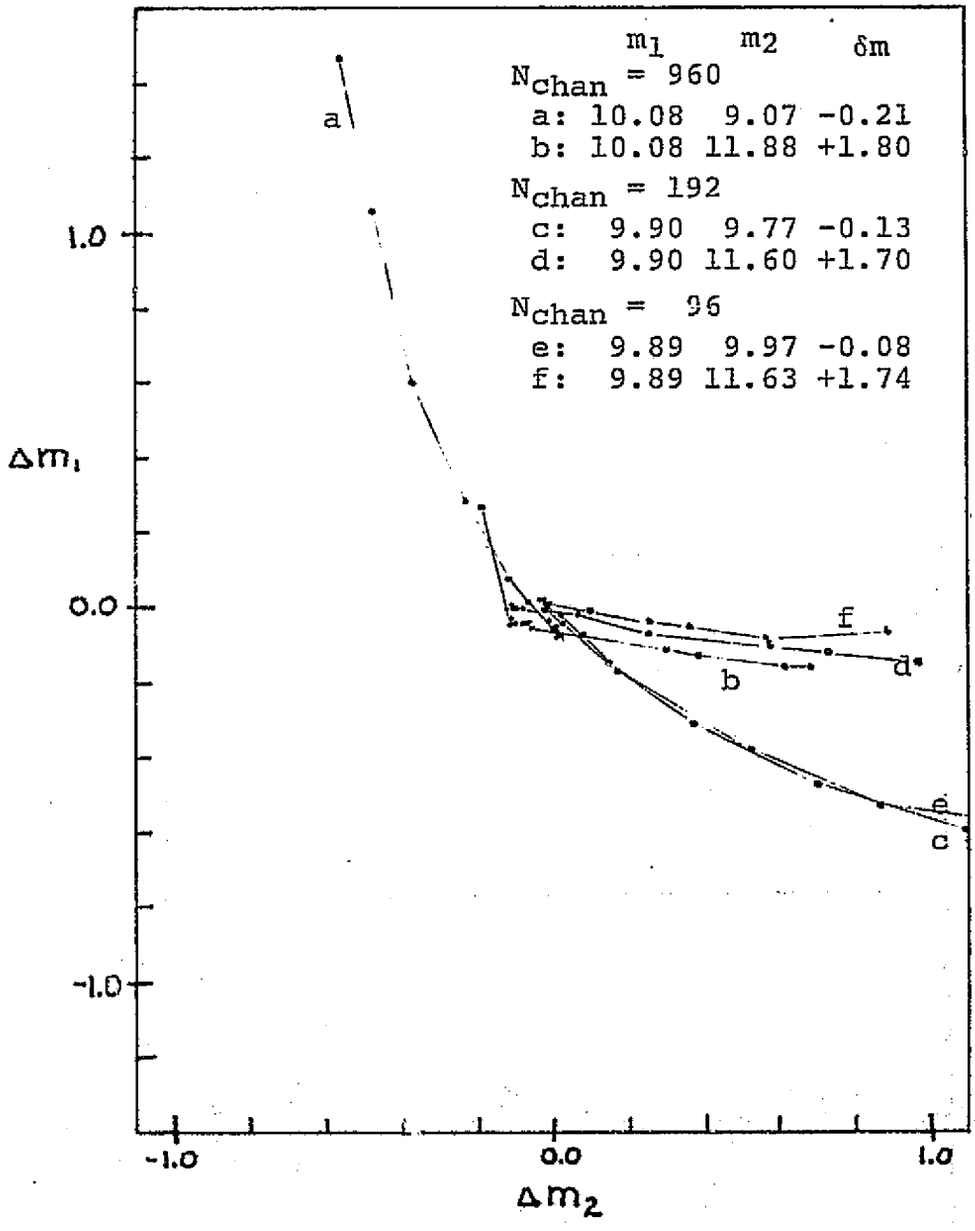

Figure IV.3.16. Errors in Magnitudes as Functions of Separation, δm and Record Length (N_{chan})
($\overline{R/L} \simeq 36$, $\overline{\theta} \simeq 51\overset{\circ}{.}8$)

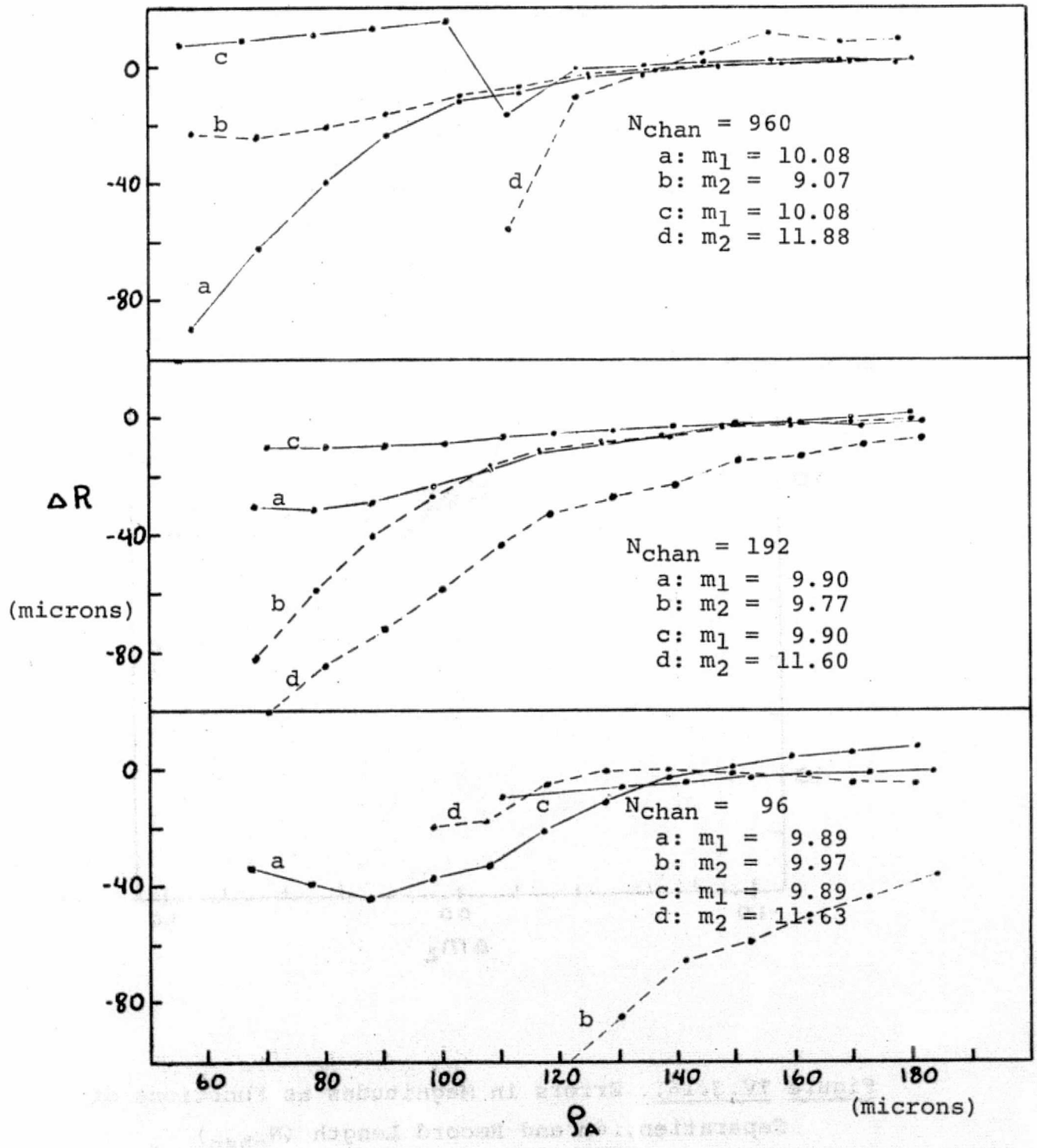

Figure IV.3.17. Error in R Coordinate Direction as a Function of Separation, δm and Record Length. (N_{chan}) ($\overline{R/L} \simeq 36$, $\bar{\theta} \simeq 51.^{\circ}8$)

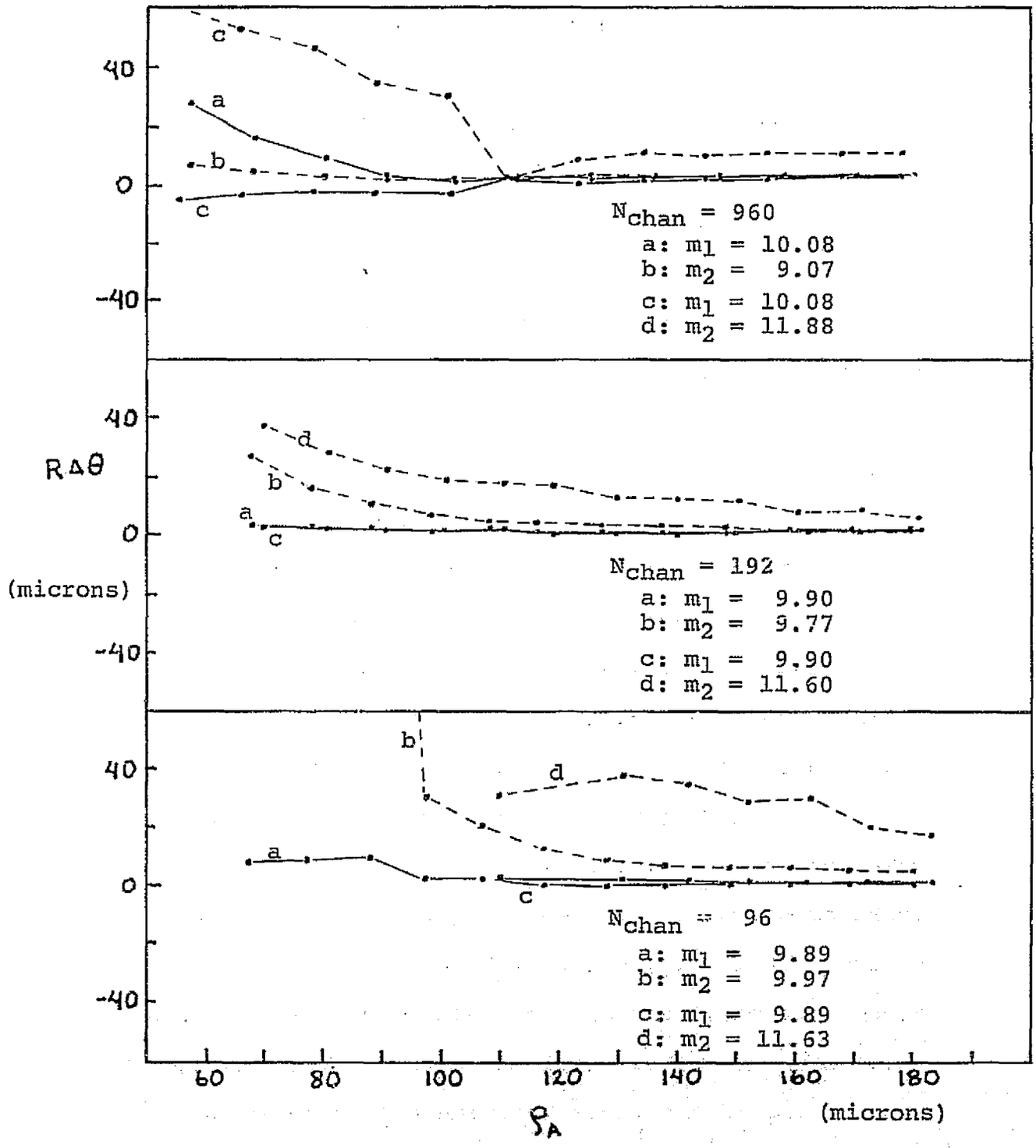

Figure IV.3.18. Error in θ Coordinate Direction as a Function of Separation, δm and Record Length. (N_{chan}) ($\overline{R/L} \approx 36$, $\overline{\theta} \approx 51.^{\circ}8$)

3.7 ℝ(Distribution of background stars)

Results up to this point have been for at most a pair of stars. To be versatile, the AMAS must be able to observe many stars simultaneously. Indeed, this is in principle one of its strong points - it provides two dimensional positional information for a field of stars. Rosenberg (1972) has shown that the mathematical technique is capable of reducing up to six computer generated star signals.

The present test considers a field of ten stars - a not unreasonable number for a typical parallax field. Individual signals were first obtained for eight widely separated stars and one binary in the field center with a separation of 125 microns and δm of 1.4 magnitudes. All the observations were obtained using 480 channels to record 180° of ruling rotation. The reduced solutions for each individual star show a range of magnitudes from 9.99 to 12.62 and a range of R/L from 14.6 to 101.0 (i.e., R=1.8 to 12.8mm). The combined signal for all ten stars is shown in Figure IV.3.19

The individual solutions were then added in various combinations to investigate the effects of additionally observed stars upon the resolution accuracy of the central binary. Obviously, one must have prior knowledge of the number and positions of the field stars before approaching a solution to such a complicated wave form. Figure IV.3.20 shows a map of the field covering a 16 x 16 mm area of the focal plane. A cross marks the location of ruling rotation center and an arrow shows the direction of $\theta = 0^{\circ}.0$. In addition,

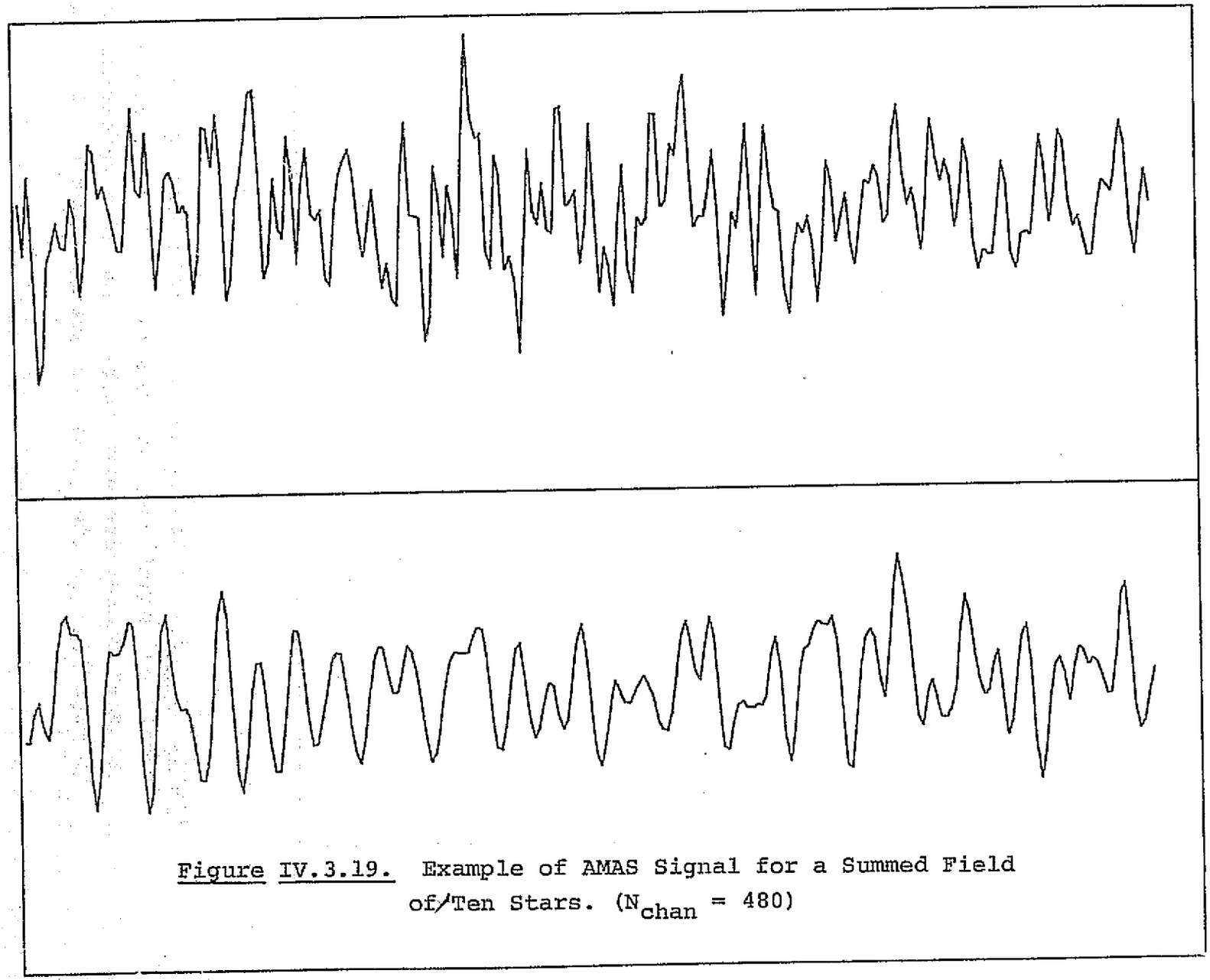

Figure IV.3.19. Example of AMAS Signal for a Summed Field of Ten Stars. (N_{chan} = 480)

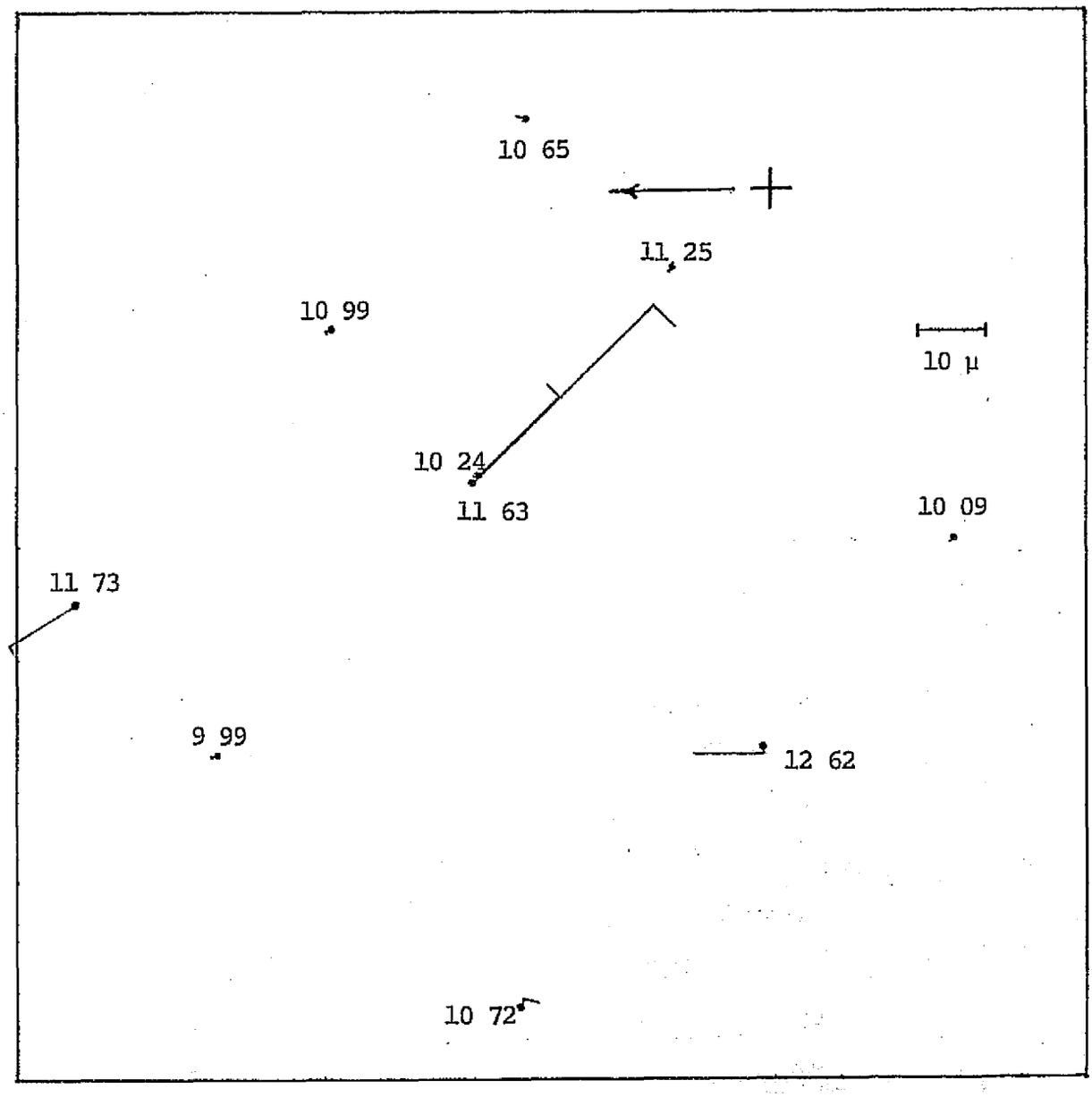

Figure IV.3.20. Chart of 16x16 mm Field Showing Actual Star Positions, Magnitudes and Exaggerated Error Components in (R,θ) Coordinate Directions. (The 10 μ reference mark is magnified to 100 times the actual scale of this field)

lines of lengths scaled to the exaggerated 10 micron mark show the displacement errors when all 10 stars are reduced simultaneously.

Table IV.1. summarizes the standard data for the field obtained from individual solutions. This data furnishes the initial estimates and reference values for the combined solutions. Table IV.2. indicates the additional fields generated using fewer than 10 stars.

Table IV.1. Standard Values for Field Members.

Star Number	R(mm)	θ(degrees)	m
1	5.9321	117.806	10.09
2	8.3917	88.816	12.62
3	12.8261	72.803	10.72
4	1.8502	38.628	11.25
5	6.0984	44.395	10.24
6	6.2235	44.482	11.63
7	11.8431	45.603	9.99
8	3.8052	-16.142	10.65
9	6.8913	17.444	10.99
10	12.1576	30.718	11.73

The results for the 10 cases constructed from the 10 candidate stars are shown in Figures IV. 3.21. a-d. The errors in the (R,θ) co-ordinate directions and the error in magnitude are plotted as a function of the actual magnitude of the star. The errors are derived from the values obtained for the corresponding star in its individual solution. Figure IV. 3.22. shows the effects of additional background stars on

the solution to the central binary. The initial errors inherent in the binary solution are unaffected with three additional stars but begin to degrade with further addition of stars. The error in P.A. remains essentially unchanged.

Table IV.2. Combinations of Field Stars Reduced Together.

Case Number	Component Star Numbers	Total
1	5,6	2
2	5,6,8	3
3	5,6,1	3
4	5,6,10	3
5	5,6,2	3
6	5,6,3,8	4
7	5,6,3,8,10	5
8	5,6,3,8,10,1,9	7
9	5,6,3,8,10,1,9,2,4	9
10	All	10

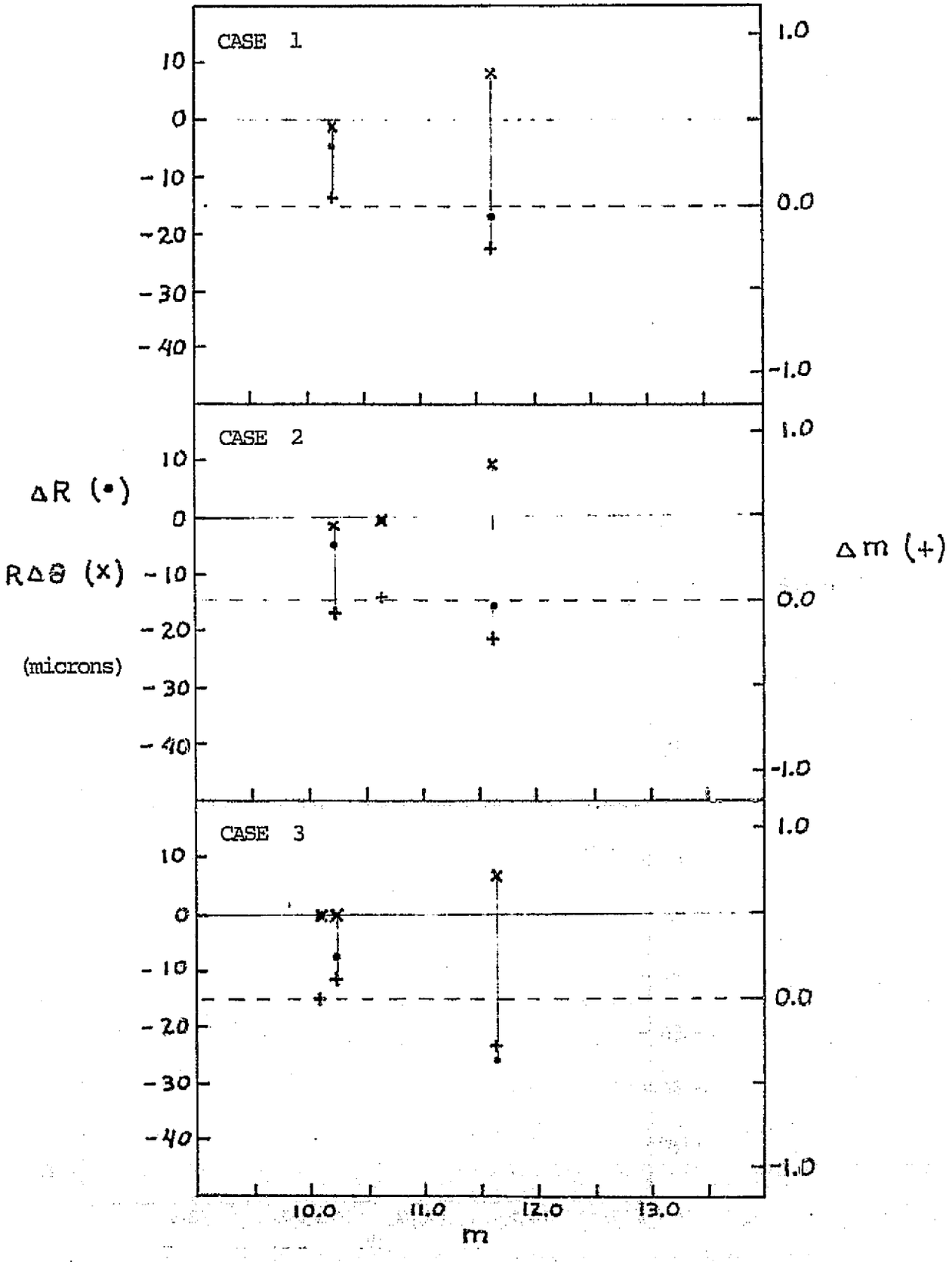

Figure IV.3.21.(a). Errors in Position and Magnitude as Functions of Number and Apparent Magnitudes of Field Stars for Cases as Described in Table IV.2.

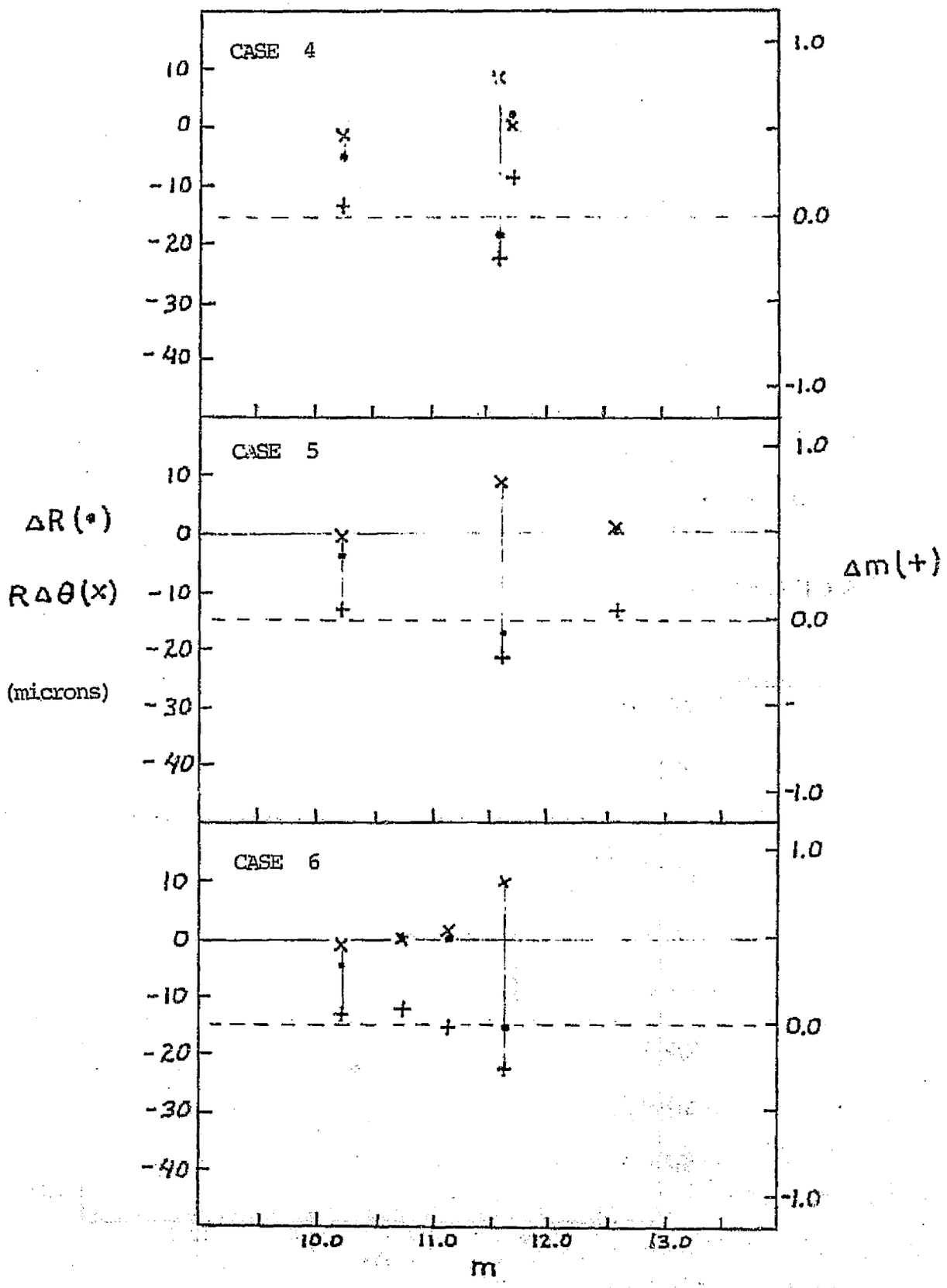

Figure IV.3.21.(b). Errors in Position and Magnitude as Functions of Number and Apparent Magnitudes of Field Stars for Cases as Described in Table IV.2.

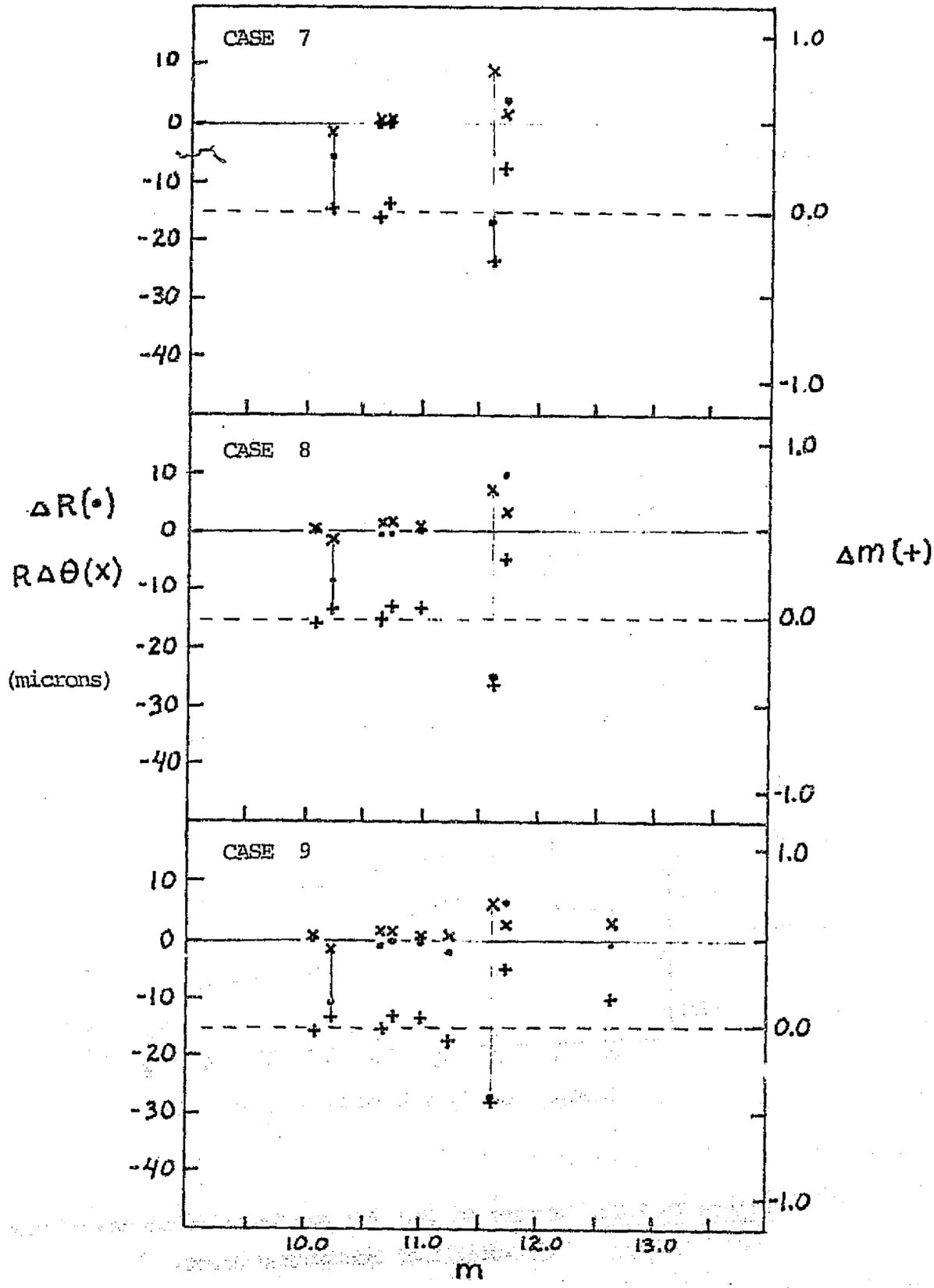

Figure IV.3.21.(c). Errors in Position and Magnitude as Functions of Number and Apparent Magnitudes of Field Stars for Cases as Described in Table IV.2.

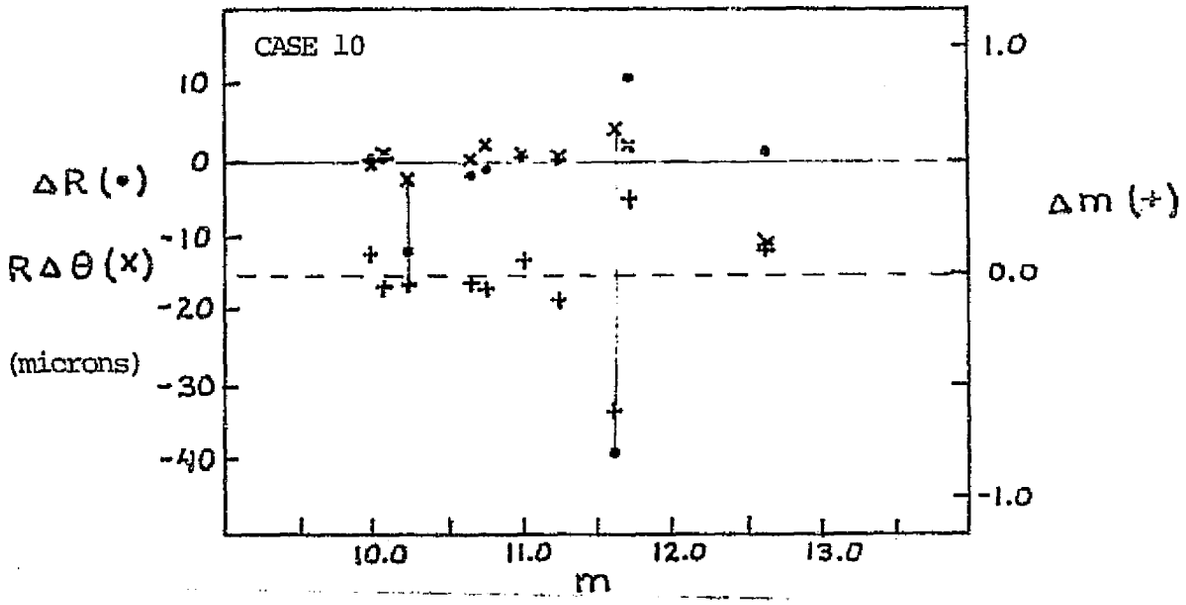

Figure IV.3.21.(d). Errors in Position and Magnitude as Functions of Number and Apparent Magnitudes of Field Stars for Cases as Described in Table IV.2.

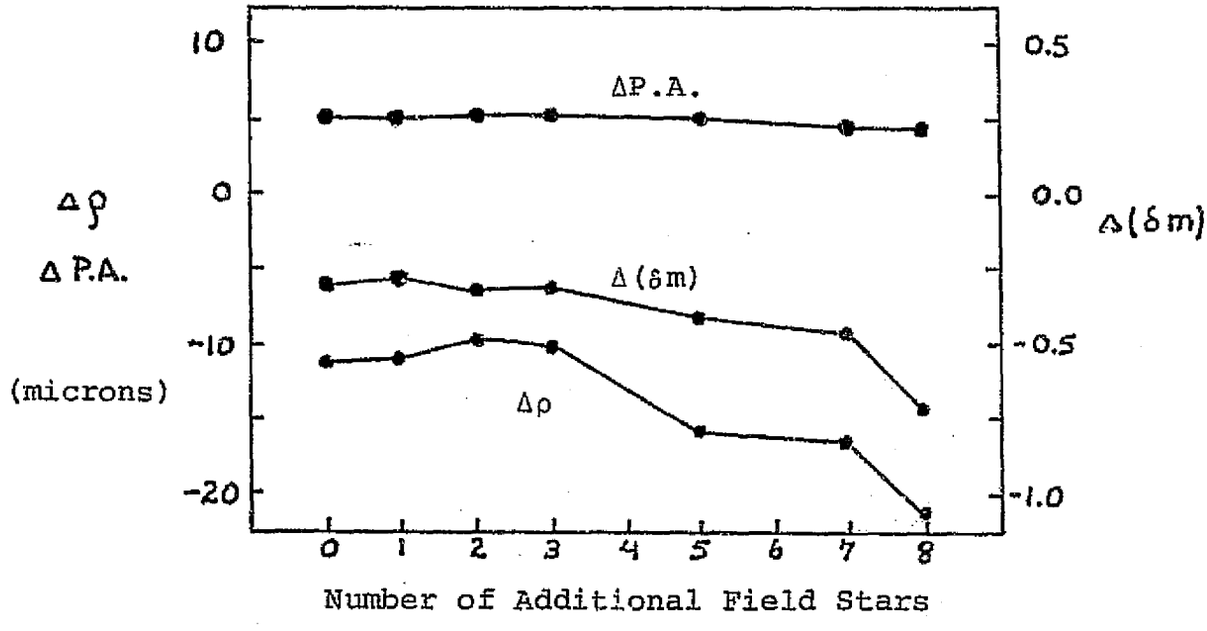

Figure IV.3.22. Errors in (ρ,P.A.) and δm as Functions of Number of Additional Background Stars.

V. Discussion of the Results

A. Precision of the AMAS

The results indicate the AMAS's precision, as defined in terms of repeatability of measurement, for single stars can be conservatively put at 1.5 microns in each coordinate under certain limiting conditions. Beyond values of R/L≈200 the precision tends to decrease, undoubtedly due to non-constant ruling rotation rate. An upper limit of apparent magnitude may be put at 12.5 for the current prototype AMAS. However, it is perhaps more proper to express this limit in terms of a signal to noise ratio of approximately 3.8 since the limiting magnitude may be extended by depressing the noise via photomultiplier cooling or increased integration times.

B. Accuracy of the AMAS

The AMAS has been found to accurately duplicate a calibrated displacement of 10.3 $\pm$ 1.2 microns over a similar range of parameters which limits the above described precision. This displacement is repeatably observed to well within one micron, indicating the AMAS is free of any serious systematic effects in position in the relative sense. This does not rule out any large scale systematic errors that might be encountered over large relative displacements, although the mathematical and mechanical simplicity of the AMAS as well as the results obtained for star fields lead one to doubt the existence of such errors.

C. Resolving Capability of the AMAS

The AMAS is found able to resolve binary star images with separations of about 50 microns, but with a large systematic error in separation. The trend to accurate resolution is found to follow a characteristic form over a variety of parameters. For a pair with $\delta m \sim 0$, accurate resolution occurs at a separation of 120 microns. Smaller separations are systematically increased. Position angle determinations accurate to 1° are also made at this separation with evidence for such accuracy at even smaller separations. Thus, for a $\delta m \sim 0$ the AMAS resolves to one micron in separation and one degree in position angle at a separation of 120 microns. For $1 \leq \delta m < 3$ this minimum resolution limit increases to about 175 microns. For $\delta m > 3$, accurate resolution of binary stars may be impractical.

A more meaningful way to look at this may be to translate the linear values to angular ones for a comparison with photographic methods of binary star astrometry. The size of the star image is also a significant factor. Observations of the laboratory images yield a value for σ/L of approximately 0.5. This gives the radius at the point where the intensity falls to 1/e times the central intensity - a radius of approximately 65 microns. However, at this point the intensity is still 37% of the central value. At a radius of $\sqrt{2}\sigma$ the intensity has fallen to 14% of the central intensity. Thus, if this larger value is considered

reasonable, the diameter of the laboratory images becomes $2\sqrt{2}\sigma$ or 180 microns. On the scale of the 40-inch astrometric reflector at Fan Mountain (15.0 arsec.mm^{-1}) this diameter corresponds to 2".7 and the value of accurately determined minimal value of separation corresponds to 1".8. Thus, star images are accurately resolved even when they significantly overlap as shown below in Figure V.1.

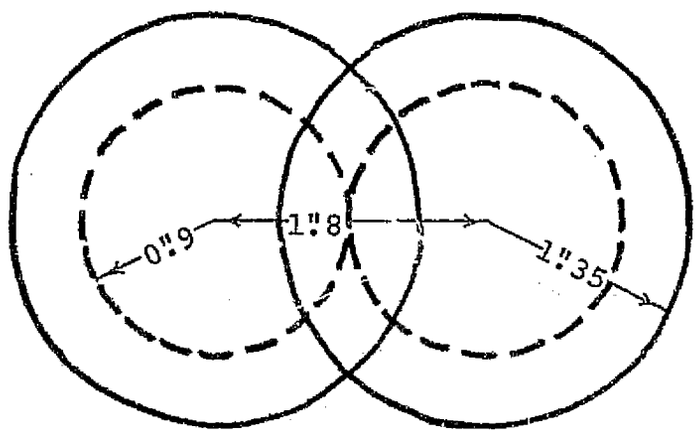

Figure V.1. Configuration of Minimum Accurate Resolution of Binary with $\delta m \sim 0$ and with Diameters Defined as 120 μ (1".8) or 180 μ (2".7).

It is appropriate to compare this result with that achieved with the photographic plate - the chief competitor of the AMAS for which well determined performance parameters exist. Van de Kamp (1967) states that for well blackened star images of about 2".0 diameter, the minimum accurately determined separation is about 2".0. For a plate with forty to fifty exposures, the probable errors in the separation

components ($\Delta x, \Delta y$) are $\pm$ 0".006 as obtained from the entire set of exposures. This corresponds to an error in separation of $\pm$ 0".006 with an error in position angle of 0°.2. The errors associated with a single measurement are 0".04, 1°.1. Thus, a single photographic determination of (ρ, P.A.) has errors of (0".04, 1°.1) as compared with a single AMAS determination with errors (0".02, < 1°.0). Thus, the prototype AMAS performs on the same level as, and perhaps slightly better than, the photographic plate in combination with a precision measuring machine with regards to the binary star problem. The limiting resolvable separation for non-zero δm increases similarly in both approaches.

D. Performance of the AMAS for Astrometric Star Fields

The results obtained for numerous stars in a field indicate that over a range of nearly two magnitudes the AMAS gives comparable results to observations of each star individually. For fainter stars, the accuracy decreases accordingly. A typical astrometric field for parallax determination contains up to 10 reference stars and one or two π stars. The reference stars are ideally chosen to have a magnitude spread of less than one magnitude centered about 11.0 and the π star's brightness is depressed to this magnitude by means of a rotating sector. Thus, the AMAS in its prototype form will accomodate such a problem.

A better approach than observing the entire field simultaneously would be to replace the usual photomultiplier tube with an image dissector that would allow the AMAS to

"look" at selected areas of the field at any one time. By varying the currents through the yoke about the neck of the tube, only a portion of the photocathode is used to supply the dynode chain with photoelectrons. Thus, if the field is imaged onto the photocathode in a slightly out-of-focus fashion to minimize the effects of non-uniform photocathode, one can electronically limit the effective area of observation to the region immediately surrounding the star. The entire field can be scanned electronically to produce individual signals for each field star without faint stars being washed out by brighter neighbors. The background light of the sky would then also be drastically reduced. The photometric accuracy of this technique would be limited by the degree of uniformity of the photocathode and first dynode.

VI. Effects of Non-constant Ruling Rotation

The signal generated by a single source with the D.C. term removed is given by

$$I_j = A_k \operatorname{Cos}\left[\frac{\pi R_k}{L}\operatorname{Cos}\ (\omega t_j + \theta k)\right] ,$$

where ω is a motor parameter assumed constant and t_j arises from the multiscaling so that $(t_{j+1} - t_j)$ is also assumed constant. For simplicity one may write

$$\theta_j \equiv \omega t_j$$

since channel number may equivalently be considered as ruling position angle.

In the reduction scheme, θ_j is assumed to be free of error as in the case of an ideal motor. That this is obviously incorrect may be seen in the variation in ruling rotation period measured by means of the pulses from the optical trigger. In effect, any error in θ_j must be treated in the reduction as if it arose from variations in θ_k. That is, any real error in θ_j is equivalently treatable as an error in θ_k with θ_j being error free.

Thus, all that needs to be done to evaluate the effects of motor speed variation on θ_k is to measure those variations. Since successive sweeps are synchronized at $\theta_j=0$, the error in θ_j is simply, in the first approximation, a fraction of the error in θ_N if one makes the further assumption that within a single rotation ω is constant. Thus, the speed variations are in successive sweeps so that θ_j is scaled by some amount from sweep to sweep.

Figure VI.1. shows the trend in rotation period of the Ronchi ruling as a function of the elapsed motor run time for the original motor, the new motor and the period measured at the motor shaft itself under the normal operating load. The latter curve indicates the degradation introduced by the rubberized belt and variation in bearing friction. These effects are especially serious during the first 30 minutes of operation while the system temperature was increasing. The motor was routinely allowed to run for 60 minutes before any recorded observations were made. The data for Figure VI.1. was obtained by making a series of many observations of ten rotations per observation with periods determined with a digital counter accepting pulses from the optical trigger. The errors associated with single rotations of the ruling and motor are 2.44 and 2.80 milliradians respectively. Note that the accuracy of rotation at the ruling is greater than at the motor shaft verifies the hope that when the prototype was constructed, the rather massive bearings would smooth out variations introduced by the motor.

The error that is translated into the position of a star is then directly proportional to its distance from the center of rotation of the ruling and only affects the θ-coordinate direction. Since information is being accumulated at all ruling position angles and the error in θ_j is presumably zero at $\theta_j=0$, the error in θ_j is just

$$\Delta\theta_j = \frac{j}{N}\sigma_{\theta_j} = \frac{j}{N}(2.44\times10^{-3})$$

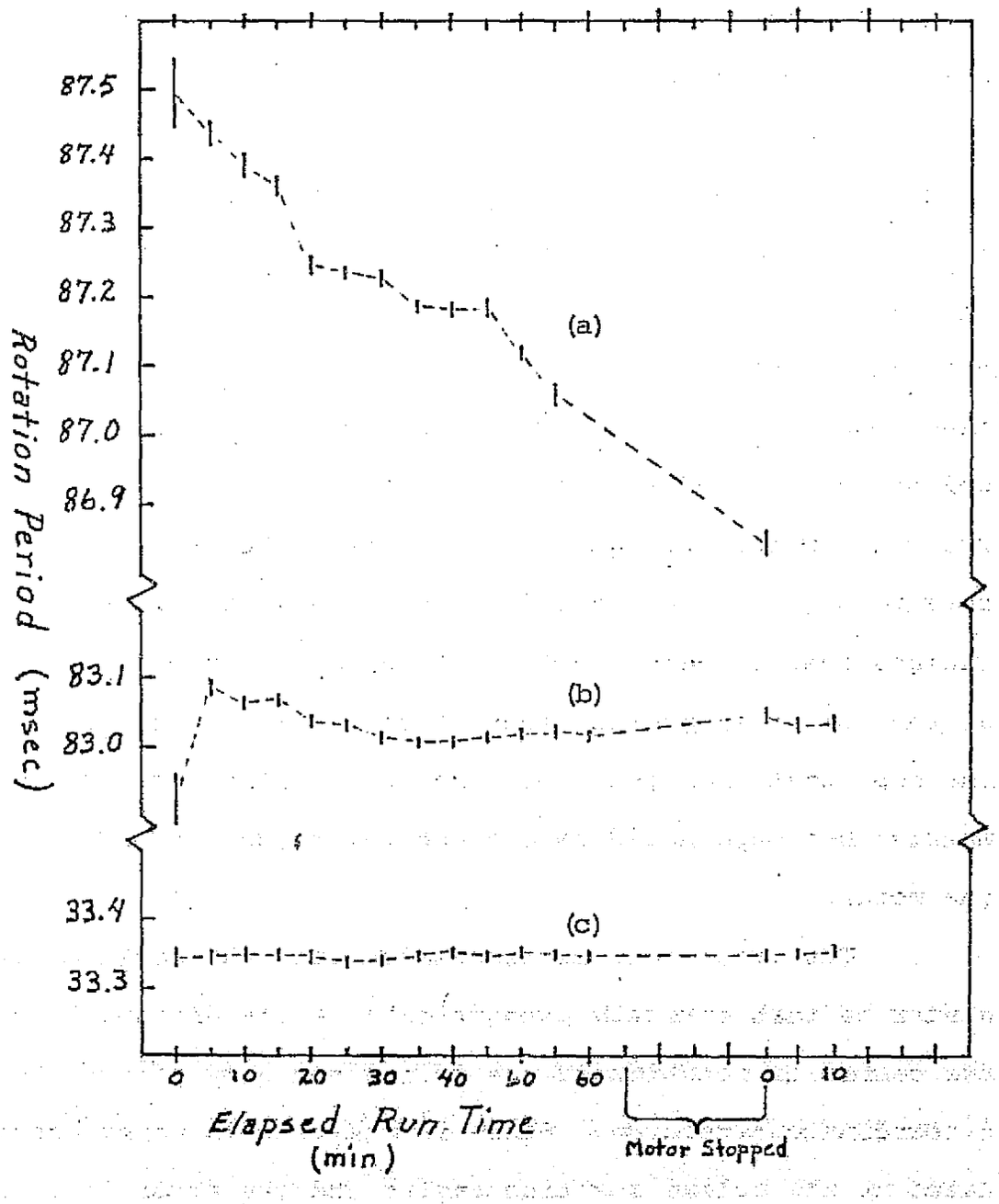

Figure VI.1. Rotation Period Measured at (a) Ruling with Original Motor, (b) Ruling with New Motor and (c) Shaft of New Motor.

where N is the total number of channels. The error that is then associated with θ_k may be taken as

$$\sigma_{\theta k} = \frac{1}{N}\sum_{j=1}^{N} j\sigma_{\theta j} = \frac{\sigma}{N}\theta_j \frac{1}{N}\sum_{j=1}^{N} j$$

$$= \frac{\sigma}{N}\theta_j \bar{j} = \frac{\sigma}{N}\theta_j \frac{(N+1)}{2} \simeq \frac{\sigma}{2}\theta_j \quad .$$

The angular error associated with θ_k produces a linear error in the θ_k direction given by

$$\sigma_{\theta_k} = \frac{\sigma}{2}\theta_j R_k \simeq (1.22\times10^{-3})R_k \quad .$$

For a value of R/L=25 (R=3.175 mm) one sees that $\sigma_{\theta k}$=3.9 microns. The error in the θ_k direction exceeds 10 microns for values of R/L >64.5 (R=8.197 mm).

In order to see the effects of non-constant rotation, T. Strickwerda (1975) has modeled the effect by convolving an elliptical image, whose major axis is in the θ_k direction, with the ruling transmission pattern. The effect is to produce an amplitude modulation envelope with the greatest "pinch" centered on the high frequency component. This is perhaps intuitively to be expected, as the high frequencies are smeared out more than the low frequency component under conditions of non-constant rotation. Also, the amount of light observed when the ruling is at the low frequency orientation is unaffected by variations in $(\sigma/L)_\theta$. Strickwerda finds that the usual exponential damping term becomes

$$e^{-\{\pi/2(\sigma/L)_R\}^2\{\mathrm{Cos}^2(\theta_j+\theta_k) + (\sigma_\theta/\sigma_R)^2\mathrm{Sin}^2(\theta_j+\theta_k)\}} .$$

He has used this expression to produce computer generated AMAS signals which model non-constant rotation. The effect of this amplitude modulation is to produce residuals that are themselves double cosine functions. Figure VI.2(a). shows the residuals for the solution to the signal displayed in Figure I.3.(a). One might attempt a correction based on these residuals by letting them represent a fictitious star whose position is reduced along with the real star. In this particular case, a solution to the residuals by themselves gives rise to a fictitious star removed from the real star by ΔR=152 microns and $R\Delta\theta$=33 microns. The fictitious star also has a negative intensity. When the two are solved together, the real star is shifted by $(\Delta R, R\Delta\theta) = (1.0, 0.1)$ microns. This procedure produced a correction in R and not in θ as might be expected. The r.m.s. of the residuals decreases by about 40%. The new set of residuals is shown in Figure IV.2.(b). They again show the expected double cosine form reduced in amplitude. Presumably the procedure, if valid, could be repeated to further reduce the dispersion in the residuals.

Clearly a better way of eliminating the ill effects of non-constant rotation is to use an optically encoded motor with a servo speed control and the ruling mounted directly on the motor shaft. The maximum allowed error accumulated after one rotation as a function cf the desired maximum error in the θ_k direction is given by

$$\sigma_{\theta j} = 2\sigma_{\theta k}/R_k$$

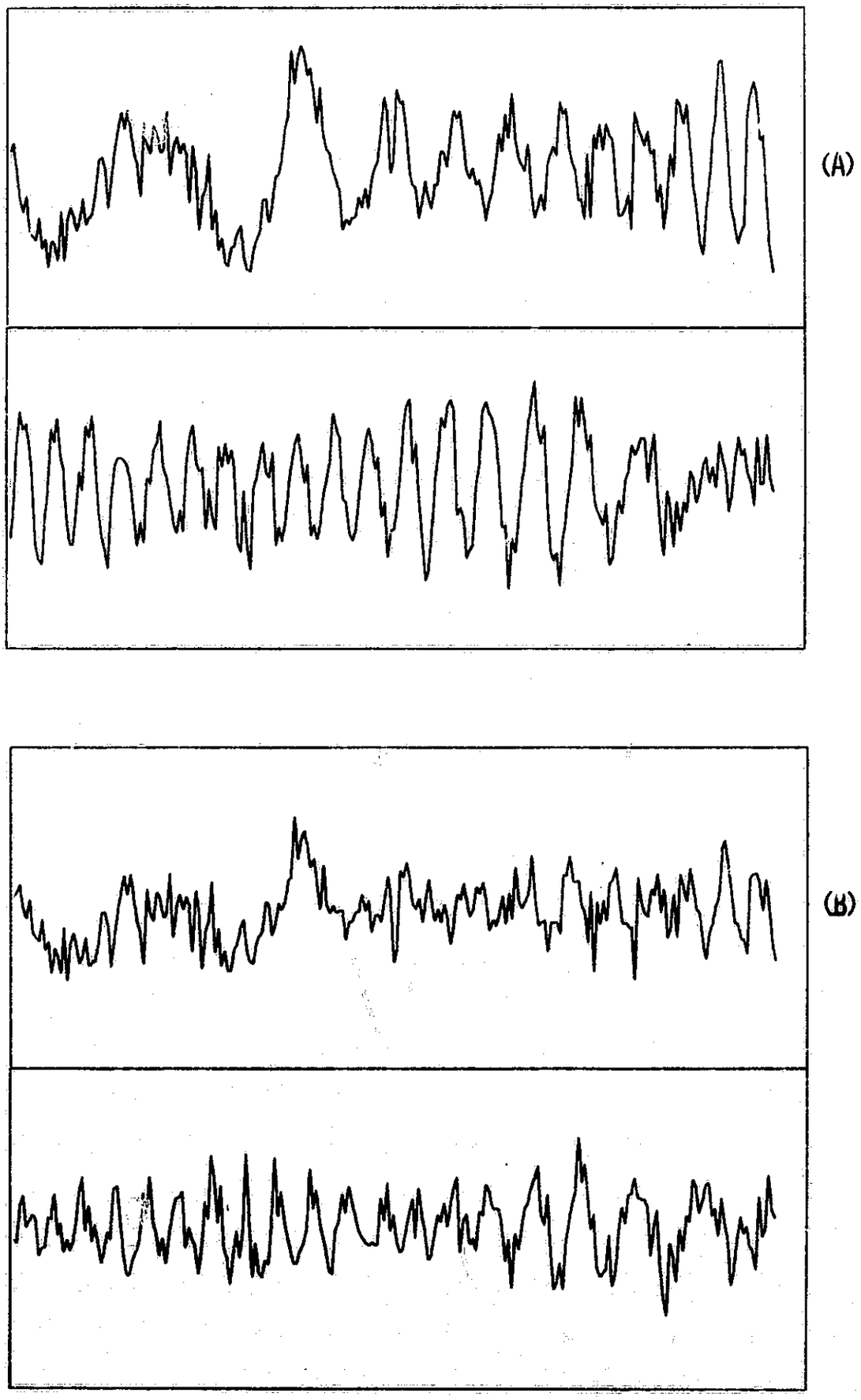

Figure VI.2. (a) Residuals to Solution of Signal Shown in Fig.I.3.(a). (b) Residuals Remaining After Fictitious Star has been Introduced in Attempt to Correct for Signal in (a). (The vertical scale is here approximately 1/5 that of Fig.I.3.)

For a 40-inch telescope with $\sigma_{\theta k} \sim$ 0.5 micron and $R_k \sim$ 50 mm, $\sigma_{\theta j} \sim$20 microradian. For an LST with $\sigma_{\theta k} \sim$ 0".002 $\sim$0.7μ (at F/24) and $R_k \sim$50 mm, $\sigma_{\theta j} \sim$ 28 microradians. These values of $\sigma_{\theta j}$ represent an increase in accuracy of nearly 100 times the rotational accuracy of the prototype AMAS.

VII. Effect of Non-centered Ruling

Another instrumentally induced error arises from not positioning the center of rotation exactly between two lines (either transparent or opaque). The geometry for such a situation is shown in Figure VII.1. which considers the ruling difining the frame of rest and the star image orbiting about the actual center of rotation.

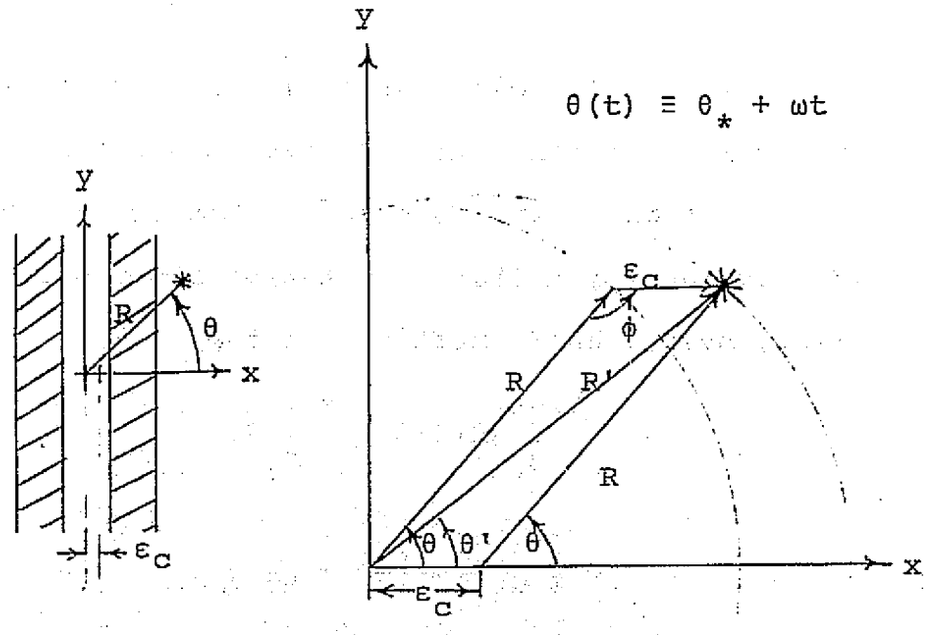

Figure VII.1. Geometry of a Non-centered Ruling

Since

$$R'^2 = R^2 + \varepsilon_c^2 - 2R\varepsilon_c \cos\phi \qquad \text{where } \phi = \pi - \theta$$

$$= R^2 + \varepsilon_c^2 + 2R\varepsilon_c \cos\theta \qquad \cos\phi = \cos(\pi-\theta) = -\cos\theta$$

the error in R is given by

$$\Delta R \equiv R' - R = (R^2 + \varepsilon_c^2 + 2R\varepsilon_c^2 \mathrm{Cos}\theta)^{\frac{1}{2}} - R \ . \quad (7\text{-}1)$$

Also, since

$$\mathrm{Sin}\Delta\theta = \frac{\varepsilon_c}{R'}\mathrm{Sin}\phi = \frac{\varepsilon_c}{R'}\mathrm{Sin}\theta$$

so that

$$\Delta\theta = \mathrm{Sin}^{-1}\left(\frac{\varepsilon_c}{R'}\mathrm{Sin}\theta\right) \ ,$$

where $\Delta\theta \equiv \theta - \theta' \ .$ (7-2)

The displacement arising from decentering is only in the x direction. The cumulative error from this situation is a function of the location of the triggering point θ_0, if only the first 180^0 of rotation are used. The cumulative error, over a half rotation, is then

$$\delta R \equiv \int_{\theta_0}^{\theta_0+\pi} \Delta R(\theta)\,d\theta \ / \int_{\theta_0}^{\theta_0+\pi} d\theta$$

$$= \frac{1}{\pi}\int_{\theta_0}^{\theta_0+\pi} \Delta R(\theta)\,d\theta \ , \quad (7\text{-}3)$$

and similarly

$$\delta\theta = \frac{1}{\pi}\int_{\theta_0}^{\theta_0+\pi} \Delta\theta(\theta)\,d\theta \quad (7\text{-}4)$$

The above equations in their discrete forms are

$$\delta R \simeq \frac{1}{N}\sum_{j=1}^{N} \Delta R(\theta_j) \quad (7\text{-}5)$$

and

$$\delta\theta \simeq \frac{1}{N}\sum_{j=1}^{N} \Delta\theta(\theta_j) \quad (7\text{-}6)$$

Equations (7-5) and (7-6) may be easily evaluated with a computer for various combinations of R, θ_* and ε_c. The calculations confirm conclusions that may be drawn from studying Figure VII.1. It is seen that the position of the star image relative to the trigger determines the effect of de-centering error on the coordinates (R,θ). For example, if $\theta_* = 0$, the error in R will average to zero but the error in θ will be maximum over the 180^0 sweep. For $\theta_* = 90^0$ the situation is reversed. For example, a star with $(R,\theta)_* = (3.0\text{mm},0^0)$ and $\varepsilon_c \approx 5$ microns will have $(\Delta R,\Delta\theta) = (0.0\mu,3.2\mu)$; at $(R,\theta_*) = (3.0,45^0)$, $(\Delta R,\Delta\theta) = (-2.2, 2.2)$. The smearing due to de-centering is present even if the displacement averages to zero. For the above case, the standard deviations of the set of $(\Delta R_j,\Delta\theta_j)$ are (3.5,3.5) microns.

This discussion shows that great care should be taken in centering the Ronchi ruling. The ruling used for observations in this paper was painstakingly centered by matching the shapes of the low frequency components in a full 360^0 of rotation. It is estimated that the error in centering is no more than 5 microns. It should be emphasized that this error produces systematic effects that are functions primarily of θ_* and ε_c and unaffected by R itself.

VIII. Alternative Grating Patterns

The technique of the AMAS is not limited to a simple Ronchi ruling. This pattern was adopted for the prototype primarily because of its availability. For instance, a ruling with a cosine transmission pattern would be mathematically more simple and would eliminate errors arising from ignoring higher order terms native to the Ronchi ruling. However, a cosine ruling is significantly more difficult to construct with sufficient precision. Any sort of grating pattern whose transmission function may be written down is a candidate for the AMAS. Desirable properties for such a grating reduce principally to transparency per unit area and simplicity to construct. Jacobs (1973) has investigated in detail the properties of an orthogonol Ronchi ruling, i.e. two Ronchi patterns superposed orthogonally. Such a pattern should provide equally high precision in both R and θ. The transmission function is separable in (x,y). This pattern also easily provides transparency ratios or "throughputs" on the order of 75% by constructing a negative "checkerboard" whose transmission function is $(1 - T(x,y))$ where $T(x,y)$ is the transmission function for the normal orthogonal Ronchi ruling.

Another type of modulation technique has been suggested by the Perkin and Elmer Corporation which utilizes a random dot coded disk. Rotation of this disk produces a speckle pattern which presumably may be analyzed for positional and intensity information. If such a disk is pictured with the

second 180^0 being identical to the first as is shown in Figure VIII.1.; the amplified signal from the first may be played back through the second to produce a "picture" of the first half's field of view. This seemingly nonsense situation may be extended to two identical disks which are connected via a telemetry link as is shown in Figure VIII.2. The two must, of course, be highly synchronized. The random coded mask could also be scanned and stored in a computer so that the down-link signal could be compared in a manner to give the desired astrometric information. The details of this technic have not been worked out and are under study at the McCormick Observatory.

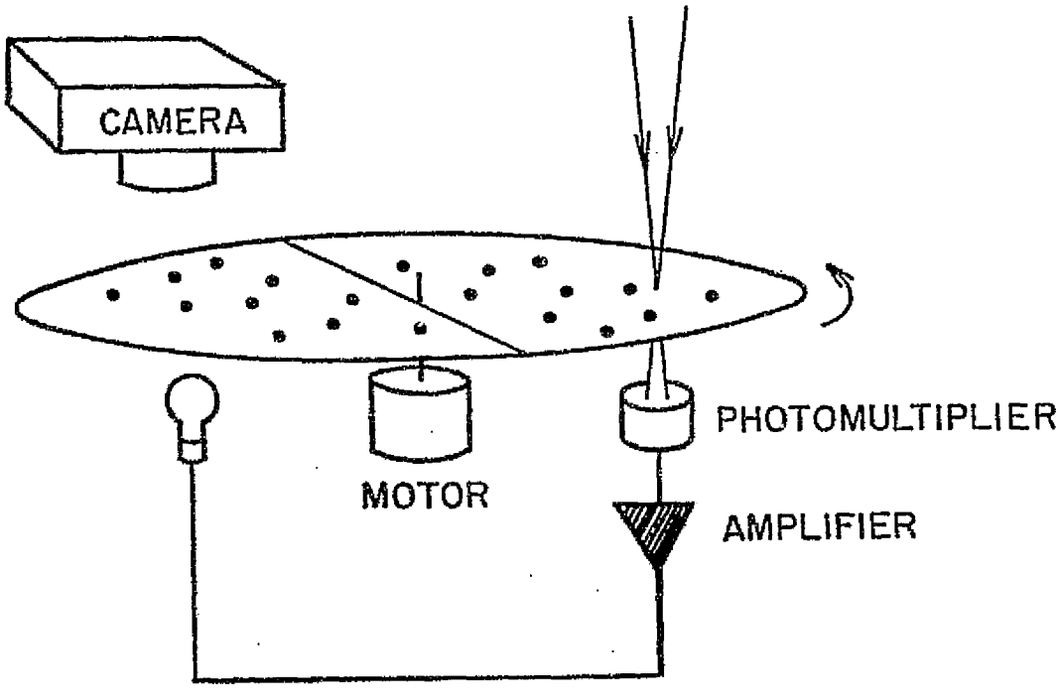

Figure VIII.1. Schematic Diagram of the Operation of the Random Coded Disk With Identical Halves.

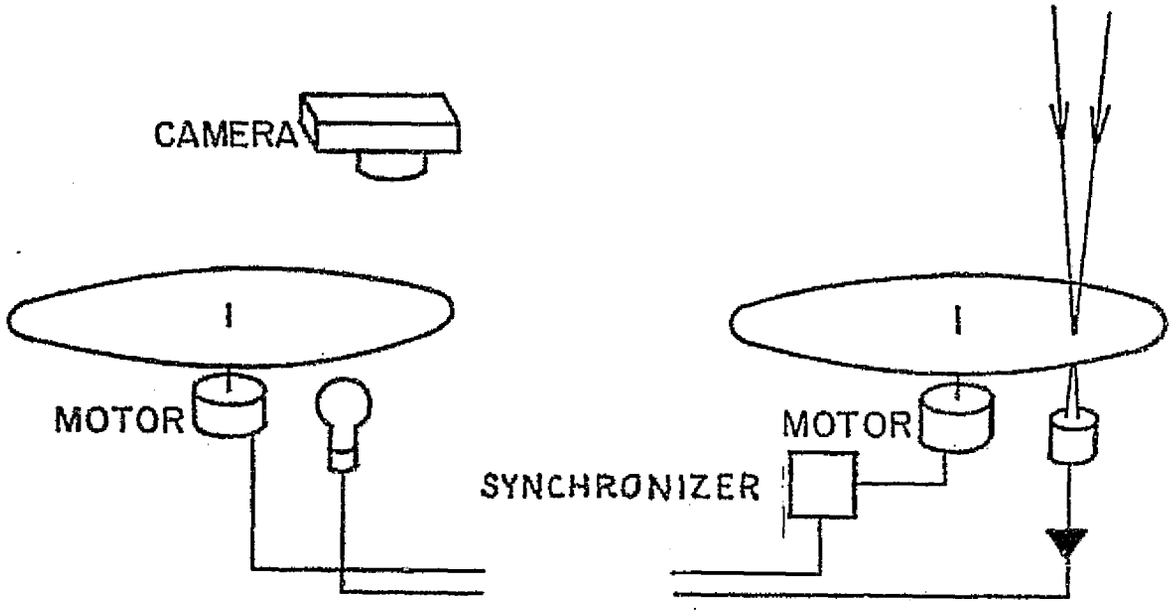

Figure VIII.2. Schematic Diagram of the Operation of Two Removed but Synchronized Random Coded Disks.

IX. The AMAS as an LST Instrument

A. General

The present series of laboratory experiments shows that the prototype AMAS with a Ronchi ruling performs as well as the traditional photographic plate-measuring machine combination. This result alone indicates the viability of an AMAS as a ground-based astrometric instrument. The AMAS also appears to be well suited to performing astrometry on the LST, if it can withstand launch conditions. The focal plane scale of the LST of $\sim 3''.0\ mm^{-1}$ offers a sensitivity surpassing present ground based astrometric telescopes. Even the prototype instrument would provide single relative measurements accurate to within $0''.004$, a factor of five better than current ground based instruments and only a factor of two above the desired accuracy of $0''.002$. Resolution appears to be limited by angular size and δm. For LST images with diameters $\sim 0''.1$, the prototype AMAS should resolve separations $\geq 0''.13$ for $\Delta m \sim 0$. With the utilization of available technology to refine the presently rather crude version of the AMAS, this technique offers a simple way of performing astrometric studies from the LST.

B. Critical Parameters for an LST Instrument

The following critical parameters for the construction of an LST version of the AMAS must be given consideration:

1. Uniform Rotation - The rate of rotation of the modulating ruling or grating must be constant to the tolerance as described in Section VI. For an LST version with a field of 5 arcminutes (100 mm at 3".0 mm^{-1}) the positional accuracy must be $\lesssim$15 microradians.
2. Accurate Centering - Calculations show that error in centering produces systematic position errors $\sim 0.6\ \epsilon_c$. Thus, an LST AMAS using a Ronchi ruling must be centered to a tolerance of 0.5 micron.
3. Adequate Data Registration Capacity - For LST image diameters $\sim$0".1 the conditions for suppression of higher order terms require that $\sim$3300 lines cross star images at the edge of the field forthest from the center of rotation. To record the highest frequency component with a minimum of three sample points requires a minimum position angle sampling increment of $L/3R \simeq 100$ microradians which corresponds to $\pi \times 10^4$ channels to record 180^0 of rotation.
4. Flatness of Field - Any field curvature which produces deviations from true positions greater than a few tenths of a micron must be eliminated by one or a combination of methods. Field flattening optics may be placed in the optical path, the modulating grating may be optically figured to match the field curvature or small deviations from flatness may be adequately taken care of by mathematical modeling in the data

reduction procedure.

5. Operating Modes for the AMAS - The AMAS could be operated in two basic modes:

   (i) Predetermined-semi dedicated mode where previously chosen fields will be observed using predetermined relative coordinates to drive the field limiting yoke on the image dissector.

   (ii) Serendipity mode using a dwell pattern on the yoke to scan the current field of view in carrying out a routine check for multiplicity, etc. The AMAS would ideally be functioning in either of these modes at all times.

C. Areas for Continued Study

As with all new techniques with a wide range of applicability, it is essential that continuing efforts be made to bring to light additional subtle effects inherent in the technique. As often expressed here, the simplicity and straight-forwardness of the AMAS lead to the conclusion that only small order effects may still be hidden after the rather extensive amount of research that has gone into the technique to date. However, efforts at this observatory are being made to construct a new AMAS using a precision encoded motor with a shaft mounted ruling to obtain further ground based observations to seek out such effects.

One deficit of the present AMAS is its limited intra-scene dynamic range, which restricts its application to stellar field work. For single stars, this problem may be

avoided by using the image dissector. For binary stars, an inherent limit to values of $\delta m < 5$ appears difficult to surmount, as the secondary signal amplitude is then on the order of the ignored third order term arising from the square wave transmission pattern. The related problem of the consequences of ignoring this term may be considered by looking at Equation (1-4). For $\sigma/L \simeq 0.5$ one sees that the ignored term is equivalent to a star with coordinates $(3R,\theta)$ and an intensity down by nearly 5.4 magnitudes. Experience with laboratory star images shows that although the errors in the reduced coordinates of the faint star are large, the errors in the star brighter by 5 magnitudes are entirely negligible. This simple argument indicates that the simplifying assumptions made by Rosenberg in the currently applied data reduction scheme are entirely adequate for an LST version of the AMAS.

An additional possible application for the AMAS is the astrometry of planetary satellites. If the Ronchi ruling is modified so that only small opposite portions of the planetary limb are visible when the planetary center is adjusted to coincide with the center of ruling rotation, then positions of, say, the fainter Jovian satellites can be measured with respect to the center of the Jovian disk. Precise centering can be accomplished by studying the effects of slight telescope adjustments on the form of the signal produced from the modulated limb. Such additional possibilities further illustrate the versatility of the AMAS.

References

Code, A.D. 1960, in Stars and Stellar Systems, G.P, Kuiper and B.D. Middlehurst, eds. (Chicago: University of Chicago Press), Vol.6, chap.2, p.50.

Fredrick, L.W., McAlister, H.A., van Altena, W.F. and Franz, O.G. 1975, Space Astrometry : ESRO SP-108 (Noordwijk, Netherlands: ESRO Scientific & Technical Branch), p.49.

Gursky, H. and Schwartz, D. 1974, in X-Ray Astronomy, R. Giacconi and H. Gursky, eds. (Boston: D. Reidel Pub. Co., Inc.), Chap 2, p.65.

Jacobs, K.C. 1973, unpublished report.

Rosenberg, F.D. 1972, unpublished Ph.D. dissertation, University of Virginia.

Rosenberg, F.D. 1973, private communication.

Smith, C.D. 1973, unpublished Ph.D. dissertation, University of Virginia.

Strikwerda, T.E. 1975, private communication.

van de Kamp, P. 1967, Principles of Astrometry (San Francisco: W.H. Freeman and Co.), p.146.

Appendix

CONTRACTUAL STATEMENT OF WORK

SUPPORTING RESEARCH TO ASCERTAIN THE TRUE PERFORMANCE LIMITS OF THE ASTROMETRIC MULTIPLEXING AREA SCANNER (AMAS)

General

The AMAS is a potential Large Space Telescope (LST) instrument for the gathering of astrometric data. However, present ground-based observations with the AMAS give results of a lower precision than anticipated. The purpose of this program is to demonstrate by a laboratory study of the AMAS that its current apparent limitations are not inherent to the technique, and thus, that it is worthy of consideration as a possible LST instrument. The basic format of the study is the laboratory observations by the AMAS of artificial double stars and stellar fields, attempting thereby to simulate simply LST conditions. The program duration is to be one year. The reporting on the work will be through brief quarterly reports, and the delivery of a comprehensive final report one month after the completion of all tasks.

Task 1

Construct a series of artificial double stars to be used in the laboratory testing of the AMAS. These artificial double stars should approximate the real images expected from a diffraction limited LST of focal ratio about 24. Their separations and magnitude differences should adequately mock-up those physical conditions representative of priority observations for an AMAS on the LST. In particular, their minimal separations are to be ten to one-hundred times less than those real doubles presently resolvable (4 arc-sec) using the AMAS on a ground-based telescope. In addition, some artificial star fields should be generated to demonstrate the p wer of the AMAS for doing parallax and proper motion studies.

Task 2

Develop a best method of data analysis by improving the present computer programs, and/or by modifying the underlying mathematical techniques used in the deconvolution of the AMAS's photomultiplier response function (PRF).

Task 4

Determine the effects of non-uniform grating rotation on the precision of the results; and from these findings specify the uniformity of grating rotation needed for LST work.

Task 5

Ascertain what particular Ronchi pattern on the grating optimizes the precision of the results. Investigate other alternative grating patterns, and determine if they can give improved precision over that derived using Ronchi-pattern type gratings.

Task 6

Specify the degree of field flatness required at the focal plane to ensure good results over an astrometrically useful field of view.

Task 7

Estimate qualitatively the potential long-term stability of the AMAS's performance under LST conditions. (e.g., expected degradation of the results from bearing aging, effects caused by uneven photocathode response due to charged particle damage, etc.)

Task 8

Prepare for the final report a section which presents, based on the hard results generated by this study, an opinion on the viability of AMAS use on the LST. This section must include discussions of: (1) problem areas remaining that require further study; and, (2) those critical parameters of the AMAS that must be recognized in constructing an LST instrument.

The NASA Technical Officer for this Report is Thomas Kelsall, Goddard Spaceflight Center, Greenbelt Road, Greenbelt, Maryland, 20771.